CAMBRIDGE
UNIVERSITY PRESS

Research Article

Evolutionary Map of the Universe (EMU): A pilot search for diffuse, non-thermal radio emission in galaxy clusters with the Australian SKA Pathfinder

S.W. Duchesne[1], A. Botteon[2], B.S. Koribalski[3,4], F. Loi[5], K. Rajpurohit[6], C.J. Riseley[7,8,1], L. Rudnick[9], T. Vernstrom[10,1], H. Andernach[11,12], A.M. Hopkins[13], A.D. Kapinska[14], R.P. Norris[4,3], and T. Zafar[13]

[1]CSIRO Space and Astronomy, Bentley, WA, Australia, [2]INAF-IRA, Bologna, Italy, [3]CSIRO Space and Astronomy, Epping, NSW, Australia, [4]Western Sydney University, Penrith, NSW, Australia, [5]INAF–Osservatorio Astronomico di Cagliari, Selargius, Italy, [6]Harvard-Smithsonian Center for Astrophysics, Cambridge, MA, USA, [7]Dipartimento di Fisica e Astronomia, Università degli Studi di Bologna, Bologna, Italy, [8]INAF–Istituto di Radioastronomia, Bologna, Italy, [9]Minnesota Institute for Astrophysics, University of Minnesota, Minneapolis, MN, USA, [10]ICRAR, The University of Western Australia, Crawley, Australia, [11]Thüringer Landessternwarte, Tautenburg, Germany, [12]Depto. de Astronomía, Univ. de Guanajuato, Callejón de Jalisco s/n, Guanajuato, GTO, Mexico, [13]School of Mathematical and Physical Sciences, Macquarie University, Sydney, NSW, Australia and [14]National Radio Astronomy Observatory, Socorro, NM, USA

Abstract

Clusters of galaxies have been found to host Mpc-scale diffuse, non-thermal radio emission in the form of central radio halos and peripheral relics. Turbulence and shock-related processes in the intra-cluster medium are generally considered responsible for the emission, though details of these processes are still not clear. The low surface brightness makes detection of the emission a challenge, but with recent surveys with high-sensitivity radio telescopes we are beginning to build large samples of these sources. The Evolutionary Map of the Universe (EMU) is a Southern Sky survey being performed by the Australian SKA Pathfinder (ASKAP) over the next few years and is well-suited to detect and characterise such emission. To assess prospects of the full survey, we have performed a pilot search of diffuse sources in 71 clusters from the *Planck* Sunyaev–Zeldovich (SZ) cluster catalogue (PSZ2) found in archival ASKAP observations. After re-imaging the archival data and performing both (u, v)-plane and image-plane angular scale filtering, we detect 21 radio halos (12 for the first time, excluding an additional six candidates), 11 relics (in seven clusters, and six for the first time, excluding a further five candidate relics), along with 12 other, unclassified diffuse radio sources. From these detections, we predict the full EMU survey will uncover up to ≈ 254 radio halos and ≈ 85 radio relics in the 858 PSZ2 clusters that will be covered by EMU. The percentage of clusters found to host diffuse emission in this work is similar to the number reported in recent cluster surveys with the LOw Frequency ARray (LOFAR) Two-metre Sky Survey [Botteon, et al. 2022a, A&A, 660, A78], suggesting EMU will complement similar searches being performed in the Northern Sky and provide us with statistically significant samples of halos and relics at the completion of the full survey. This work presents the first step towards large samples of the diffuse radio sources in Southern Sky clusters with ASKAP and eventually the SKA.

Keywords: galaxies: clusters: general; large-scale structure of the Universe; radio continuum: general

1. Introduction

1.1 Radio emission in galaxy clusters

Diffuse, non-thermal radio emission has been observed in hundreds of galaxy clusters and is thought to be linked to the dynamics of the hot ($\approx 10^7$–10^8 K), X-ray-emitting intra-cluster medium (ICM). These synchrotron radio sources are generated by the μ G-level (e.g. Clarke et al., 2001; Brüggen et al., 2012) cluster magnetic fields, fuelled by energy deposited via cluster mergers and accretion – see Brunetti & Jones (2014) for an overview

of the theoretical frameworks describing the physical mechanisms responsible for the diffuse radio emission and van Weeren et al. (2019) and Paul et al. (2023) for observational reviews. While there are a number of different generation mechanisms for diffuse radio sources, they share some common properties: the spectral properties of the sources tend to preclude singular energy/particle injection sites, requiring in situ (re-)acceleration mechanisms (e.g. Jaffe, 1977). The observed spectra are steep, with spectral indices[a] $\alpha \lesssim -1$ Duchesne et al., 2021d). Due to their steep radio spectra, diffuse cluster sources are best detected at low frequencies.

Radio halos are found at the centres of some clusters. The size of these sources is typically of order ≈ 1 Mpc and they are found predominantly in merging and post-merger cluster systems (e.g. Cassano et al., 2010, 2023). The mechanisms powering radio halos

[a]We define the spectral index, α, via $S_\nu \propto \nu^\alpha$, for a flux density S_ν at frequency ν.

are not completely understood, though it is likely related to turbulence in the ICM as a result of major mergers (e.g. Brunetti et al., 2001; Petrosian, 2001; Cassano et al., 2007). At the smaller scale ($\lesssim 500$ kpc) 'mini-halos' are found in relaxed cool-core clusters (e.g. Giacintucci et al., 2017, 2019). Sloshing in the core of the cluster likely powers the emission, with the observed radio properties otherwise being similar to normal radio halos. Halos with multiple components have also been observed (e.g. in RX J1720.1+2638; Biava et al., 2021). Indeed, the once-clear division between mini-halo and halo is becoming blurred with the new generation of radio interferometers, with transitional 'mini'-halos showing mixed characteristics typical of both mini-halos and halos (e.g. Riseley et al., 2022a, 2023). Diffuse emission is also being found at much larger scales than the traditional radio halo (e.g. Shweta et al., 2020; Rajpurohit et al., 2021; Vacca et al., 2022b,a; Botteon et al., 2022b; Bruno et al., 2023b) with so-called 'megahalos' also featuring a change in their radio surface brightness profile hinting at a change in physical conditions with increasing distance from the cluster centre (Cuciti et al., 2022).

In the low-density cluster outskirts, elongated radio sources other than tailed radio galaxies are occasionally observed. These are typically referred to as *radio relics*[b], and have been observed to be co-located with shocks detected via X-ray emission (e.g. Finoguenov et al., 2010; Akamatsu et al., 2015; Urdampilleta et al., 2018; Di Gennaro et al., 2019). Because of the coincidence with shocks and observed morphology and spectra the physical mechanism generating relics is thought to relate to shock-acceleration processes (e.g. Enßlin et al., 1998; Hoeft & Brüggen, 2007; Kang, 2018). When observed with high sensitivity radio telescopes, some relics have been detected with a diffuse component that physically extends and spectrally steepens towards the cluster centre (e.g. in 1RXS J0603.3+4214; van Weeren et al., 2012; Rajpurohit et al., 2018, 2020). In some cases, multiple relics are observed in a single cluster (e.g. in Abell 3667; Röttgering et al. 1997; Johnston-Hollitt 2003; Hindson et al. 2014; Riseley et al. 2015; de Gasperin et al. 2022, and Abell 3376; Bagchi et al. 2006; Kale et al. 2012) and complex merging systems have been observed to host both radio relics and halos (e.g. in Abell 2744; Pearce et al. 2017; Rajpurohit et al. 2021, and Abell 3266; Duchesne et al. 2022; Riseley et al. 2022b). The exact shock (re-)acceleration mechanism is still being investigated, and larger numbers of sources and highly-detailed multiwavelength analyses are required to understand these sources further.

Finally, other, smaller-scale diffuse emission is seen in some clusters (e.g. Slee et al., 2001; Hodgson et al., 2021). These sources include steep-spectrum fossil plasmas left over from past episodes of active galactic nuclei (AGN). These sources may be simply ageing through synchrotron and inverse-Compton losses, or in some cases may be re-energised by mechanical processes in the ICM (e.g. adiabatic compression due to shocks; Enßlin & Gopal-Krishna, 2001). Revived fossil plasmas have been observed connected to active radio galaxies (e.g. van Weeren et al., 2017; de Gasperin et al., 2017). Such sources provide possible links to the aforementioned radio relics and highlight a fossil electron population that may provide mildly-relativistic particles for shock–re-acceleration processes (e.g. Vazza et al., 2021).

1.2 Surveys with modern radio telescopes

With the new, sensitive radio interferometers at low frequencies ($\lesssim 1$ GHz), there have been a number of radio surveys of clusters as well as detections of heretofore unseen types of emission. Below 231 MHz, work with the Murchison Widefield Array (MWA; Tingay et al., 2013; Wayth et al., 2018) has had its large fractional bandwidth leveraged to explore spectral properties of these steep-spectrum radio sources (Hindson et al., 2014; George et al., 2017; Giacintucci et al., 2020; Duchesne et al., 2020; Hodgson et al., 2021; Duchesne et al., 2021d,b, 2022). In the Northern Hemisphere, the LOw Frequency ARray (LOFAR; van Haarlem et al., 2013) and the recent second data release from the LOFAR Two-metre Sky Survey (LoTSS-DR2; Shimwell et al., 2022) is also being used for surveys of new diffuse cluster sources (e.g. van Weeren et al., 2021; Hoang et al., 2022) with the latest data release providing the largest single sample of clusters hosting diffuse radio sources (Botteon et al., 2022a, hereinafter BSC22) along with in-depth statistical analyses of the sources and the hosting clusters (Bruno et al., 2023a; Zhang et al., 2023; Cassano et al., 2023; Cuciti et al., 2023; Jones et al., 2023).

Closer to ≈ 1 GHz MeerKAT is also producing images of unprecedented sensitivity and resolution of clusters as part of surveys (e.g. Knowles et al., 2021) including the MeerKAT Galaxy Cluster Legacy Survey (MGCLS; Knowles et al., 2022) which is enabling highly-informative studies of selected cluster systems and the constituent diffuse, non-thermal radio emission (e.g. Riseley et al., 2022a; Giacintucci et al., 2022; Sikhosana et al., 2023; Trehaeven et al., 2023; Riseley et al., 2023). The upgraded Giant Metrewave Radio Telescope (uGMRT; Gupta et al., 2017) is also producing in-depth multi-wavelength studies of galaxy clusters, enabling new detections (e.g. Schellenberger et al., 2022; Pandge et al., 2022; Lee et al., 2022; Kurahara et al., 2023) providing muchneeded bandwidth to investigate the wideband spectral properties of these sources (e.g. Rajpurohit et al., 2020, 2021; Di Gennaro et al., 2021; Kale et al., 2022).

1.3 The Australian SKA Pathfinder

The Australian SKA Pathfinder (ASKAP; Hotan et al. 2021) is a 36-antenna radio interferometer located on Inyarrimanha Ilgari Bundara, the CSIRO[c] Murchison Radio-astronomy Observatory. ASKAP operates between 700–1800 MHz with an instantaneous bandwidth of 288 MHz and features 12-m dishes. The array has baselines ranging from 22 m to 6 km, providing sensitivity to angular scales up to ≈ 50 arcmin and an angular resolution of $\approx 12''$ at 900 MHz. ASKAP's primary purpose is all-sky radio surveys, including continuum (e.g. Norris et al., 2011, 2021), linear polarisation (Gaensler et al., 2010; Thomson et al., 2023), spectral line work (e.g. Rhee et al., 2023; Dickey et al., 2013; Koribalski et al., 2020; Allison et al., 2022), and transient/variability surveys (Macquart et al., 2010; James et al., 2019; Murphy et al., 2021). The main technology that allows ASKAP surveying capability is its phased array feeds (PAF; Hotan et al., 2014; McConnell et al., 2016). The PAF simultaneously forms 36 mostly-independent primary beams that are arranged in a regular footprint on the sky covering ≈ 30 deg^2 at 900 MHz.

---

[b]Note that these sources are also sometimes referred to as 'radio shocks'.

[c]Commonwealth Scientific and Industrial Research Organisation.

While ASKAP has completed the first two epochs of the shallow Rapid ASKAP Continuum Survey (RACS; McConnell et al., 2020; Duchesne et al., 2023a), one of the major continuum surveys undertaken by ASKAP is the Evolutionary Map of the Universe (EMU; Norris et al., 2011, 2021). EMU is to cover the Southern Sky at 943 MHz with a total integration time of 10 h per pointing. With a standard image point-spread function (PSF) of $15'' \times 15''$ the expected noise characteristics approach $\approx 30\,\mu\mathrm{Jy\,PSF^{-1}}$. The survey is to be completed over the next few years, with $\approx 15\%$ of the survey currently observed. The main science goals of EMU are to trace the evolution of star-forming galaxies and supermassive black holes, to explore large-scale structure and cosmological parameters, to use radio sources to help understand clusters, to study Galactic continuum emission, and to explore an uncharted region of observational parameter space, and find new classes of objects.

Shallow RACS data products have already been used to help characterise diffuse radio emission in galaxy clusters (Duchesne et al., 2021d, 2022), but the deep ASKAP observations of EMU and other deep ASKAP surveys are providing many new detections – and a more in-depth characterisation – of such sources (e.g. Wilber et al., 2020; HyeongHan et al., 2020; Brüggen et al., 2021; Duchesne et al., 2021a,b; Venturi et al., 2022; Riseley et al., 2022b; Loi et al., 2023; Macgregor et al., submitted). Completion of the EMU survey is expected to yield an additional large sample of radio halos and relics, complementing similar surveys being conducted with LOFAR. In this work we aim to explore the prospects of the full EMU survey in the context of uncovering radio halos and relics using similar, archival ASKAP observations.

Where relevant, we assume a flat Λ cold dark matter cosmology with $H_0 = 70\,\mathrm{km\,s^{-1}\,Mpc^{-1}}$, $\Omega_M = 0.3$, and $\Omega_\Lambda = 1 - \Omega_M$.

2. The galaxy cluster sample

Following BSC22, we select clusters reported in the second *Planck* Sunyaev–Zeldovich (SZ) cluster catalogue (PSZ2; Planck Collaboration et al., 2016a), which provides a selection of clusters across a range of redshifts with masses of $\approx 10^{14}$–$10^{15}\,\mathrm{M_\odot}$. Figure 1 shows the mass distribution of the full 1 653 clusters in the PSZ2 catalogue as well as the subsample used in this work, as described below.

To select PSZ2 clusters to search, we obtain all archival ASKAP datasets with Stokes I total intensity images available, that fit the following criteria:

1. Observed in ASKAP Band 1 ($\lesssim 1$ GHz central frequency),
2. Observed after all 36 antennas became operational (though ignoring flagged antennas),
3. Observed for ≥ 5 h,
4. Field direction not within Galactic latitudes $b \pm 5°$,
5. Publicly 'released' before October 1, 2022,
6. Not a duplicated field – if fields were observed multiple times, only the 'best' quality (i.e. lowest median rms noise) was selected.

Other, particularly higher-frequency (Band 2), observations are available in the archive that could also be used, though we adhere
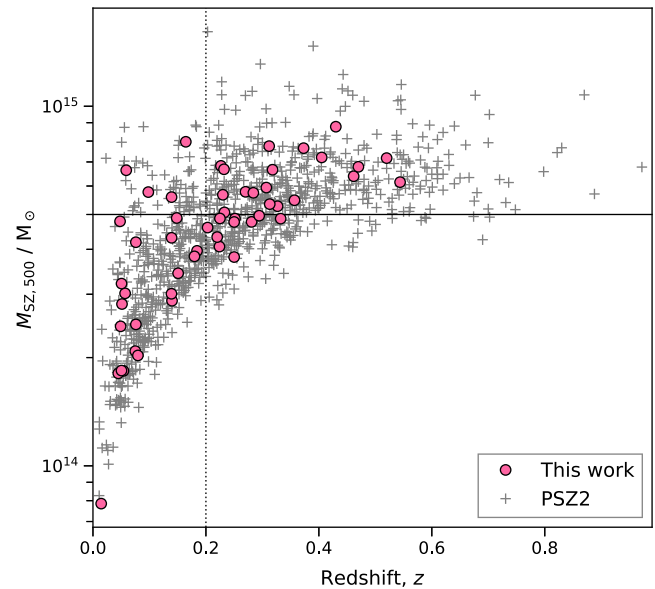

Figure 1. The distribution of cluster mass with redshift for the PSZ2 catalogue (gray crosses) and the sample used in this work (pink circles) for clusters with reported redshifts. A vertical dotted line is drawn at $z = 0.2$, the redshift we assume for clusters with no reported redshift. The horizontal line is drawn at $M_{SZ,500} = 5 \times 10^{14}\,\mathrm{M_\odot}$.

to these criteria to ensure a similar dataset to the main EMU survey. During the commissioning and early science phase of ASKAP (prior to November 16, 2022, when full operations commenced), ASKAP had been performing numerous operational tests, including pilot surveys for the main ASKAP Survey Science Teams (SST). These SSTs cover a range of scientific goals, from neutral hydrogen absorption and emission studies of distant (Rhee et al., 2023; Allison et al., 2022) and nearby (Dickey et al., 2013; Koribalski et al., 2020) targets, to transient and variability studies of both Galactic and extra-Galactic objects (e.g. Murphy et al., 2021), and studies of linear polarisation of radio sources with POSSUM[d] (Gaensler et al., 2010). Included in these SSTs are also the total intensity continuum surveys such as EMU, covering most of the Southern Sky, and the Survey with ASKAP of GAMA-09 + X-ray (SWAG-X; Moss et al., in prep.), overlapping with the GAMA-09[e] field.

The chosen observation scheduling block IDs (SBIDs) and their details are recorded in Table 1. A total of 36 SBIDs are available fitting the above criteria, however, two do not feature PSZ2 clusters. The total area covered is $\approx 1\,990\,\mathrm{deg^2}$, which comprises 71 PSZ2 clusters (≈ 0.036 PSZ2 clusters per $\mathrm{deg^2}$). Figure 2 shows the distribution of clusters and selected observations across the sky, and Table 2 summarises the 71 clusters. The selected SBIDs include observations from the EMU Pilot Survey (Norris et al., 2021), Gravitational wave follow-up observations, SWAG-X, *TESS* follow-up observations (Rigney et al., 2022), a POSSUM observation that is commensal with EMU, and various other EMU early science and commissioning observations (e.g. Brüggen et al., 2021; Gürkan et al., 2022; Quici et al., 2021). A handful of these

---

[d]The Polarisation Sky Survey of the Universe's Magnetism.
[e]Galaxy And Mass Assembly at declination $-9°$.

Table 1. Archival ASKAP observations used in this work.

SBID	ν[a]	Coordinates[b]	Project	Purpose	Footprint	Pitch	τ_{int}[c]	σ_{rms}[d]	PSF[e]
	(MHz)	(J2000)				(deg)	(h)	(μJy PSF^{-1})	(arcsec × arcsec)
8132	888	22:46:14 −32:15:35	AS034	Early Science	`square_6x6`	0.90	9.0	46.2	10.0 × 8.5
8137	888	23:11:46 −32:15:35	AS034	Early Science	`square_6x6`	0.90	10.0	44.4	10.1 × 8.5
8275	1014	06:26:49 −54:04:19	AS034	Early Science	`square_6x6`	0.90	10.0	28.2	11.2 × 9.5
9287	944	21:00:00 −51:07:06	AS101	EMU	`closepack36`	0.90	10.0	34.3	14.8 × 11.1
9325	944	20:34:17 −60:19:18	AS101	EMU	`closepack36`	0.90	10.0	35.3	12.5 × 10.9
9351	944	20:42:00 −55:43:29	AS101	EMU	`closepack36`	0.90	10.0	38.5	12.0 × 10.7
9410	944	21:15:26 −60:19:18	AS101	EMU	`closepack36`	0.90	10.0	32.6	11.8 × 10.7
9434	944	21:32:44 −51:07:06	AS101	EMU	`closepack36`	0.90	10.0	30.1	12.1 × 10.1
9437	944	20:27:16 −51:07:06	AS101	EMU	`closepack36`	0.90	10.0	35.3	12.0 × 10.1
9442	944	21:18:00 −55:43:29	AS101	EMU	`closepack36`	0.90	10.0	33.3	14.0 × 10.9
9501	944	21:56:34 −60:19:18	AS101	EMU	`closepack36`	0.90	10.0	31.9	12.1 × 10.7
9596	944	05:56:19 −33:09:10	AS111	GW follow-up	`closepack36`	0.90	10.0	36.4	12.1 × 9.7
10083	944	21:54:00 −55:43:29	AS101	EMU	`closepack36`	0.90	10.0	32.2	12.1 × 9.9
10135	888	09:29:10 −01:39:32	AS112	SWAG-X	`square_6x6`	1.05	8.6	45.1	13.3 × 12.1
10475	888	08:38:45 +04:38:27	AS112	SWAG-X	`square_6x6`	1.05	8.7	53.7	13.4 × 12.4
10486	888	09:04:00 −01:39:00	AS112	SWAG-X	`square_6x6`	1.05	8.6	57.7	13.2 × 11.6
13570	944	00:58:00 −23:45:00	AS033	Commissioning	`closepack36`	0.90	10.0	37.0	12.6 × 9.7
15191	944	00:50:38 −25:16:57	AS111	GW follow-up	`closepack36`	0.90	10.5	30.1	12.4 × 9.9
20875	888	09:29:15 +04:38:27	AS112	SWAG-X	`closepack36`	1.05	8.0	46.4	13.4 × 12.5
20931	888	09:04:00 +04:39:00	AS112	SWAG-X	`closepack36`	1.05	8.0	48.1	13.5 × 12.5
21021	888	08:38:50 −01:39:32	AS112	SWAG-X	`closepack36`	1.05	8.0	57.1	13.3 × 11.9
25035	888	04:24:00 −70:00:00	AS113	*TESS* followup	`square_6x6`	1.05	13.0	34.9	13.9 × 12.0
25077	888	05:08:00 −60:00:00	AS113	*TESS* followup	`square_6x6`	1.05	13.0	33.7	13.9 × 11.4
28257	944	02:30:27 +00:00:00	AS101	EMU	`closepack36`	0.90	5.1	74.0	18.0 × 18.0
32235	944	19:08:00 −64:30:00	AS113	*TESS* followup	`closepack36`	0.90	10.0	37.2	12.3 × 11.2
33370	944	02:08:57 −09:20:42	AS101	EMU	`closepack36`	0.90	5.0	56.6	18.0 × 18.0
33459	944	02:08:57 −04:40:35	AS101	EMU	`closepack36`	0.90	5.0	52.7	18.0 × 18.0
33509	944	02:30:27 −04:40:35	AS101	EMU	`closepack36`	0.90	5.0	57.6	18.0 × 18.0
34120	944	13:29:47 −30:17:10	AS103	POSSUM	`closepack36`	0.90	10.0	32.6	12.3 × 9.9
41688	944	09:00:00 −57:00:00	AS113	Pointing test	`closepack36`	0.90	10.0	29.6	12.3 × 10.7
41710	944	09:00:00 −29:00:00	AS113	Pointing test	`closepack36`	0.90	10.0	30.7	12.3 × 10.1
41757	944	09:00:00 −37:00:00	AS113	Pointing test	`closepack36`	0.90	10.0	28.5	12.5 × 10.3
41850	944	09:00:00 −24:00:00	AS113	Pointing test	`closepack36`	0.90	10.0	31.4	12.4 × 10.2
41871	944	09:00:00 +03:00:00	AS113	Pointing test	`closepack36`	0.90	9.0	37.2	12.6 × 11.8
41894	944	09:00:00 −17:00:00	AS113	Pointing test	`closepack36`	0.90	10.0	31.4	12.4 × 10.5

[a]Effective image frequency.
[b]Coordinates at the centre of the tile.
[c]Total integration time for the given observation.
[d]Median rms noise over the archival, full-resolution image.
[e]PSF as reported in the image metadata, though note for older images on CASDA the PSF may vary slightly over the image.

SBIDs have already featured in work focused on diffuse emission in galaxy clusters (Wilber et al., 2020; HyeongHan et al., 2020; Brüggen et al., 2021; Duchesne et al., 2021b,d; Venturi et al., 2022; Riseley et al., 2022b; Loi et al., 2023) and for completeness in this work we report both previously detected sources and newly detected sources in the 71 PSZ2 clusters.

Of the 71 clusters selected for this work, 18 do not have redshifts reported in the original PSZ2 catalogue. We find six of these have spectroscopic redshifts reported in the literature, and for

these clusters we follow BSC22 and compute $M_{SZ,500}$ by interpolating the $M_{SZ}-z$ curves provided in the PSZ2 individual algorithm catalogues (Planck Collaboration et al., 2016b). One cluster, PSZ2 G167.43−53.67, has an angular separation < 10 arcmin from 15 other catalogued clusters (and one group) with redshifts in the range $0.132 \lesssim z \lesssim 1.35$. Due to the ambiguity in an possible cross-match, we do not obtain a redshift for this cluster. Cluster redshifts are reported in Table 2 along with the relevant redshift reference where available.
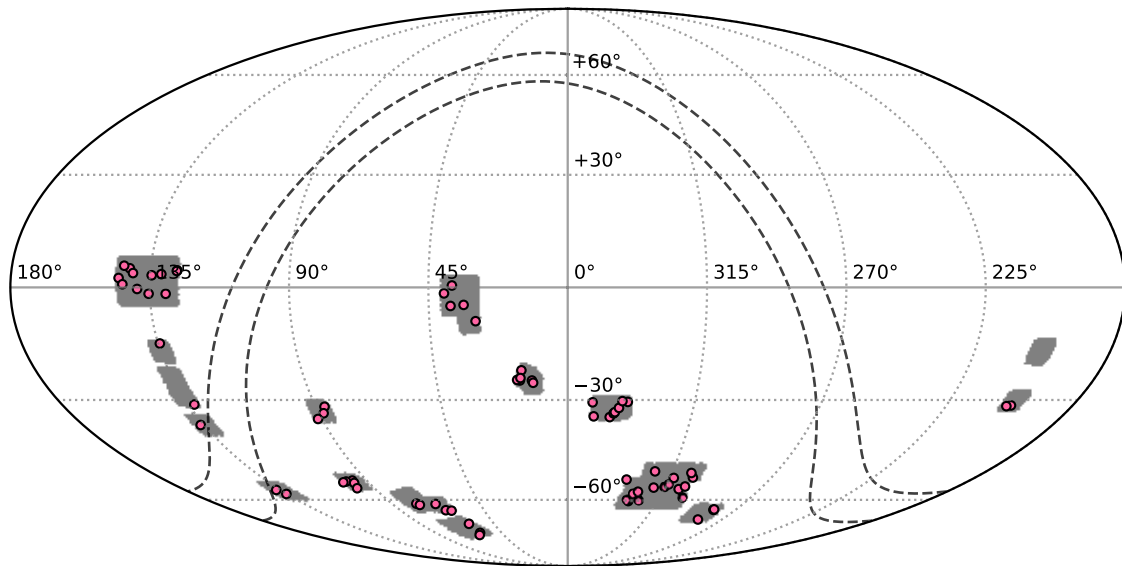
Figure 2. Equatorial map centered on $(\alpha_{J2000}, \delta_{J2000}) = (0, 0)^{\circ}$ showing the sky coverage of the ASKAP observations used in this work (shaded gray regions). The pink circles indicate the locations of the PSZ2 clusters used in this work. The black, dashed lines are drawn at Galactic latitudes $b \pm 5^{\circ}$.

3. Data

3.1 Archival ASKAP observations

3.1.1 Re-imaging the ASKAP data

As the archival ASKAP data have been processed at various stages of pipeline development and with a range of imaging settings (particularly image weighting), we opt to re-image all datasets containing the PSZ2 clusters from our sample. To avoid re-imaging PAF beams without significant sensitivity to clusters in our sample, we identify PAF beams that lie within 0.75 deg of a cluster from our sample. This results in 144 beams covering the 71 clusters, ranging from 1 to 4 beams per cluster. Each beam has its own visibility dataset and is re-imaged independently prior to co-addition/linear mosaicking for each target. Each beam dataset is retrieved from the CSIRO ASKAP Science Data Archive (CASDA Chapman et al., 2017; Huynh et al., 2020) and has already been self-calibrated as part of the usual ASKAPsoft data processing strategy. This direction-independent self-calibration procedure has remained reasonably unchanged over the course of processing the archival datasets and comprises two rounds of phase-only self-calibration. Our re-imaging process is in principle similar to the process described by van Weeren et al. (2021, see also Botteon et al. 2022a) used for LOFAR, though due to the higher frequency the direction-dependent effects caused by the ionosphere are not as problematic for the ASKAP data.

We stage each PAF beam dataset on the internal CSIRO supercomputer and use a bespoke processing pipeline SASKAP[f] for processing single ASKAP beams. We begin by creating large template images for each beam out to the first sidelobe with a Briggs (1995) robust +0.25 image weighting. We use WSClean[g] (Offringa et al., 2014; Offringa & Smirnov, 2017) for imaging, and make use of the multi-scale CLEAN algorithm for deconvolution and

the wgridder algorithm (Arras et al., 2021; Ye et al., 2021) for gridding/de-gridding. This template image provides a good model of the sky for primary beam modelling later on, and allows us to subtract the sky > 5 Mpc from the cluster centre. For clusters without a redshift, we follow BSC22 and assume $z = 0.2$ (here and for other redshift-dependent processing parameters described further on). For clusters with $z < 0.1$, we opt to reduce this size (cluster-dependent) to aid in processing. After subtracting the sky away from the cluster, we phase shift the individual beam datasets towards the direction of the target cluster and begin further self-calibration. This self-calibration process uses the CASA[h] (CASA Team et al., 2022) task gaincal with the CLEAN component model generated by WSClean, and performs two loops in most cases: (1) phase-only on 300 s intervals, and (2) amplitude and phase on 60 s intervals. Generally the amplitude self-calibration makes a significant improvement near bright sources, but in two cases failed. In the two failed cases, we simply turn this second stage off and rely on the phase-only self-calibration which yielded sufficient improvement for our purposes.

Figure 3 shows a comparison of the archival data with the phase-shifted and self-calibrated data for PSZ2 G241.79−24.01 in beam 5 of SB9596. The left panel shows the archival image, and the right panel shows a robust 0.0 image after self-calibration. PSZ2 G241.79−24.01 is the most extreme example of the self-calibration improvements, as it features a $S_{887\,MHz} \approx 1$ Jy source at its centre. The self-calibration reduces artefacts significantly enough to reveal heretofore unseen diffuse emission near the centre. These improvements are commensurate with the improvements seen using direction-dependent calibration and imaging software such as killMS (Tasse, 2014; Smirnov & Tasse, 2015) and DDFacet (Tasse et al., 2018, see Wilber et al. 2020; Brüggen et al. 2021; Riseley et al. 2022b for ASKAP examples) and are functionally similar to a single facet in cases without bright, off-axis sources.

[f]https://gitlab.com/Sunmish/saskap/-/tree/petrichor.
[g]https://gitlab.com/aroffringa/wsclean/.

[h]https://casa.nrao.edu/.

Table 2. PSZ2 clusters covered by the archival ASKAP data shown in this work.

Cluster	Other name	Coordinates[a] (hh:mm:ss, dd:mm:ss)	z	z ref.[b]	$M_{SZ,500}$ ($\times 10^{14}$ M$_\odot$)	Source(s)[c]	Source(s) ref.[d]
PSZ2 G006.16−69.49	–	23:22:09 −34:34:31	0.23	3	$3.73^{+0.50}_{-0.52}$	–	–
PSZ2 G008.31−64.74	Abell S1077	22:58:43 −34:47:18	0.312	1	$7.75^{+0.41}_{-0.40}$	R+R+cH	1
PSZ2 G011.06−63.84	Abell 3934	22:53:33 −33:44:20	0.224	1	$4.07^{+0.47}_{-0.49}$	cH	1
PSZ2 G011.92−63.53	Abell 3926	22:51:54 −33:23:39	0.24	4	$4.36^{+0.46}_{-0.48}$	H	1
PSZ2 G014.72−62.49	–	22:46:32 −32:12:04	0.5	3	$5.96^{+0.65}_{-0.71}$	–	–
PSZ2 G017.25−70.71	–	23:24:41 −30:39:04	0.31	3	$4.78^{+0.57}_{-0.64}$	–	–
PSZ2 G018.18−60.00	Abell 3889	22:34:51 −30:32:31	0.2515	1	$4.87^{+0.45}_{-0.47}$	–	–
PSZ2 G018.76−61.65	–	22:42:33 −30:18:54	0.24	3	$4.33^{+0.52}_{-0.60}$	–	–
PSZ2 G110.28−87.48	–	00:49:01 −24:40:13	0.52	1	$7.17^{+0.59}_{-0.65}$	H	1
PSZ2 G149.63−84.19	Abell 133	01:02:41 −21:54:44	0.0569	1	$3.02^{+0.18}_{-0.16}$	U+U	2
PSZ2 G167.43−53.67	–	02:29:35 +00:29:42	–	–	–	–	–
PSZ2 G167.66−65.59	–	01:59:55 −08:51:32	0.405	1	$7.20^{+0.61}_{-0.68}$	–	–
PSZ2 G167.98−59.95	Abell 329	02:14:44 −04:35:08	0.1393	1	$4.31^{+0.38}_{-0.39}$	–	–
PSZ2 G172.98−53.55	Abell 370	02:39:52 −01:34:05	0.373	1	$7.65^{+0.56}_{-0.57}$	H	3
PSZ2 G174.40−57.33	Abell 362	02:31:43 −04:51:40	0.1843	1	$3.96^{+0.49}_{-0.49}$	–	–
PSZ2 G175.69−85.98	Abell 141	01:05:30 −24:39:17	0.23	1	$5.67^{+0.36}_{-0.40}$	H	4
PSZ2 G180.74−85.21	–	01:09:14 −24:30:39	–	–	–	–	–
PSZ2 G219.88+22.83	Abell 664	08:25:08 +04:27:23	0.232813	1	$5.07^{+0.44}_{-0.48}$	cR	1
PSZ2 G220.11+22.91	–	08:25:47 +04:18:13	0.2248	1	$4.87^{+0.41}_{-0.45}$	–	–
PSZ2 G223.47+26.85	–	08:45:29 +03:28:31	0.3269	1	$5.27^{+0.65}_{-0.64}$	H	1
PSZ2 G225.48+29.41	Abell 732	08:57:54 +03:10:28	0.203	1	$4.60^{+0.45}_{-0.49}$	H	1
PSZ2 G227.59+22.98	–	08:39:26 −01:40:44	0.28085	1	$4.77^{+0.66}_{-0.67}$	cR+cR	1
PSZ2 G227.89+36.58	–	09:26:52 +05:00:35	0.4616	1	$6.39^{+0.67}_{-0.68}$	cH	1
PSZ2 G228.38+38.58	–	09:34:34 +05:41:01	0.543811	1	$6.15^{+0.82}_{-0.92}$	U	1
PSZ2 G228.50+34.95	–	09:22:15 +03:45:10	0.2701	1	$5.78^{+0.51}_{-0.58}$	cH	1
PSZ2 G230.73+27.70	–	09:01:29 −01:39:30	0.29435	1	$4.96^{+0.57}_{-0.61}$	–	–
PSZ2 G231.79+31.48	Abell 776	09:16:14 −00:24:42	0.332405	1	$4.87^{+0.63}_{-0.66}$	R+H	1
PSZ2 G232.84+38.13	Abell 847	09:40:27 +02:28:19	0.1508	1	$3.43^{+0.38}_{-0.40}$	cR	1
PSZ2 G233.68+36.14	–	09:35:17 +00:49:06	0.356823	1	$5.48^{+0.65}_{-0.67}$	R+R+H	1
PSZ2 G236.92−26.65	Abell 3364	05:47:36 −31:52:23	0.1483	1	$4.89^{+0.29}_{-0.32}$	–	5
PSZ2 G239.27−26.01	MACS J0553.4-3342	05:53:24 −33:42:07	0.43	1	$8.77^{+0.44}_{-0.46}$	H	6,7
PSZ2 G241.79−24.01	Abell 3378	06:05:53 −35:18:33	0.1392	1	$5.59^{+0.20}_{-0.22}$	U+U	1
PSZ2 G241.98+19.56	–	08:57:49 −14:44:31	0.27	2	$4.44^{+0.52}_{-0.60}$	–	–
PSZ2 G254.52+08.27	–	08:51:30 −31:15:52	–	–	–	–	–
PSZ2 G260.80+06.71	–	09:05:12 −37:01:30	–	–	–	cR+cH	1
PSZ2 G262.36−25.15	Abell 3391	06:26:19 −53:41:20	0.0514	1	$2.82^{+0.14}_{-0.13}$	U	8
PSZ2 G263.14−23.41	Abell S592	06:38:54 −53:58:53	0.2266	1	$6.83^{+0.34}_{-0.31}$	H	7
PSZ2 G263.19−25.19	Abell 3395	06:27:09 −54:25:48	0.0506	1	$3.21^{+0.18}_{-0.19}$	U	8
PSZ2 G263.68−22.55	Abell 3404	06:45:29 −54:13:46	0.1644	1	$7.96^{+0.23}_{-0.21}$	H	4
PSZ2 G265.21−24.83	–	06:32:17 −56:08:51	0.054	1	$1.84^{+0.17}_{-0.17}$	–	–
PSZ2 G270.63−35.67	–	05:09:55 −61:17:15	0.313	1	$5.34^{+0.34}_{-0.34}$	–	–
PSZ2 G271.28−36.11	–	05:05:34 −61:44:28	0.25	1	$3.81^{+0.34}_{-0.38}$	–	–
PSZ2 G272.08−40.16	Abell 3266	04:31:14 −61:24:25	0.0589	1	$6.64^{+0.11}_{-0.12}$	R+U+H+U	9,10,11
PSZ2 G275.24−40.42	–	04:22:09 −63:35:16	–	–	–	–	–
PSZ2 G275.73−06.12	–	09:08:04 −56:41:42	–	–	–	–	–
PSZ2 G276.09−41.53	Abell 3230	04:10:39 −63:44:28	0.14	1	$2.88^{+0.27}_{-0.27}$	–	–

Table 2. Continued.

Cluster	Other name	Coordinates[a] (hh:mm:ss, dd:mm:ss)	z	z ref.[b]	$M_{SZ,500}$ ($\times 10^{14}$ M$_\odot$)	Source(s)[c]	Source(s) ref.[d]
PSZ2 G276.14−07.68	–	09:01:23 −58:01:50	–	–	–	–	–
PSZ2 G282.32−40.15	–	04:00:53 −68:33:05	–	–	–	–	–
PSZ2 G286.28−38.36	–	03:59:13 −72:05:50	0.307	1	$5.94^{+0.39}_{-0.40}$	H	1
PSZ2 G286.75−37.35	–	04:07:46 −72:57:42	0.47	1	$6.79^{+0.49}_{-0.53}$	H	1
PSZ2 G311.98+30.71	Abell 3558	13:27:58 −31:30:45	0.048	1	$4.79^{+0.17}_{-0.17}$	H	12
PSZ2 G313.33+30.29	Abell 3562	13:33:40 −31:43:04	0.049	1	$2.44^{+0.21}_{-0.24}$	H+B	13,12
PSZ2 G328.58−25.25	–	18:56:04 −66:56:26	0.1797	1	$3.82^{+0.44}_{-0.47}$	–	–
PSZ2 G331.96−45.74	Abell 3825	21:58:13 −60:24:46	0.075	1	$2.08^{+0.24}_{-0.24}$	–	–
PSZ2 G332.11−23.63	–	18:47:25 −63:28:01	–	–	–	–	–
PSZ2 G332.23−46.37	Abell 3827	22:01:53 −59:56:24	0.098	1	$5.77^{+0.18}_{-0.18}$	H	1
PSZ2 G332.29−23.57	–	18:47:12 −63:17:23	0.0146	1	$0.79^{+0.10}_{-0.10}$	–	–
PSZ2 G333.89−43.60	SPT-CL J2138-6007	21:37:50 −60:07:12	0.318	1	$6.66^{+0.47}_{-0.51}$	H	1
PSZ2 G335.58−46.44	Abell 3822	21:54:07 −57:51:47	0.076	1	$4.19^{+0.16}_{-0.18}$	H+R	1
PSZ2 G336.95−45.75	Abell 3806	21:46:31 −57:16:38	0.076	1	$2.47^{+0.21}_{-0.21}$	–	–
PSZ2 G337.99−33.61	–	20:14:43 −59:13:03	–	–	–	–	–
PSZ2 G339.74−51.08	–	22:15:02 −53:21:21	–	–	–	–	–
PSZ2 G340.35−42.80	–	21:20:26 −55:56:16	–	–	–	–	–
PSZ2 G341.19−36.12	Abell 3685	20:32:16 −56:26:07	0.284	1	$5.74^{+0.56}_{-0.59}$	R+R	14
PSZ2 G341.44−40.19	Abell 3732	21:01:01 −55:43:00	0.25	1	$4.77^{+0.45}_{-0.46}$	–	–
PSZ2 G342.33−34.93	SPT-CL J2023-5535	20:23:25 −55:34:30	0.232	1	$6.68^{+0.45}_{-0.43}$	R+R+H	15
PSZ2 G342.62−39.60	Abell 3718	20:55:53 −54:54:54	0.139	1	$3.01^{+0.33}_{-0.35}$	U	16
PSZ2 G345.38−39.32	Abell 3716S	20:52:13 −52:50:12	0.044831	1	$1.81^{+0.18}_{-0.18}$	–	–
PSZ2 G345.82−34.29	Abell S861	20:18:49 −52:42:55	0.0505	1	$1.84^{+0.21}_{-0.16}$	–	–
PSZ2 G346.86−45.38	Abell 3771	21:29:48 −50:46:37	0.0796	1	$2.03^{+0.26}_{-0.27}$	H	1
PSZ2 G347.58−35.35	Abell S871	20:25:49 −51:16:38	0.22	1	$4.33^{+0.43}_{-0.45}$	cH	1

Notes.
[a]Coordinates reported in the PSZ2 catalogue.
[b]Reference for the cluster redshift. 1: Planck Collaboration et al. (2016a); 2: Aguado-Barahona et al. (2019); 3: Maturi et al. (2019); 4: Bleem et al. (2020).
[c]Detected sources, including: radio halo (any size, H), relic (R), miscellaneous diffuse emission (U), candidate object (c), '-' indicates no clear diffuse emission aside from active radio galaxies.
[d]References for detections of radio emission. 1: this work; 2: Slee et al. (2001); 3: Xie et al. (2020); 4: Duchesne et al. (2021b); 5: Knowles et al. (2022); 6: Bonafede et al. (2012); 7: Wilber et al. (2020); 8: Brüggen et al. (2021); 9: Murphy (1999); 10: Duchesne et al. (2022); 11: Riseley et al. (2022b); 12: Venturi et al. (2022); 13: Venturi et al. (2003); 14: Duchesne et al. (2021a); 15: HyeongHan et al. (2020); 16: Loi et al. (2023).

Following the self-calibration, we create a range of images:

1. Uniform image (highest resolution),
2. Robust 0.0 image (high resolution with sensitivity to extended structure),
3. Robust +0.25 image (as above, but generally more suitable for extended emission, depending on (u, v) coverage),
4. Robust +0.25 image, with Gaussian taper corresponding to 100 kpc (25–50 kpc if $z < 0.09$),
5. Robust +0.25 image, with Gaussian taper corresponding to 250 kpc (63–125 kpc if $z < 0.09$).

Note that this is similar to the image set created by BSC22 for their work with the LoTSS-DR2, though we optimize the weighting and tapering scales for the lower-resolution ASKAP data. Generally the first three images are to provide a range of reference images at high resolution while retaining sensitivity to extended sources, and the tapered, low-resolution maps provide better sensitivity to large-scale halos and relics. We then subtract compact emission from the visibility datasets by imaging with data with a (u, v) cut to remove emission on physical scales < 250 kpc (between 63–125 kpc if $z < 0.09$, depending on cluster). After subtraction of the compact emission model in the (u, v) data, we re-image the residual datasets following the previous round of imaging, excluding the robust 0.0 image.

3.1.2 Modelling the ASKAP primary beams

The 36 primary beams of the PAFs are formed by adjusting weights to maximise SNR while observing the Sun (Hotan et al., 2021). This process is undertaken every 1–2 months, and can create primary beam responses that shift in position by $\approx$ arcmin and change shape slightly. These changes can result in a factor of two difference to the response towards the beam edges (Duchesne et al., 2023a). ASKAP now measures the primary beam responses via holographic measurements while observing PKS J0408−6544. During most early science and commissioning, appropriate holographic measurements were not available and so a 2-D circular Gaussian model was assumed for primary beam correction and
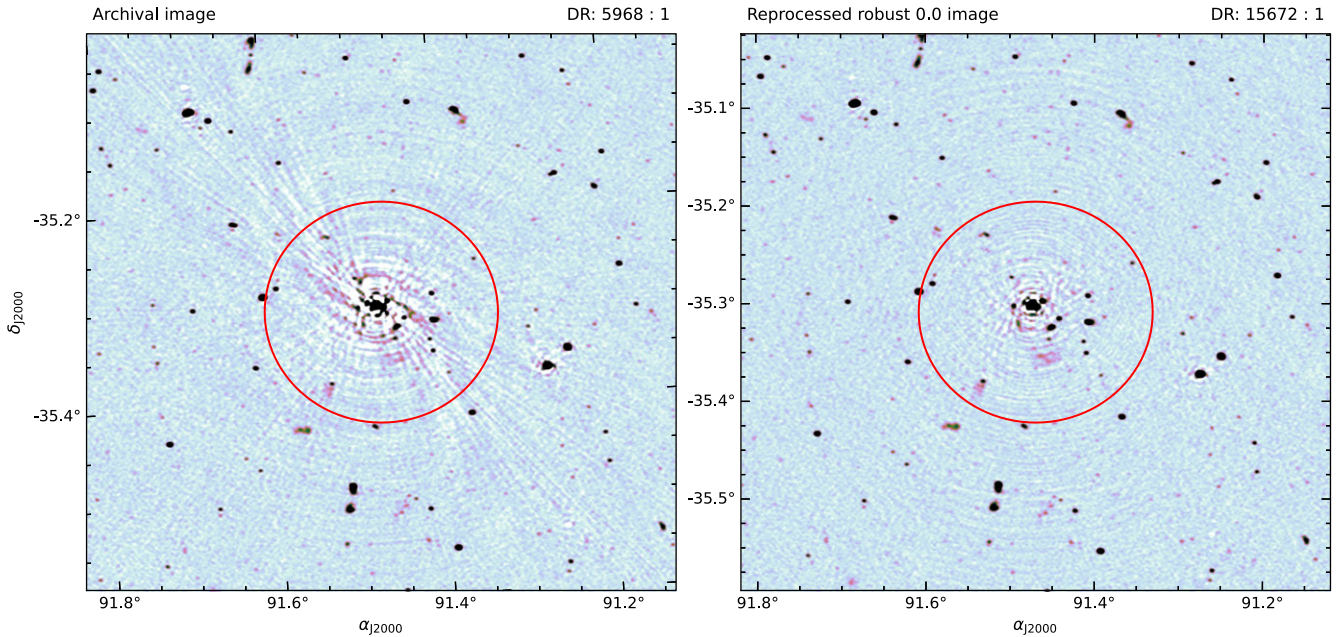
Figure 3. PSZ2 G241.79−24.01 in beam 5 of SB9596 in the archival image (*left*) and the phase-rotated and self-calibrated robust 0.0 image (*right*). The dynamic range for each image is shown in the top right of each panel. The red circle is centred on PSZ2 G241.79−24.01 and has a radius of 1 Mpc at the cluster's redshift ($z = 0.1392$). The linear colour scale is the same in each panel and shown in the range $[− 150, 1000]$ μJy beam^{-1}.

mosaicking[i]. This was found to be inadequate, particularly at the beam edges (McConnell et al., 2020). While resulting per-beam brightness scale errors can average out in the centre of an ASKAP image (formed via linear mosaic of all PAF beams), tile edges and individual beam images will retain these significant errors.

For consistency we opt to measure an in-field primary beam response for all observations. We created a global sky model from the existing RACS source-lists. At present, RACS has completed two sub-surveys, one at 887.5 MHz (RACS-low; McConnell et al., 2020; Hale et al., 2021) and the other at 1367.5 MHz (RACS-mid; Duchesne et al., 2023a). All imaging data products for RACS-low and RACS-mid are available through CASDA[j]. The sky model is created by merging the existing per-observation source-lists from RACS-low and RACS-mid[k]. These source-lists were created using the `selavy` source-finding software during the processing of the surveys, which decomposes grouped pixels ('sources') into 2-D Gaussian components. For this purpose, we use the 'component' lists to represent individual sources. The source-lists are retrieved from CASDA for each survey. We merge the RACS-low and RACS-mid source-lists separately, removing duplicated sources in overlap regions. This duplicate removal simply matches sources within their respective reported angular size in each observation that comprises the overlap regions. If a source is detected in two or more source-lists based on this criterion, we take the

source that has the smallest separation from its tile centre. This process results in 3 313 521 components for RACS-low and 3 916 193 components for RACS-mid.

With separate merged source-lists for RACS-low and RACS-mid, we perform a cross-match using `match_catalogues`[l] accepting a maximum separation of 10 arcsec and excluding sources if they have neighbours within 25 arcsec. This yields 2 088 670 sources. We then calculated two-point spectral indices for every source, following

$$\alpha = \frac{\log_{10} (S_{\text{RACS-low}}/S_{\text{RACS-mid}})}{\log_{10} (887.5/1367.5)}, \tag{1}$$

where $S_{\text{RACS-low}}$ and $S_{\text{RACS-mid}}$ are the RACS-low and RACS-mid integrated flux densities for the given source. We clip the catalogue where sources have α outside of the range $[− 3, 2]$ and where sources have integrated flux densities $< 10\,\sigma_{\text{rms}}$ in the respectively catalogues. This results in a final sky model with 1 092 183 sources with spectral indices. The sky model has a median spectral index of $\approx −0.84$.

The apparent brightness template image is used to create the primary beam response. We generate a source-list using the source-finder PyBDSF[m] (Mohan & Rafferty, 2015) for each template beam image, and cross-match these per-beam source lists to the RACS sky model. We restrict the match to sources within 2.25 deg of the beam centre to ensure we are not matching sources in the primary beam sidelobes (which are imaged). Additionally, we restrict the per-beam source-list to compact components, with integrated to peak flux density ratios of < 1.2. We use `flux_warp` to generate the primary beam model, by taking the sky model cross-match results, extrapolating to the

---

[i]The first regularly scheduled holography observation was SB34422 – at the end of 2021 – and prior to that most observations did not have a holography observation that corresponded to the PAF beam-former weights used for that particular time period.

[j]Under the RACS DOI for catalogue data products: https://doi.org/10.25919/1khs-c716.

[k]While a 25 arcsec resolution catalogue is available for RACS-low (Hale et al., 2021), we opt to create our own catalogue for this work to retain the highest-possible resolution across the survey to match the RACS-mid data. Similarly, all-sky RACS-mid catalogues are available (Duchesne et al., 2023b), but were not available at the time of processing these data.

[l]Packaged as part of `flux_warp` (Duchesne et al., 2020).
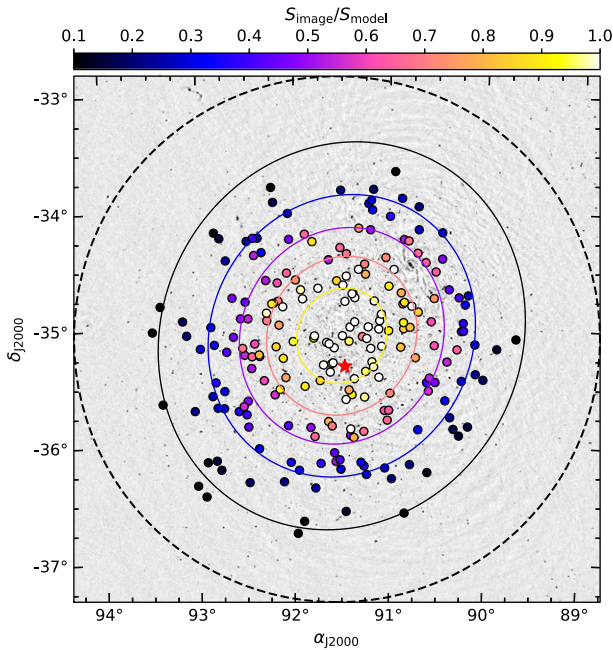[m]https://github.com/lofar-astron/PyBDSF.

Figure 4. Example beam 5 from SB9596 – a corner beam in the `closepack36` footprint. The background is the template image prior to directional self-calibration and source subtraction, used to generate the beam model. Overlaid are the sources used in modelling, coloured by the ratio of the measured flux density to the model flux density ($S_{\mathrm{image}}/S_{\mathrm{model}}$). Also overlaid are contours from the model beam, in levels of [0.1, 0.3, 0.5, 0.7, 0.9]. The larger dashed, black circle indicates the 2.25-deg radius within which sources are selected. The red star indicates the location of PSZ2 G241.79−24.01.

relevant frequency, and fitting a 2-D elliptical Gaussian model to the ratio $S_{\mathrm{image}}/S_{\mathrm{sky\ model}}$. While Duchesne et al. (2023a) found Zernike polynomial models represented the mid-band beams more accurately than 2-D Gaussian models, the fitted elliptical Gaussian is sufficiently accurate for the main lobe within 0.75 deg for the low-band ASKAP data. An example beam model is shown in Figure 4 along with the calibrator sources used in generating the model. We use these models for primary beam correction. For clusters with multiple beams, we form a linear mosaic of the beam images as in the usual ASKAPSoft processing, applying the primary beam responses and weighting the co-addition by the square of the primary beam response.

As an estimate of the uncertainty in the brightness scale, ξ_{scale}, of the mosaicked ASKAP images, we take the quadrature sum of standard deviations of the residuals ($\sigma_{b,\mathrm{residual}}$) from the calibrator sources used in generating the individual 2-D Gaussian beam models. In addition to the beam model uncertainty, we also add the uncertainties from the RACS-low and RACS-mid brightness scales, which are 7% (McConnell et al., 2020) and 6% (Duchesne et al., 2023a) in this case, respectively. In total, the brightness scale uncertainty is then

$$\xi_{\mathrm{scale}}^2 = 0.07^2 + 0.06^2 + \sum_b^{N_{\mathrm{beams}}} \sigma_{b,\mathrm{residual}}{}^2. \qquad (2)$$

Only the residuals from calibrator sources with a model beam attenuation of ≥ 0.1 are included as the images are clipped for attenuation < 0.1.

3.1.3 A comparison of the new and archival images

To compare the new, re-processed images with the archival images, we look at the rms noise (σ_{rms}) and peak flux density

(S_{max}) within 1 Mpc of the cluster centres, and by extension the dynamic range (DR $= S_{\mathrm{max}}/\sigma_{\mathrm{rms}}$). For this comparison we use the re-processed robust 0.0 image as that image weighting is generally the closest match to the weighting used by ASKAPsoft. Figure 5 shows the comparison of the three quantities, with each cluster (and resulting image) coloured according to the cluster's declination. In general, there is a marginal improvement in the overall DR of the re-processed images (median $\mathrm{DR_{new}/DR_{archival}} = 1.08^{+0.17}_{-0.07}$, with uncertainties drawn from the 16th and 84th percentiles of the distribution), though not all clusters see an improvement. Some of the largest improvements are in the equatorial fields, which is simply a combination of difference in image weighting (where robust 0.0 is not as close to the ASKAPsoft weighting) and some differences in the treatment of w-terms between WSClean (via wgridder) and the ASKAPSoft w-projection implementation[n]. In cases where the re-processed image has lower DR, this is generally the result of a difference of image PSF. There is also some variation to the brightness scales between re-processed and archival images due to the different primary beam models used, illustrated in the centre panel of Figure 5, though there is general agreement with median $S_{\mathrm{max}}^{\mathrm{new}}/S_{\mathrm{max}}^{\mathrm{archival}} = 1.00^{+0.07}_{-0.09}$). For consistency we only use the re-processed images for analysis in this work.

In Appendix A we also summarise the rms noise (Table A1) and PSF (Table A2) of the five re-processed images (robust 0.0, robust $+0.25$, uniform, and the two tapered images) and archival images of each cluster. While the images used in this work are not directly output from the ASKAPsoft pipeline, we suggest they form an approximate representation of the images being produced for the main EMU survey that is currently underway.

3.1.4 Image-based angular scale filtering

While not originally performed on these archival datasets, as part of the EMU processing pipeline, the main survey images go through an additional image-based angular scale filtering. This filtering is based on the multi-resolution filtering method described by Rudnick (2002), and employs maximum and minimum sliding box filters at two angular scales to remove features in images that fall outside of the two chosen angular scales. We introduce a python implementation, DiffuseFilter[o]. This implementation has a curated mode for filtering EMU images that removes angular scales outside of $3\,\theta_{\mathrm{M}} \lesssim \theta_{\mathrm{scale}} \lesssim 27\,\theta_{\mathrm{M}}$, where θ_{M} is the full width at half maximum of the major axis of the image PSF. The smaller scale typically removes compact emission unassociated with diffuse cluster sources, and the larger scale is used to remove large-scale ripples. The ripples are generally a combination of undeconvolved sidelobes of off-axis extended (usually Galactic) emission, solar interference, and generally the poorer calibration of short baselines.

Similar angular scale filtering has been used in previous cluster studies to identify diffuse radio sources within images with a large number of compact sources (e.g. Knowles et al., 2022; Venturi et al., 2022) and will be a feature of the upcoming EMU survey. For assessing expectations of the full EMU survey, we opt to generate these filtered maps for the robust $+0.25$ images alongside the (u, v)-plane subtraction method outlined earlier. We also create a separate filtered map similar to the (u, v)-plane subtraction method, removing similar scales only as a point of comparison. Figure 6

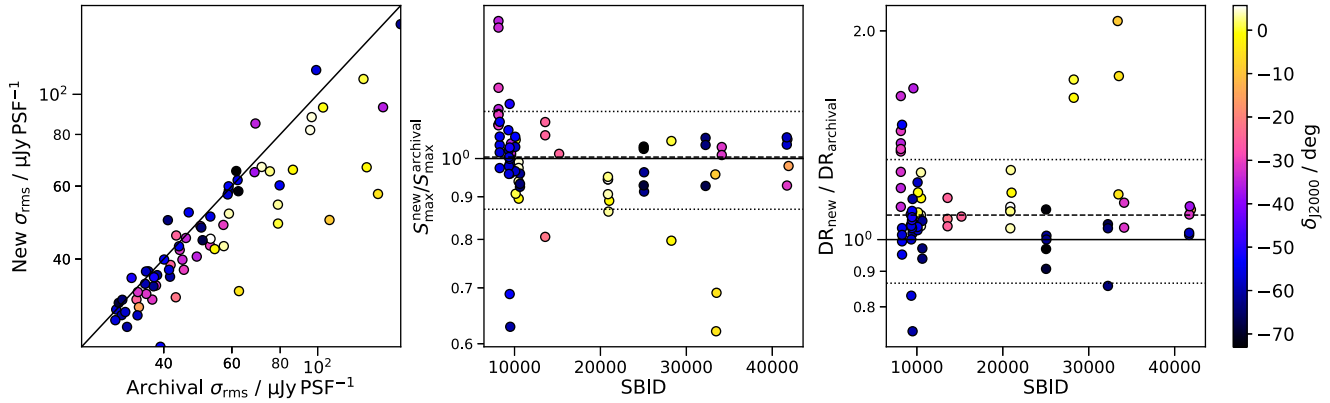[n] https://www.atnf.csiro.au/computing/software/askapsoft/sdp/docs/current/calim/gridder.html.
[o] https://gitlab.com/Sunmish/diffusefilter.

Figure 5. Comparison of the rms noise (σ_{rms}, *left*), peak flux density (S_{ms}, as a function of SBID, *centre*), and dynamic range (DR, as a function of SBID, *right*) calculated within 1 Mpc of cluster centres between the new re-processed, robust 0.0 images and the original archival images as they appear on CASDA. The points are coloured by the cluster declination. The solid black lines indicate equal values between the images.

shows some examples of the different filter methods on a selection of clusters. A comparison of the (u, v)-plane and image-plane filtering methods is presented in Section 5.3.

3.2 Optical and X-ray data

We use optical data to inform positions of clusters and of any potential hosts to candidate diffuse radio sources. We typically only collect a single optical dataset per cluster, depending on availability and the sensitivity necessary. The optical data include images from the Dark Energy Survey (DES) data release 2 (DES DR2; Flaugher et al., 2015; Abbott et al., 2018, 2021), the Pan-STARRS[p] survey (PS1; Tonry et al., 2012; Chambers et al., 2016), the Digitized Sky Survey (DSS2), and the Sloan Digitized Sky Survey data release 7 (SDSS DR7; Abazajian et al., 2009).

For associated X-ray observations, we query the *Chandra*[q] and *XMM*-Newton[r] online archives for observations of the PSZ2 clusters in our sample. In total we find that 36 of the 71 PSZ2 clusters have existing *XMM*-Newton observations, which we make use of, and we also make use of *Chandra* observations for three additional clusters without *XMM-Newton* data. We used the standard pipeline data products, which are generally sufficient for this work. For the *XMM*-Newton pipeline[s] data products, we make use of the three-colour image generated from data taken by the European Photon Imaging Camera (EPIC; Turner et al., 2001; Strüder et al., 2001). For the *Chandra* pipeline data products, we use images from the Advanced CCD Imaging Spectrometer (ACIS) produced through standard data processing by the *Chandra* X-ray Centre[t]. Optical and X-ray images are only used for qualitative analysis.

4. Survey results

The clusters in our sample that are found to host diffuse emission are reported in Table 3 with measured and derived quantities where possible. The classification scheme we follow and the source measurements are described in the following sections, along with notes on the individual systems.

4.1 Classification scheme

For classification of sources, we largely follow the scheme outlined by BSC22 though we relax the criteria for considering objects 'candidate' sources. The classifications generally only consider three types of emission:

1. *Radio halo (H).* A diffuse, extended radio source located at the centre of a cluster. For the purpose of classifying diffuse radio sources, the cluster centre can be considered the X-ray centroid (if there is X-ray data available), the SZ peak (the location of the PSZ2 coordinates), or the optical centre (as seen in the available optical images), with preference in that order. No distinction is made between different types of radio halos (mega, giant, mini).

2. *Radio relic (R).* An extended radio source towards the periphery of a cluster, assuming the same concept of cluster centre as described above. We relax the sharp surface brightness criterion from BSC22, noting relics viewed at different angles can have a range of morphologies (e.g. Skillman et al., 2013; Wittor et al., 2023) and that the lower resolution of the ASKAP observations is less able to detect such features in the images. We require that any sources we classify as radio relics do not have obvious features of a radio galaxy (lobes, hotspot, AGN core, optical host). We do not require morphological features such as 'arc-like shape' as this is largely dependent on the geometry of the merger/projection as mentioned above. While we do find the projected size of the detected relics to be > 300 kpc in line with BSC22, we did not use this criterion.

3. *Unclassified/other diffuse emission (U).* An extended radio source that does not fit into the radio halo and relic classifications, but is not obviously a radio galaxy (or similar active radio source) and does not have an obvious optical identification. This classification collects diffuse radio sources such as phoenices/(revived) fossil plasmas (Kempner et al., 2004). We do not distinguish between

(i) PSZ2 G272.08−40.16 (Abell 3266).

(ii) PSZ2 G241.79−24.01 (Abell 3378).
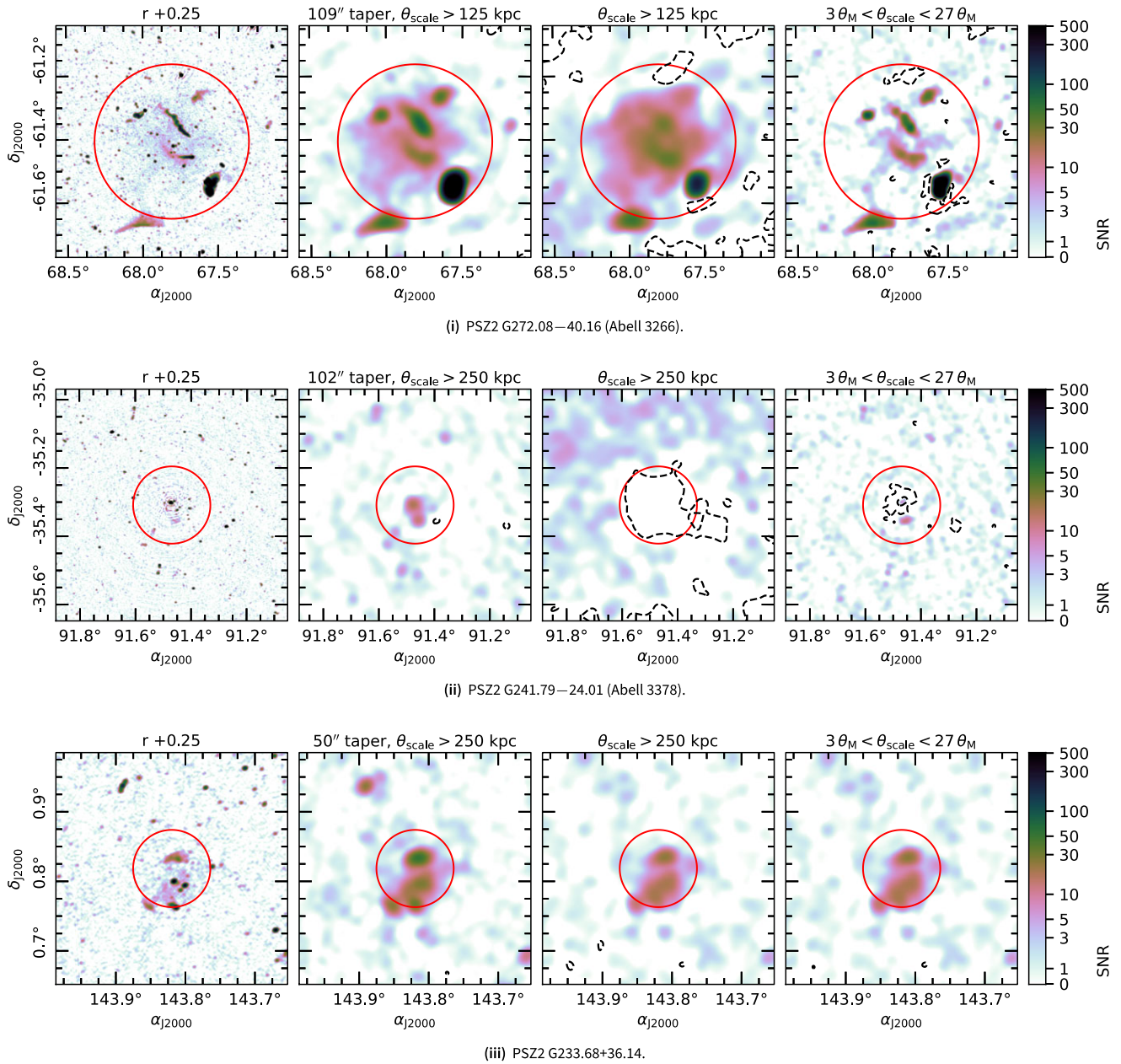
(iii) PSZ2 G233.68+36.14.

Figure 6. Examples of angular scale filtering. *Left.* Robust +0.25 reference image. *Centre left.* (u, v)-filtered image, with corresponding taper applied during imaging. *Centre right.* Image-based filtering using the same scale as the (u, v) filtering. Note the image is convolved to the same resolution as the filter. *Right.* Image-based filtering used for the EMU survey. Note that the image is convolved to the resolution of the lower filter. The red circles are centred on the cluster with a 1 Mpc radius. Black, dashed contours are drawn on the filtered images at $-3\,\sigma_{rms}$.

these types of emission as there is no meaningful way to do so with the single frequency ASKAP data available.

4. *Nothing applicable (NA).* Clusters that do not feature a source that can be classified as above are classified as 'NA'. Note this applies to the cluster as a whole rather than individual sources as opposed to the other classifiers.

A halo or relic might be considered a candidate (cH, cR) if it is not clear whether the emission is from other unsubtracted radio sources in the cluster. While this classification scheme is similar to that used by BSC22, it is not as rigorous. Hoang et al. (2022)

use a similar visual classification approach rather than a rigorous decision tree looking at non-PSZ2 clusters in the LoTSS-DR2 data. They find similar results for radio halos and relics when comparing the classification methods using the same decision tree. For other sources (the unclassified diffuse sources and AGN-related emission) the two approaches may be less consistent.

Figure 7 shows a set of images used for 'quick-look' classification of the sources (using PSZ2 G008.31−64.74 as an example) and highlights the range of images available for each cluster. Generally, images with interesting sources are followed-up with more in-depth inspection of the FITS images. In Figure 8 we show an

Table 3. Measured properties of the (candidate) diffuse radio sources detected in the PSZ2 clusters.

Cluster	z^a	Source	New?	ν^b (MHz)	Taper^c (kpc)	ξ_{scale}	Notes^d	S_{int} (mJy)	S_{sub} (mJy)	Model	S_{model} (mJy)	Luminosity^e ($\times 10^{24}$ W Hz^{-1})	LAS^f (arcmin)	LLS^g (kpc)	Dist.^{h} (kpc)
PSZ2 G008.31−64.74	0.312	R (SE)	√	887.5	–	0.22	–	11.2 ± 2.5	–	–	–	3.74 ± 0.30	3.7	1 000	2 000
PSZ2 G008.31−64.74	0.312	R (NW)	√	887.5	–	0.22	–	11.2 ± 2.6	–	–	–	3.72 ± 0.36	4.6	1 300	1 200
PSZ2 G008.31−64.74	0.312	cH	√	887.5	250	0.22	–	10.3 ± 2.8	1.5	circle	21.9 ± 9.1	7.3 ± 3.1	5.5	1 500	–
PSZ2 G011.06−63.84	0.224	cH	√	887.5	100	0.21	–	5.4 ± 1.4	1.1	skewed	5.4 ± 1.9	0.84 ± 0.30	3.0	650	–
PSZ2 G011.92−63.53	0.24	H	√	887.5	100	0.18	–	7.7 ± 1.6	0.27	skewed	8.9 ± 5.0	1.62 ± 0.90	6.8	1 500	–
PSZ2 G110.28−87.48	0.52	H	√	943.5	100	0.29	–	2.97 ± 0.96	0.16	skewed	3.4 ± 1.2	3.9 ± 1.4	2.7	1 000	–
PSZ2 G149.63−84.19	0.0569	U (S)	×	943.5	–	0.25	–	18.7 ± 4.6	–	–	–	0.1463 ± 0.0028	3.3	220	210
PSZ2 G149.63−84.19	0.0569	U (N)	×	943.5	–	0.25	conf.	337 ± 89	–	–	–	2.818 ± 0.031	1.7	110	150
PSZ2 G172.98−53.55	0.373	H	×	943.5	100	0.25	conf.	5.6 ± 1.7	0.63	skewed	6.9 ± 3.0	3.5 ± 1.6	3.2	1 000	–
PSZ2 G175.69−85.98	0.23	H	×	943.5	100	0.33	–	22.6 ± 8.3	1.8	skewed	22.9 ± 8.7	3.8 ± 1.4	7.1	1 600	–
PSZ2 G219.88+22.83	0.232813	cR	√	887.5	100	0.18	–	14.5 ± 2.9	0.66	–	–	2.58 ± 0.19	5.6	1 200	2 500
PSZ2 G223.47+26.85	0.3269	H	√	887.5	250	0.14	–	3.24 ± 0.69	0.25	skewed	3.7 ± 2.0	1.38 ± 0.74	3.8	1 100	–
PSZ2 G225.48+29.41	0.203	H	√	943.5	100	0.27	conf.	8.7 ± 2.9	1.6	skewed	5.3 ± 2.1	0.65 ± 0.26	5.1	1 000	–
PSZ2 G227.59+22.98	0.28085	cR (NW)	√	887.5	100	0.24	–	2.88 ± 0.76	–	–	–	0.750 ± 0.087	2.2	570	1 200
PSZ2 G227.59+22.98	0.28085	cR (SE)	√	887.5	100	0.24	–	1.42 ± 0.40	–	–	–	0.369 ± 0.055	1.9	480	1 500
PSZ2 G227.89+36.58	0.4616	cH	√	887.5	100	0.21	conf.	1.30 ± 0.33	–	–	–	1.11 ± 0.19	1.6	560	–
PSZ2 G228.38+38.58	0.543811	U	√	887.5	–	0.18	–	1.26 ± 0.28	–	–	–	1.61 ± 0.26	1.5	570	620
PSZ2 G228.50+34.95	0.2701	cH	√	887.5	100	0.20	–	1.77 ± 0.46	0.036	circle	8.8 ± 2.8	2.10 ± 0.67	2.6	640	–
PSZ2 G231.79+31.48	0.332405	R	√	887.5	–	0.23	–	16.1 ± 4.3	2.4	–	–	7.28 ± 0.46	3.3	930	790
PSZ2 G231.79+31.48	0.332405	H	√	887.5	250	0.23	conf.	7.8 ± 5.8	1.1	ellipse	5.1 ± 2.0	1.99 ± 0.77	6.0	1 700	–
PSZ2 G232.84+38.13	0.1508	cR	√	887.5	100	0.18	conf.	26.2 ± 4.9	–	–	–	1.722 ± 0.068	6.0	940	580
PSZ2 G232.84+38.13	0.1508	U	√	887.5	–	0.18	–	9.8 ± 1.8	–	–	–	0.622 ± 0.023	1.4	230	74
PSZ2 G233.68+36.14	0.356823	R (N)	√	887.5	–	0.18	–	15.2 ± 2.8	–	–	–	6.97 ± 0.46	2.9	870	290
PSZ2 G233.68+36.14	0.356823	R (S)	√	887.5	–	0.18	–	6.9 ± 1.3	–	–	–	3.17 ± 0.25	2.2	650	1 100
PSZ2 G233.68+36.14	0.356823	H	√	887.5	–	0.18	conf.	19.8 ± 4.3	1.9	skewed	19.7 ± 5.5	9.0 ± 2.6	4.6	1 400	–
PSZ2 G239.27−26.01	0.43	H	×	943.5	100	0.21	–	15.4 ± 3.4	0.72	skewed	14.3 ± 3.2	10.3 ± 2.4	4.5	1 500	–
PSZ2 G241.79−24.01	0.1392	U (S)	√	943.5	100	0.17	–	6.4 ± 1.2	0.30	–	–	0.360 ± 0.024	2.7	390	390
PSZ2 G241.79−24.01	0.1392	U (central)	√	943.5	100	0.17	–	9.8 ± 2.2	2.2	–	–	0.651 ± 0.033	4.1	600	37
PSZ2 G260.80+06.71	0.2∗	cR	√	943.5	100	0.26	–	64 ± 17	–	–	–	–	5.7	–	–
PSZ2 G260.80+06.71	0.2∗	cH	√	943.5	100	0.26	–	11.6 ± 3.3	0.59	skewed	10.7 ± 5.2	–	7.2	–	–
PSZ2 G262.36−25.15	0.0514	U	×	1 013.5	–	0.30	–	7.6 ± 2.3	–	–	–	0.0479 ± 0.0026	2.2	130	730
PSZ2 G263.14−23.41	0.2266	H	×	1 013.5	100	0.26	–	13.9 ± 4.5	2.8	skewed	12.5 ± 4.9	1.97 ± 0.78	4.4	970	–
PSZ2 G263.19−25.19	0.0506	U	×	1 013.5	–	0.20	conf.	345 ± 69	–	–	–	2.109 ± 0.024	8.7	510	640
PSZ2 G263.68−22.55	0.1644	H	×	1 013.5	250	0.41	–	28 ± 14	4.0	skewed	30 ± 15	2.3 ± 1.2	8.4	1 400	–
PSZ2 G272.08−40.16	0.0589	R	×	943.5	50	0.19	–	74 ± 14	–	–	–	0.625 ± 0.012	10.	700	1 100
PSZ2 G272.08−40.16	0.0589	U (N)	×	943.5	50	0.19	–	33.8 ± 6.6	–	–	–	0.2843 ± 0.0098	6.4	440	670
PSZ2 G272.08−40.16	0.0589	H	×	943.5	50	0.19	conf.	256 ± 58	28	skewed	161 ± 45	1.35 ± 0.38	24	1 600	–
PSZ2 G272.08−40.16	0.0589	U (W)	×	943.5	–	0.19	conf.	3.40 ± 0.74	–	–	–	0.0286 ± 0.0028	2.2	150	870
PSZ2 G286.28−38.36	0.307	H	√	887.5	100	0.20	–	11.8 ± 2.8	1.8	skewed	12.8 ± 3.9	4.1 ± 1.3	5.5	1 500	–
PSZ2 G286.75−37.35	0.47	H	√	887.5	100	0.14	–	8.3 ± 1.4	0.57	circle	8.9 ± 1.9	7.9 ± 1.8	3.8	1 300	–
PSZ2 G311.98+30.71	0.048	H	×	943.5	100	0.20	–	30.2 ± 7.7	4.9	skewed	44 ± 15	0.242 ± 0.082	11	600	–
PSZ2 G313.33+30.29	0.049	H	×	943.5	100	0.26	–	49 ± 16	8.8	skewed	70 ± 27	0.40 ± 0.15	12	700	–
PSZ2 G313.33+30.29	0.049	U	×	943.5	100	0.26	–	35 ± 10	1.8	–	–	0.215 ± 0.014	8.1	470	1 100
PSZ2 G313.33+30.29	0.049	Bridge	×	943.5	100	0.26	conf.	73 ± 45	–	–	–	0.977 ± 0.044	28	1 600	–
PSZ2 G332.23−46.37	0.098	H	√	943.5	100	0.13	–	8.1 ± 1.3	1.2	skewed	9.7 ± 2.3	0.241 ± 0.058	5.7	620	–
PSZ2 G333.89−43.60	0.318	H	√	943.5	100	0.22	conf.	4.4 ± 1.2	0.57	skewed	4.4 ± 1.7	1.52 ± 0.60	3.5	980	–

Table 3. Continued.

Cluster	z^a	Source	New?	ν^b (MHz)	Taper^c (kpc)	ξ_{scale}	Notes^d	S_{int} (mJy)	S_{sub} (mJy)	Model	S_{model} (mJy)	Luminosity^e ($\times 10^{24}$ W Hz^{-1})	LAS^f (arcmin)	LLS^g (kpc)	Dist.^{h} (kpc)
PSZ2 G335.58−46.44	0.076	H	√	943.5	100	0.19	–	38.1 ± 8.1	2.9	skewed	55 ± 13	0.79 ± 0.19	12	1 100	–
PSZ2 G335.58−46.44	0.076	R	√	943.5	–	0.19	–	17.7 ± 3.4	–	–	–	0.2548 ± 0.0071	4.2	360	470
PSZ2 G341.19−36.12	0.284	R (NW)	×	943.5	–	0.21	conf.	3.48 ± 0.98	0.22	–	–	1.200 ± 0.098	3.0	760	450
PSZ2 G341.19−36.12	0.284	R (SE)	×	943.5	–	0.21	conf.	7.3 ± 1.8	0.42	–	–	2.22 ± 0.15	3.8	960	1 100
PSZ2 G342.33−34.93	0.232	R (W)	×	943.5	–	0.21	–	15.8 ± 3.3	–	–	–	2.64 ± 0.13	2.9	640	640
PSZ2 G342.33−34.93	0.232	R (E)	×	943.5	100	0.21	–	3.22 ± 0.74	–	–	–	0.539 ± 0.055	2.8	630	780
PSZ2 G342.33−34.93	0.232	H	×	943.5	100	0.21	conf.	32.8 ± 7.7	4.0	skewed	53 ± 14	8.9 ± 2.4	5.7	1 300	–
PSZ2 G342.62−39.60	0.139	U	×	943.5	–	0.26	conf.	12.5 ± 4.0	2.2	–	–	0.818 ± 0.039	4.1	600	150
PSZ2 G346.86−45.38	0.0796	H	√	943.5	100	0.16	–	7.6 ± 1.6	1.4	skewed	7.2 ± 2.2	0.115 ± 0.035	4.8	430	–
PSZ2 G347.58−35.35	0.22	cH	√	943.5	–	0.24	–	4.0 ± 1.0	0.0027	skewed	6.1 ± 1.5	0.90 ± 0.23	2.4	520	–

^{a}'*' indicates assumed redshift.
^{b}Image frequency.
^{c}Image taper used. '-' if the standard robust $+0.25$ image is used (see Section 3.1.1 for details).
^{d}'conf.' refers to sources that are blended with either residual emission after subtraction or with other diffuse sources.
^{e}At the image frequency, assuming $\alpha = -1.2 \pm 0.2$ for all sources.
^{f}Largest deconvolved angular scale (or extent) within 2σ contours.
^{g}Largest deconvolved linear scale (or extent) from the LAS at the reported redshift.
^{h}Linear projected distance from the PSZ2 cluster centre.

example of the set of images provided in Appendix A for all clusters that highlight the main robust 0.25 image, the source-subtracted, tapered image, and any sources of interest.

4.2 Source measurements

Measured properties of sources are reported in Table 3 and relevant measurements are described below. When measuring properties of radio halos we make use of the compact source-subtracted [(u, v)-plane subtraction] robust 0.25 map with tapering. As relics and smaller-scale diffuse emission tend to have small-scale features, we generally make use of the non-filtered images for those sources to avoid loss of flux density. For relics/unclassified sources with embedded compact emission, we instead subtract the peak flux density of the intervening sources from the total integrated flux density measurements.

We define polygon regions that cover the sources of interest and first estimate the largest angular size (LAS) of the source using the largest angular separation between any pair of pixels within the region above. Figure 8(ii) [and Figures A1(i)–A(1xxi) in Appendix A] shows the line (grey, dashed) between the two selected pixels used to estimate the source sizes. We also make use of the polygon regions to determine the flux-weighted centroid of each source, and for relics and other unclassified diffuse emission we calculated the angular separation along with the project distance of the diffuse source from the cluster centre as reported in the PSZ2 catalogue.

For all diffuse cluster sources reported, we provide a measurement of the integrated flux density, S_{int}, at the frequency of the relevant ASKAP image, following

$$S_{int} = \sum_{n}^{N} S_n \left(\frac{|c_1 c_2| 4 \ln 2}{\pi \theta_M \theta_m} \right) \quad \text{Jy}, \tag{3}$$

where N is the number of image pixels comprising the integration region (optionally for pixels above a brightness threshold, e.g. $3\sigma_{rms}$), c_1 and c_2 are the pixel dimensions in R. A. and declination,

and θ_M and θ_m are the major and minor axes of the PSF. Associated uncertainties, σ_S, are calculated via

$$\sigma_S = \sqrt{N_{PSF}\sigma_{rms}^2 + (S_{int}\xi_{scale})^2} \quad \text{Jy}, \tag{4}$$

where N_{PSF} is the number of PSFs covering the full integration region, ξ_{scale} is the brightness scale uncertainty (Equation (2)).

After visual inspection of the compact source-subtracted datasets we find residual emission for some sources and suggest this creates a bias in the measurements for the radio halos. This scales with the number of compact sources subtracted and is generally more significant for fainter compact sources which are harder to image and subtract when imaging with a (u, v) cut. We define this flux density bias as

$$S_{sub} = 0.2 \left(1 - \frac{S'}{S} \right) S_{int} \quad \text{Jy}, \tag{5}$$

where S is the integrated flux density within the polygon region of the uniformly weighted image, and S' is the same measurement on the uniform map after compact source subtraction. By construction this is always less than 20% of the original integrated flux density measurement and is subtracted from measurements made using the (u, v)-filtered maps.

For the flux density measurement, we include all pixels within the polygon regions. Including all pixels within the polygon allows some reduction in bias of low-significance diffuse emission (e.g. Hales et al., 2012) and we assume the noise is symmetric and account for measurement of low-SNR pixels by including all pixels within the polygon in the estimation of σ_S (in Equation (4)). In Figure 9 we show the ratio of flux density measurements between this measurement technique and similar integration on pixels above $2\sigma_{rms}$ and $3\sigma_{rms}$ as a function of the largest angular size of the source measured within $2\sigma_{rms}$ contours. We also show the same flux density ratio between the integrated flux density and the model flux density for radio halos described in the following section. The measured flux density is always larger when including all pixels, but does not appreciably change with source size. Polygon regions used for measurements are shown on the
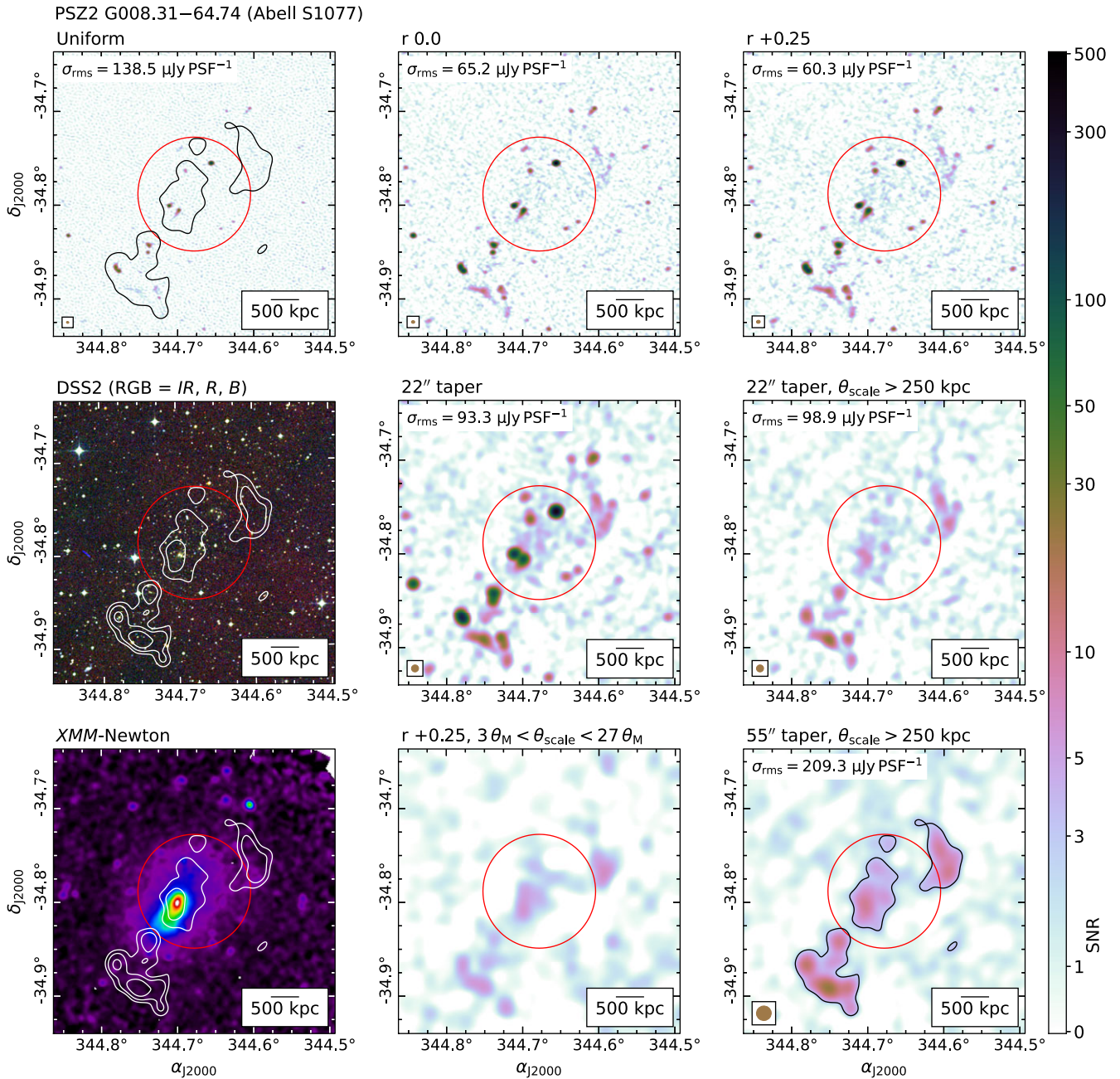
Figure 7. Example set of images used for identification of sources in PSZ2 G008.31−64.74. The colour scales in all radio images are linear between the range $[0, 3\,\sigma_{\text{rms}}]$ and logarithmic in the range $[3\,\sigma_{\text{rms}}, 500\,\sigma_{\text{rms}}]$. The white and black contours are of the bottom right image, and are drawn at $[3, 6, 12, 24, 48] \times \sigma_{\text{rms}}$ in the optical and X-ray panels and at $3\,\sigma_{\text{rms}}$ in other panels. The solid circle is centred on the reported PSZ2 coordinates and has a 1 Mpc radius at the cluster redshift. Clusters without a measured redshift are assumed to be at $z = 0.2$, and the circle is dashed in those cases. Clusters without publicly available *XMM*-Newton and *Chandra* observations are shown without an X-ray image. Images of all clusters are made available online. Note that the image-based filtering retains the resolution and brightness units as the original robust $+0.25$ map, and so appears with the same brightness scale as the original robust $+0.25$ image after filtering.

right panel of Figure 8(ii) for PSZ2 G008.31−64.74 and in Figures A1(i)−A1(lxxi) in Appendix A for the remaining clusters.

4.3 Radio halo models

To help with obtaining flux densities of radio halos, we use `Halo-FDCA` (Boxelaar et al., 2021) to fit a range of 2-D exponential

profiles to the surface brightness in the compact source-subtracted images. For each halo (and candidate halo) we use the same image used for integrated flux density measurements described in the previous section, and mask intervening sources/residual emission not associated with the radio halo. We then use `Halo-FDCA` to fit three profiles to each halo: a standard circular exponential profile (see e.g. Orrú et al., 2007; Murgia et al., 2009; Bonafede

(i) PSZ2 G006.16−69.49.
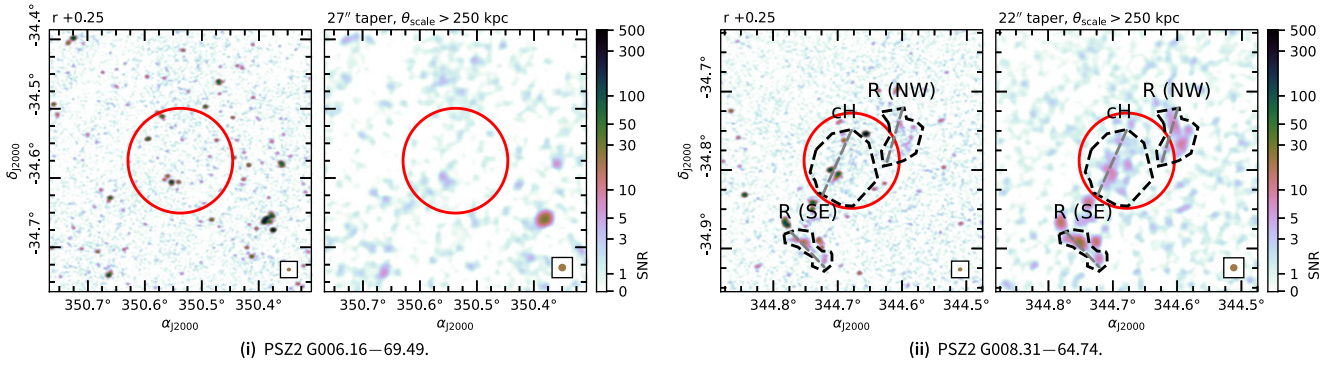
(ii) PSZ2 G008.31−64.74.

Figure 8. Example images of PSZ2 G006.16−69.49 (i) with no diffuse sources and PSZ2 G008.31−64.74 (ii) with two relics and a candidate halo. Similar images for all clusters are included in Appendix A. *Left panels.* The robust +0.25 reference image. *Right panels.* The robust +0.25 image, tapered, after subtraction of sources of scales < 250 kpc. In all panels, the red circle has a 1 Mpc radius at the redshift of the clusters (in Appendix A a dashed circle indicates an assumed redshift of 0.2). For clusters with diffuse emission, the dashed polygon regions indicate the diffuse sources of interest and are the regions used for integrated flux density measurements. The PSF of each image is shown in the bottom right corner.
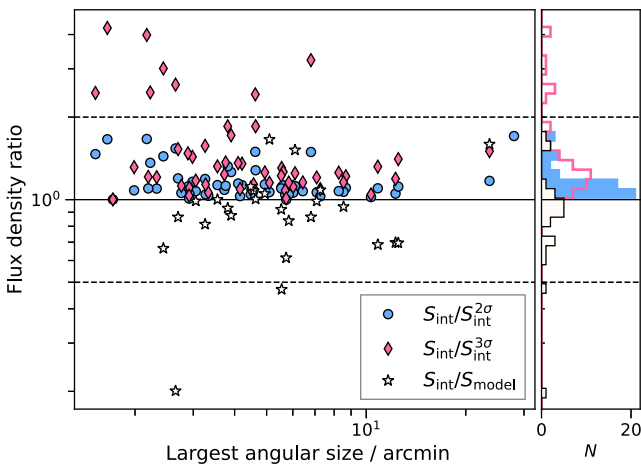
Figure 9. Flux density ratios as a function of largest angular size/extent. We show the comparison between full measurement (all pixels) and three alternatives: integration over $2\,\sigma_{rms}$ (blue, circles), $3\,\sigma_{rms}$ (pink, diamonds), and the model flux densities for radio halos (white, stars). A histogram of the distribution of the flux density ratios is also shown. The solid black line indicates a ratio of 1, and the dashed black lines are drawn at flux density ratios of 0.5 and 2.

et al., 2009), and generalized elliptical and skewed elliptical profiles (Boxelaar et al., 2021). After fitting, we use the reduced χ^2 as a simple model selection parameter. To obtain the model flux density, S_{model}, the fitted exponential profile is integrated out to three times the *e*-folding radius following BSC22.

In Figure 10 we show the results of fitting the radio halo models with Halo-FDCA in a low-SNR case [a circular model for the halo in PSZ2 G008.31−64.74, 10(i)] and a high-SNR case [a skewed model for the halo in PSZ2 G011.06−63.84, 10(ii)]. Equivalent images for other halos reported in this work are shown in Appendix B. The model flux densities and the selected models are reported in Table 3 alongside the integrated flux densities described in Section 4.2. We show the ratio of S_{int}/S_{model} for all halos in Figure 9, finding a median $S_{int}/S_{model} = 0.93^{+0.16}_{-0.24}$. Residual emission from partially subtracted sources or heavily confused clusters results in difference between the integration within polygon regions and integration of the model profile. For radio halo

power calculations, we use the model flux density rather than the integrated flux density measured within the polygon region unless otherwise stated.

4.4 Notes on individual systems

Each cluster hosting a diffuse source of interest is included in Table 3 along with measured properties and a note indicating if we are reporting the source for the first time. In the following, we include relevant notes about the individual clusters and the diffuse emission we detect.

4.4.1 PSZ2 G008.31–64.74 (Abell S1077)

Figure A1(ii). We report the detection of a double radio relic system (SE and NW), with additional residual emission at the cluster center that we consider a candidate radio halo. De Filippis et al. (2004) report a ≈ 1.5 arcmin soft X-ray tail of emission in *Chandra* data, in the direction of the newly discovered SE radio relic. De Filippis et al. (2004) also report two X-ray surface brightness and temperature discontinuities towards the NE of the cluster centre, though these are not coincident with the NW and SE radio relics detected here.

4.4.2 PSZ2 G011.06–63.84 (Abell 3934)

Figure A1(iii). We report a candidate radio halo in this cluster. The cluster has no deep X-ray observation available from neither *Chandra* nor XMM-*Newton*. There is a compact source at the centre of the emission which is often seen with mini-halos, though with a project linear size of 650 kpc (within $2\sigma_{rms}$ contours) the source is considerably larger than a traditional mini-halo.

4.4.3 PSZ2 G011.92–63.53 (SPT-CL J2251–3324)

Figure A1(iv). While no redshift is available in the PSZ2 catalogue, Bleem et al. (2020) report $z = 0.24$ for the cluster. We report the detection of 1.5-Mpc diffuse emission near the centre of the cluster present in both the (u, v)-plane compact source-subtracted map and the image-filtered map, which we consider a radio halo. There are presently no *Chandra* or XMM-Newton observations available. We note that there is a large redshift distribution in the general vicinity of the cluster, in the range $0.06 \lesssim z \lesssim 0.25$, indicating there may various clusters along this line of sight.
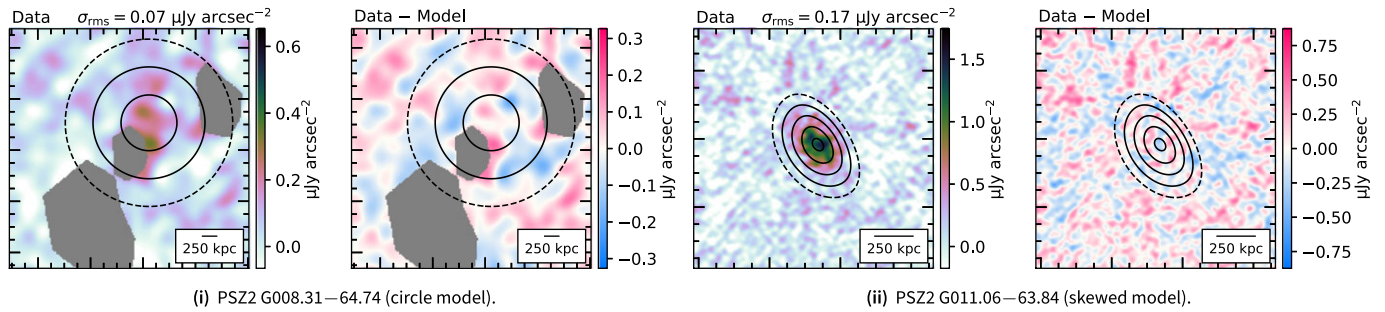
(i) PSZ2 G008.31−64.74 (circle model).   **(ii)** PSZ2 G011.06−63.84 (skewed model).

Figure 10. Example radio halo models fit using `Halo-FDCA`. *Left panels.* Compact source-subtracted image used for modelling the halo (and flux density measurements). *Right panels.* Residual image after subtraction of the model. The model is shown as black contours in both panels (solid: $[1, 2, 4, 8, 16, 32] \times \sigma_{rms}$, dashed: $0.5\,\sigma_{rms}$). The left panel colourscales are linear between $[-1, 10] \times \sigma_{rms}$ and the right panel colourscales are linear between $[-5, 5] \times \sigma_{rms}$. Note the surface brightness units are in μJy arcsec^{-2} for consistency with the literature.

4.4.4 PSZ2 G110.28–87.48

Figure A1(ix). We report the detection of a radio halo in PSZ2 G110.28–87.48. The radio halo is co-located with the X-ray emission, and we note there is a ≈ 2.4 arcmin offset between the *Planck*-SZ detection and the X-ray centroid.

4.4.5 PSZ2 G149.63–84.19 (Abell 133)

Figure A1(x). A radio phoenix was reported by Slee&Reynolds (1984) and Slee et al. (2001) in this cluster, and is well-detected in the ASKAP data. While considered a 'phoenix', in our classification scheme we do not distinguish between small-scale AGN-related diffuse emission and label the emission as 'uncertain/unclassified diffuse emission'. The second component south of the cluster centre is also detected with the ASKAP data. This component has previously been seen with the GMRT (Randall et al., 2010), the MWA (Duchesne et al., 2021c), and MeerKAT (Knowles et al., 2022) though it is unclear if this component was the lobe of a (possible background) radio galaxy or a diffuse radio source associated with the ICM. A wideband spectral study is required to confirm the nature of southern source, and the cluster and source will be discussed further in upcoming work focused on detection of giant radio galaxies (Koribalski et al., in prep) though we leave the classification of both the northern and southern sources as 'U' in this work.

4.4.6 PSZ2 G17298–53.55 (Abell 370)

Figure A1(xiv). The Frontier Fields cluster Abell 370 was observed with the VLA and GMRT by Xie et al. (2020) and was reported to host a candidate radio halo. Subsequent observations by Knowles et al. (2022) with MeerKAT confirm the detection of the radio halo and the ASKAP data presented here also detect the radio halo at low significance.

4.4.7 PSZ2 G17569–85.98 (Abell 141)

Figure A1(xvi). This is a pre-merging system (Caglar, 2018) with a radio halo reported by Duchesne et al. (2021c,b). The ASKAP data in this work have a marginally lower noise than in Duchesne et al. (2021b) owing to a new observation with the cluster closer to the PAF beam centre. This combined with better beam models, and a slightly different integration region, provides perhaps a more accurate (if less precise) flux density measurement (23 ± 8 mJy cf. 13.7 ± 1.9 mJy reported by Duchesne et al. 2021b).

4.4.8 PSZ2 G219.88+22.83 (Abell 664)

Figure A1(xviii). We report a candidate relic ≈ 2.5 Mpc to the NW of the cluster center. The candidate relic has no obvious AGN/host, and there is no high-resolution X-ray data that covers the location of the candidate relic. Artefacts from an off-axis bright source pass through the cluster centre, limiting any detection of a radio halo.

4.4.9 PSZ2 G223.47+26.85 (MACS J0845.4+0327)

Figure A1(xx). We report the detection of a radio halo, which is co-located with the X-ray emission detected by *XMM*-Newton.

4.4.10 PSZ2 G225.48+29.41 (Abell 732)

Figure A1(xxi). We report the detection of a radio halo in this cluster. The emission is partially confused with nearby extended sources. Even after subtraction of emission < 250 kpc, the full extent of the halo is difficult to determine. *Chandra* data reveal a disturbed morphology for the cluster. Extended emission is also visible to the north of the cluster (beyond 1 Mpc), though is likely an unrelated pair of radio sources, both with clear optical hosts.

4.4.11 PSZ2 G22759+22.98 (MaxBCG J129.82432–01.69949)

Figure A1(xxii). We report the detection of two candidate relics towards the NW and SE clearly visible in the compact-source subtracted maps and at low resolution. A brighter extended source SW of the cluster centre is prominent in the source-subtracted images and is a radio galaxy but also has diffuse emission extending towards the W. The radio galaxy, which may be a wide-angle tailed radio galaxy (WAT) in projection, has an optical ID, (SDSS J083917.83−014158.1), considered the BCG position in the maxBCG cluster catalogue (Koester et al., 2007). This would suggest an offset of ≈ 2.5 arcmin from the SZ coordinates and the BCG. The nature of the diffuse extension of this radio galaxy is unclear. No high-resolution X-ray data is available for the cluster.

4.4.12 PSZ2 G227.89+36.58

Figure A1(xxiii). The cluster hosts a complex collection of extended emission, including active radio galaxies. The subtraction of < 250 kpc sources leaves significant emission in and around the cluster, and we consider the residual emission to be candidate radio halo. Sensitive and high-resolution follow-up

observations by, e.g. MeerKAT would be required to confirm this source as a radio halo.

4.4.13 PSZ2 G228.38+38.58

Figure A1(xxiv). There is unclassified < 300 kpc emission ≈ 1.6 arcmin to the NE of the reported SZ cluster coordinates. The location of the diffuse emission is the centroid of cluster WHL J093439.0+054144 (Wen et al., 2009) at $z \approx 0.54$ and is likely the same system. Given the location of the small diffuse source at the centre of optical density for this system, this may be a mini-halo. Follow-up high-resolution X-ray observations would be required to confirm this.

4.4.14 PSZ2 G228.50+34.95

Figure A1(xxv). While the cluster has a a significant number of radio sources projected onto it, we are able to detect a residual extended component after subtraction of compact sources. This extended radio component coincides with the X-ray emission centroid, and we consider this a candidate radio halo.

4.4.15 PSZ2 G231.79+31.48 (Abell 776)

Figure A1(xxvii). We report the detection of a radio halo and radio relic. The radio halo is located co-spatial with the X-ray emission and the radio relic lies towards the edge of the X-ray emission region to the W. As the relic is embedded in the western portion of the halo (see Figure A1(xxvii)), we subtract the relic's integrated flux density from the flux density measurement of the radio halo, though the full extent of the halo towards the west is unclear.

4.4.16 PSZ2 G232.84+38.13 (Abell 847)

Figure A1(xxviii). The cluster hosts an extended radio source with uncertain classification. The source has no obvious optical host and may be a relic or fossil/phoenix. Given the distance from the cluster centre, we consider it a candidate relic. The 16 cluster members with spectroscopic redshifts from the SDSS have a velocity dispersion of ≈ 740 km s^{-1}. There is also diffuse emission near the cluster centre ≈ 15 arcsec south of the BCG (i.e. separated by one PSF width). The small angular scale (230 kpc) of the emission and its elongated morphology are not suggestive of a radio halo or mini-halo source. We consider this unclassified diffuse emission, and for both diffuse sources in the cluster X-ray observations would help in further clarification of the their nature.

4.4.17 PSZ2 G233.68+36.14

Figure A1(xxix). We report the detection of a radio halo and two radio relics to the N and SE of the radio halo emission. While there is no X-ray data available to confirm the cluster dynamics, the nature of the radio emission is clear from the morphology alone in this case.

4.4.18 PSZ2 G236.92–26.65 (Abell 3364)

Figure A1(xxx). This relaxed cluster hosts diffuse emission at its centre that not only coincides with the X-ray peak but also features a compact radio source near its centre, consistent with radio mini-halos. However, a second diffuse source with the same morphology as the first is located directly towards the west of the cluster separated by ≈ 4 arcmin. A radio source associated with the optical galaxy DES J054726.18−315210.8 (with a photometric redshift of 0.28) is located equidistant between the two diffuse sources and is also extended E-W in the direction of the two diffuse sources. We suggest DES J054726.18−315210.8 hosts a background radio galaxy with the diffuse sources the lobes and the E-W extension jets.

4.4.19 PSZ2 G239.27–26.01 (MACS J0553.4–3342)

Figure A1(xxxi). The cluster hosts a previously detected radio halo (Bonafede et al., 2012) and previous ASKAP data reported by Wilber et al. (2020) show the radio halo as well. The ASKAP data here are the same observations used by Wilber et al. (2020), though our self-calibration process and compact source subtraction is different. We end up with a marginally better detection with compact sources removed, though our directional self-calibration process in this case has similar results to the full direction-dependent calibration used by Wilber et al. (2020). We report a higher flux density, though note Wilber et al. (2020) use a different integration region within 3$\sigma_{\rm rms}$ contours. No further diffuse emission is found.

4.4.20 PSZ2 G241.79–24.01 (Abell 3378)

Figure A1(xxxii). The cluster hosts a bright compact source at the centre (PKS 0604−352, associated with the BCG), though artefacts are reduced during the directional self-calibration process (see Section 3.1.1). The cluster is relaxed and features at least one diffuse component off-centre. A second component coincident with the central bright source is seen after compact source subtraction, though will need further confirmation with higher dynamic range imaging due to the possibility of residual artefacts left over after compact source subtraction.

4.4.21 PSZ2 G260.80+06.71

Figure A1(xxxv). We consider an elongated source near the edge of the cluster (assuming $z = 0.2$) a candidate radio relic. There is also residual diffuse emission at the cluster centre after compact source subtraction that resembles a radio halo, though it is unclear if this is residual emission from partial subtraction or is a double radio source at the cluster centre. We note that the cluster is at a low Galactic latitude, has not been confirmed by other surveys/at other wavelengths, and has no reported redshift, and the candidate sources may be therefore Galactic in origin.

4.4.22 PSZ2 G262.36–25.15 (Abell 3391)

Figure A1(xxxvi). A small (≈ 160 kpc) diffuse source is located towards the SE of the cluster centre, though it is unclear what the source is. Brüggen et al. (2021) show the same ASKAP data but with full direction-dependent calibration. They do not comment on this source as it lies within the region of large-scale artefacts from the bright radio galaxy at the centre of the cluster. However, after compact source subtraction and image-based filtering the source remains and we suggest it is a real diffuse component.

4.4.23 PSZ2 G263.14–23.41 (Abell S592)

Figure A1(xxxvii). This cluster hosts a radio halo, originally detected by Wilber et al. (2020) with the same ASKAP observations. As with PSZ2 G239.27−26.01, differences in the integration region and thresholds used yield differences in the flux density measurements. We note as well that this dataset has one of the poorer PAF beam models, with ≈ 26% uncertainty from the primary beam modelling alone.

4.4.24 PSZ2 G263.19–25.19 (Abell 3395)

Figure A1(xxxviii). Brüggen et al. (2021) report the detection of a complex extended radio source with diffuse components (their sources 'S2' and 'S3'). The source comprises both active radio sources as well as diffuse components which may be revived fossil plasma.

4.4.25 PSZ2 G26368–22.55 (Abell 3404)

Figure A1(xxxix). This radio halo was detected by Duchesne et al. (2021b) with the same ASKAP data. We report a higher flux density in this work, again due to either integration of the full polygon region or model fitting, though note that due to the density of sources in the cluster that are subtracted, the associated uncertainty in the measurement is 50%. We note that while Planck Collaboration et al. (2016a) report $z = 0.1644$ for this cluster, only four galaxies in the vicinity of the cluster have reported redshifts: two at $z \approx 0.164$ and two at $z \approx 0.338$ (Jones et al., 2009; Guzzo et al., 2009; Bocquet et al., 2019), suggesting a possible second cluster along the line of sight.

4.4.26 PSZ2 G272.08–40.16 (Abell 3266)

Figure A1(xliii). A radio relic, fossil source, and other ambiguous diffuse emission were detected at multiple frequencies (Murphy, 1999; Duchesne et al., 2022; Riseley et al., 2022b) and a radio halo was also detected in these ASKAP observations by Riseley et al. (2022b). The compact source-subtraction and directional self-calibration procedure have revealed more of the radio halo. Some residual artefacts around a bright WAT source limit the full detection of the halo to the SW. The model flux density of the radio halo is larger than that reported by Riseley et al. (2022b), though this is a combination of general increase in flux density from integrating a model and a much larger region over which we detect the halo. From the upper limit at 216-MHz reported by Duchesne et al. (2022), we place a limit on the spectral index of $\alpha_{216}^{944} \gtrsim -1.4$.

4.4.27 PSZ2 G286.28–38.36

Figure A1(xlix). We report the detection of a radio halo in this cluster. The halo is almost perpendicular to the elongation of the X-ray emission, though it is unclear how much of the E-W extension in the radio is associated with the halo. Previously the cluster was observed with the ATCA[u] but no diffuse emission was detected (Martinez Aviles et al., 2018). An upper limit to the radio halo luminosity of $P_{1.4\,GHz} \lesssim 1.55 \times 10^{24}$ W Hz^{-1} (assuming $\alpha = -1.3$) was reported by Aviles et al. (2018). Extrapolating from our measurement and assuming the same spectral index, we find $P_{1.4\,GHz} = (4 \pm 1) \times 10^{24}$ W Hz^{-1}, inconsistent with the upper limit, requiring $-1.5 \lesssim \alpha_{888}^{1400} \lesssim -2.6$ to be consistent, suggesting this may be an ultra-steep spectrum halo (e.g. Brunetti et al., 2008).

4.4.28 PSZ2 G286.75–37.35

Figure A1(l). We report the detection of a radio halo in this cluster. While there is no high-resolution X-ray data available, it is clear from the location and morphology of the radio emission that it represents a radio halo.

[u] Australia Telescope Compact Array.

4.4.29 PSZ2 G311.98+30.71 (Abell 3558)

Figure A1(li). The cluster is part of the Shapley supercluster and Venturi et al. (2022) detected a radio halo with ASKAP. The ASKAP dataset in this work is a different (but similar) observation, and the radio halo is detected again in this work.

4.4.30 PSZ2 G313.33+30.29 (Abell 3562)

Figure A1(lii). Also in the Shapley supercluster, The ASKAP data detect the well-known radio halo (Venturi et al., 2003) along with the recently detected bridge between the cluster and the nearby group SC 1329−313 (Venturi et al., 2022).

4.4.31 PSZ2 G332.23–46.37 (Abell 3827)

Figure A1(lvi). We report the detection of a radio halo in this cluster. The halo aligns well with X-ray emission detected by *XMM*-Newton, though has a concentration parameter, $c \approx 0.23$, (Lovisari et al. 2017, with a similar value reported by Yuan et al. 2022: ≈ 0.21) Giant radio halos are typically found in clusters with $c \lesssim 0.2$ (Cassano et al., 2010, 2023). The largest linear size within $2\sigma_{rms}$ contours is 620 kpc and with a point source at the centre of the emission in this comparatively relaxed cluster the halo may be considered a mini-halo. Bernardi et al. (2016) show observations of the cluster with KAT-7, though with the low angular resolution of the KAT-7 data they could not separate any diffuse emission from the compact sources at the cluster centre.

4.4.32 PSZ2 G333.89–43.60 (SPT-CL J2138–6007)

Figure A1(lviii). We report the detection of a radio halo in this cluster. The residual diffuse emission in the cluster centre after subtraction of compact sources is co-spatial with the X-ray emission detected by *XMM*-Newton.

4.4.33 PSZ2 G33558–46.44 (Abell 3822)

Figure A1(lix). We report the detection of a radio halo and radio relic. The dynamical state of the cluster from X-ray observations is considered 'Mixed' by Lovisari et al. (2017), with concentration parameter, of ≈ 0.11. Yuan et al. (2022) report a slightly higher concentration parameter (≈ 0.17), consistent with most halo-hosting clusters.

4.4.34 PSZ2 G341.19–36.12 (Abell 3685)

Figure A1(lxiv). Duchesne et al. (2021a) report the detection of double relics with these ASKAP observations. The re-imaged data here do not reveal any new diffuse emission in this cluster, and flux density measurements are reasonably consistent with those reported by Duchesne et al. (2021a) for the two relics.

4.4.35 PSZ2 G342.33–34.93 (SPT-CL J2023–5535)

Figure A1(lxvi). HyeongHan et al. (2020) reported the detection of a radio halo and relic. The same observations are used here, and with our tapered and compact-source subtracted images we detect a marginally larger extent of the radio halo. Flux density measurements are consistent with HyeongHan et al. (2020), though we note the integrated model flux density for the radio halo is ≈ 1.6 times the direct integration from the map. A secondary relic is also detected. This second relic is not reported by HyeongHan et al. (2020), and though it is visible in the deeper MeerKAT image from the MGCLS it is also not reported by Knowles et al. (2022).

4.4.36 PSZ2 G342.62–39.60 (Abell 3718)

Figure A1(lxvii). Loi et al. (2023) reported the detection of an unclassified extended source at the cluster centre using the same ASKAP observations. The source has small-scale features that are subtracted during the (u, v)-filtering and is also blended with unassociated point sources that make the integrated flux density measurement unreliable, therefore this measurement (and radio power) is not included in Table 3. The source is elongated, and its nature remains unclear.

4.4.37 PSZ2 G346.86–45.38 (Abell 3771)

Figure A1(lxx). We report the detection of a radio halo. The cluster was part of the ATCA[v] REXCESS[w] Diffuse Emission Survey (ARDES; Shakouri et al., 2016), though no halo was detected in the ATCA data. The ATCA data detected the brighter head-tail radio galaxy in the cluster, offset from the radio halo by ≈ 5 arcmin (≈ 450 kpc).

4.4.38 PSZ2 G34758–35.35 (Abell S871)

Figure A1(lxxi). We report a candidate halo. The candidate halo is located between two extended radio sources (and related to AGN) which are not fully subtracted during the (u, v)-based compact source subtraction, but this is mitigated during the model fitting where the residuals from those sources are masked. No X-ray data are available from *Chandra* or *XMM*-Newton. The candidate halo is offset from the PSZ2-reported position by ≈ 2 arcmin (≈ 430 kpc), but is centered on the position reported in the Abell catalogue (Abell et al., 1989). Abell et al. (1989) also note that the distribution of optical galaxies is bimodal (following the aforementioned radio galaxies) and the the diffuse radio source sits somewhat between these optical concentrations as in the case of PSZ2 G175.690−85.98 (Abell 141, Section 4.4.7; Duchesne et al. 2021b).

5. Discussion

5.1 The number of diffuse cluster sources

Some type of diffuse radio emission, i.e., not associated with active radio galaxies, is found in 37 (52%) of the 71 clusters in our sample (including candidate sources). Figure 11 shows the numbers of each source type – halo (H), candidate halo (cH), relic (R), candidate relic (cR), unclassified diffuse emission (U), bridge, and clusters with no diffuse sources (NA). We include the class 'bridge' for a single case of an unambiguous and previously detected bridge of emission between a cluster and group (PSZ2 G313.33+30.29 and SC 1329−313; Venturi et al. 2022). For halos and relics, the total numbers are 21 halos (30% of clusters, with six candidates) and 11 relics (10% of clusters, with an additional five candidates). These sources are found in 12 clusters; 32% of the PSZ2 subsample in this work are found to host halos and/or relics.

In the current observation plan for the ASKAP main surveys, EMU will cover the full sky south of declination $-7°$ with additional coverage between $-7°$ and $+7°$ in declination for certain RA ranges. In Figure 12 we show the planned full EMU sky coverage and highlight the 858 PSZ2 clusters that lie within 0.75 degrees of a PAF beam in this region. Extrapolating the detection fractions

[v] Australia Telescope Compact Array.
[w] Representative *XMM*-Newton Cluster Structure Survey; Böhringer et al. (2007).
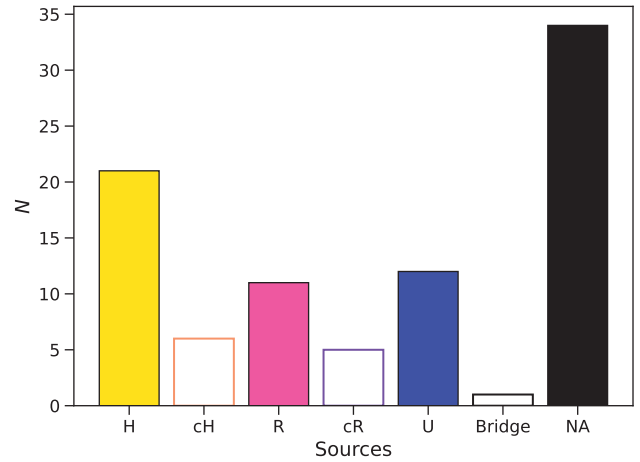
Figure 11. Counts of the halos (H), candidate halos (cH), relics (R), candidate relics (cR), unclassified sources (U), bridge, and clusters without diffuse emission (NA) in the ASKAP data for all 71 clusters in the sample.
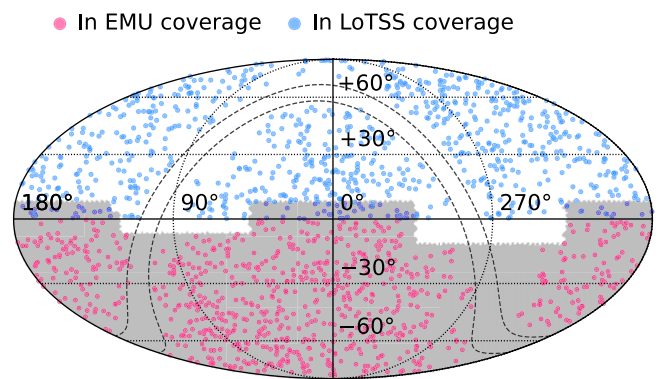
Figure 12. The distribution of PSZ2 clusters across the sky, coloured by their eventual presence in the EMU survey (pink) and LoTSS (blue). Clusters appearing in overlap regions are coloured purple. The expected full EMU survey coverage is coloured grey.

for our PSZ2 subsample, we can expect up to 254^{+88}_{-16} and 85^{+57}_{-9} PSZ2 clusters hosting halos and relics, respectively, in the EMU survey, assuming the number of candidates provides an estimate to the upper limit in the number.

Cassano et al. (2012) use the original EMU survey description (at 1.4 GHz) to predict up to ≈ 250 radio halos detected in clusters with redshifts between $0 < z \leq 0.6$ within the planned EMU coverage shown in Figure 2. This includes the assumption that a significant fraction of giant radio halos are formed through non-turbulent processes (i.e. emission via secondary electrons generated by collisions in the ICM). We note that while this number agrees with our prediction for the full EMU survey, we do not distinguish between giant radio halos and mini-halos, the latter of which is predominantly found in non-merging clusters. Conversely, the total number of halos expected in PSZ2 clusters is lower than the $\approx 1\,000$ radio halos expected below $z < 0.5$ reported by Nishiwaki & Asano (2022) from a comparison of theoretical models, though we note one halo in this work is detected in PSZ2 G110.28−87.48 ($z = 0.52$). Moreover, Nishiwaki & Asano (2022) consider EMU to cover the full sky up to declination $+30°$, and the PSZ2 catalogue itself does not contain all clusters. With these caveats in mind, we can consider the expected number of
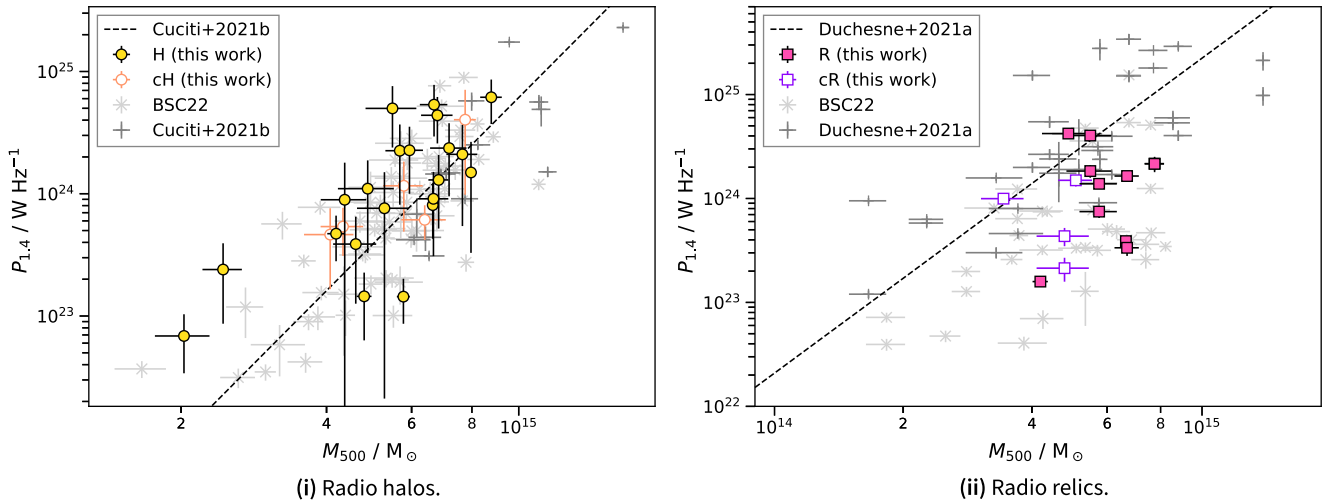
Figure 13. $P_{1.4\,\mathrm{GHz}}$–M_{500} scaling relation for radio halos ((i)) and radio relics ((ii)). We show radio halos and relics (and candidates) detected in this work, along with the halo and relic samples discovered in the LoTSS-DR2 data (at 144 MHz; Botteon et al., 2022a) and the samples curated by Cuciti et al. (2021a,b, and see references therein) for radio halos and Duchesne et al. (2021a, and see references therein) for radio relics, largely detected at frequencies above $\approx$ 1 GHz. Flux densities and luminosities have been scaled to 1.4 GHz assuming $\alpha = -1.3$ for radio halos and $\alpha = -1.2$ for relics as described in the text. Best-fit $P_{1.4}$–M_{500} correlations from Cuciti et al. (2021b) and Duchesne et al. (2021a) are shown for halos and relics, respectively.

halos extrapolated from this work in reasonable agreement with theoretical predictions.

The full LoTSS-DR2 and EMU surveys are expected to have similar total sky coverage – we show the distribution of PSZ2 cluster across the full EMU and LoTSS regions in Figure 12. Assuming the median LoTSS-DR2 noise of 83 μJy PSF^{-1} at 6 arcsec (Shimwell et al., 2022) and a median 30 μJy PSF^{-1} at 15 arcsec for the EMU survey, the higher-frequency observations at 943 MHz are less sensitive to the steep-spectrum diffuse cluster emission and we would not expect to detect as many sources as LoTSS[x]. Despite this, the percentage of clusters found to host a radio halo and/or relic is the same as the result from the LoTSS-DR2 PSZ2 survey. BSC22 find (30 ± 11)% and (10 ± 6)% of PSZ2 clusters to host halos and relics, respectively, and suggest the full LoTSS will uncover 251 ± 92 and 83 ± 50 PSZ2 clusters hosting halos and relics, respectively. We caution that the fraction of clusters found to host diffuse emission in this work is likely higher at low redshift than what can be expected for the full survey. Three of the archival ASKAP observations targeted nearby clusters: PSZ2 G272.08−40.16 (Abell 3266 in SB10636; see Riseley et al. 2022b), the cluster pair PSZ2 G262.36−25.15 and PSZ2 G263.19−25.19 (Abell 3391 and Abell 3395 in SB8275; see Brüggen et al. 2021), and PSZ2 G311.98+30.71 and PSZ2 G313.33+30.29 (Abell 3558 and Abell 3562 in SB34120; Venturi et al. 2022). These low-redshift clusters were targeted specifically for known or expected diffuse cluster emission.

5.2 The discovery space of the EMU survey

The radio power of both halos and relics have been observed to scale with host cluster mass (e.g. Cassano et al., 2013; de Gasperin et al., 2014; Cuciti et al., 2021b; Duchesne et al., 2021a,b) and other related cluster and source morphological properties (e.g. X-ray luminosity and temperature Liang et al. 2000; source size Bonafede et al. 2009). Traditionally, scaling relations have been

explored at 1.4 GHz, though with the advent of LOFAR and the MWA they are now being explored at 150 MHz as well (van Weeren et al., 2021; Duchesne et al., 2021b). In addition to the low-frequency exploration, recent results from the LoTSS-DR2 data release and the MWA have revealed radio halos and relics in clusters of lower mass than previously seen (Dwarakanath et al., 2018; Botteon et al., 2019; van Weeren et al., 2021; Botteon et al., 2021, 2022a; Duchesne et al., 2021c,d). Detection of diffuse emission in clusters with masses less than $\approx 5 \times 10^{14}$ M$_{\odot}$ has been required to investigate the scaling relations in the low mass regime (and presumably with low turbulent energy for the generation of the radio halos). Recent statistical works with the LoTSS-DR2 cluster sample (Cassano et al., 2023; Cuciti et al., 2023; Jones et al., 2023) have begun to probe this low-mass regime, and find that the scaling relations continue into this previously unexplored space. The lower luminosity halos ($< 10^{24}$ W Hz^{-1}) are comparable to the stacked results reported in Brown et al. (2011), although they could not filter out any diffuse emission associated with radio galaxies that was below the individual cluster detection limits.

The cluster sample in this work is not statistically complete and we do not provide upper limits to non-detections. We do not update the scaling relations but we do show our detections of halos and relics with the existing power-mass ($P_{1.4}$–M_{500}) relations in Figure 13 for halos [13(i)] and relics [13(ii)]. For comparison, the power calculations for sources detected in this work are scaled to 1.4 GHz assuming $\alpha = -1.3 \pm 0.2$ for radio halos and $\alpha = -1.2 \pm 0.2$ for relics (Duchesne et al., 2021d). Similarly, the LoTSS-DR2 sources are shown and scaled to 1.4 GHz assuming the same mean spectral indices. We also show the best-fit $P_{1.4}$–M_{500} relations from Cuciti et al. (2021b) and Duchesne et al. (2021a) for radio halos and relics, respectively. Due to the sensitivity of the ASKAP sample in this work, we are pushing into the low-mass regime for both radio halos and radio relics, and in the case of halos, we find six halos (and two candidate halos) in clusters with masses of $< 5 \times 10^{14}$ M$_{\odot}$. Four of these low-mass clusters are nearby ($z < 0.09$) with the lowest mass cluster Abell 3771 (see Section 4.4.37) with a redshift of 0.0796. The candidate radio halos

---

[x]Unless sources have $\alpha \gtrsim -0.6$, which is not the case for diffuse cluster sources.
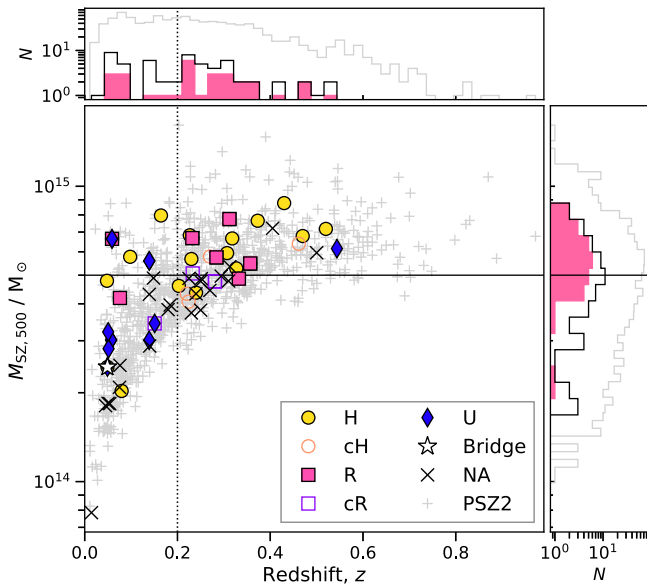
Figure 14. The mass-redshift distribution of the PSZ2 catalogue (with redshifts) as in Figure 1 but with clusters and their sources from this survey marked as appropriate. Clusters in our sample without detected diffuse emission are labelled 'NA'. The dashed and dotted black lines indicate $z = 0.09$ and $z = 0.2$, respectively. The histograms show the distributions of the combined halo and relic counts (pink, including candidates) across the redshift and mass range along with the full PSZ2 sample (grey) and cluster searched in this work (black, with redshifts).

Figure 15. The peak surface brightness as a function of integrated flux density for the diffuse sources.

in low-mass clusters, conversely, are all hosted by higher-redshift clusters. For clusters with relics, only two have masses $< 5 \times 10^{14}$ $M_\odot$ (with an additional two candidate relics in low-mass clusters). One system has a low redshift, and no double relic systems are detected in the low-mass clusters in these ASKAP data.

Figure 14 shows the distribution of PSZ2 clusters as a function of redshift as in Figure 1 with clusters and sources in this survey overlaid. We also show histograms of the redshift and mass distributions, highlighting the full PSZ2 catalogue (grey), the 71 clusters used in this work (black), and PSZ2 clusters with a radio halo and/or relic (pink). We are detecting diffuse emission over the majority of the mass and redshift range, though with a steady decrease in detections as mass is decreased. Considering the empirical scaling relations, we expect to see only low-power halos and relics in low-mass clusters. Low-power radio sources are naturally harder to detect. For halos in particular, this remains true even at low redshifts where their large size and low surface brightness limits detectability despite a large total flux density. Despite these limitations, the results from this survey with archival ASKAP data products yields promising prospects for the full EMU survey.

5.3 Detection and measurement of low-brightness, extended emission

Many of the lowest brightness extended features are only detectable at lower resolutions, after the confusing emission from more compact features are removed. Figure 15 shows the peak surface brightness as a function of integrated flux density for the diffuse radio sources reported in this work. We find radio halos down to a peak surface brightness of $\approx 0.2\,\mu$Jy arcsec^{-2} and relics down to $\approx 0.5\,\mu$Jy arcsec^{-2}. Radio halos are found with both lower peak surface brightness and lower average surface brightness (not shown here) than other diffuse sources.
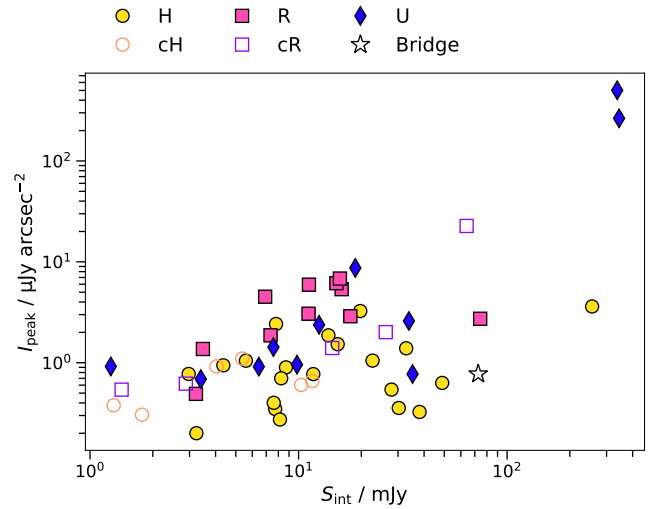
To help both detect and measure this low surface brightness emission, it is common to model and subtract embedded, unassociated (typically compact) sources in the (u, v) plane as done in this work (see Section 3.1.1). In the current era of large sky surveys and ever-increasing data volumes, this additional computationally expensive imaging step becomes prohibitive. This is exacerbated when filtering multiple angular scales. An alternative is removing compact sources or small-scale features in the image plane. Imaged-based angular scale filtering methods are being used on radio data to look at both large-scale features (e.g. Rudnick, 2002; Knowles et al., 2022; Riseley et al., 2022b; de Jong et al., 2022; Velović et al., 2023), and small-scale features (e.g. edges; Murgia et al., 2001; Ramatsoku et al., 2020; Botteon et al., 2023). EMU is making use of image-based filtering and for this work, as described in Section 3.1.4, we have produced equivalent filtered images for comparison with traditional (u, v)-plane filtering.

Upon inspection of the output maps, we find that the image-based filtering of both small and very large angular scales is useful in identifying diffuse sources while discarding artefacts from poor short baseline calibration and interference from the off-axis sources of large angular scales (including the Sun). For the full EMU survey, the image-based filtering is being done on all images, retaining scales between $3\,\theta_M \lesssim \theta_{scale} \lesssim 27\,\theta_M$. However, it is important to understand the limitations of this image-based approach, so we take advantage of the current analysis to make a comparison with image-based filtering.

First, the EMU default range of filter angular scales is not suitable for all clusters: for clusters with $z \lesssim 0.1$ the large-scale filter begins to remove sources of interest. An example of this is PSZ2 G272.08−40.16 (Abell 3266), which was found to host a ≈ 10-arcmin (≈ 700 kpc) radio halo via similarly filtered images (Riseley et al., 2022b). The radio halo is clearly detected in the pre-filtered data and the (u, v)-filtered data (after removing angular scales > 88 arcsec). In our re-imaged data, the halo is detected within $2\,\sigma_{rms}$ contours out to 25 arcmin (≈ 1.7 Mpc) which is $> 27\,\theta_M$ (≈ 7.5 arcmin) and is completely removed during image-based filtering with the default parameters. This is highlighted in the right panel of Figure 6(i).

In some situations, neither (u, v)- or image-based filtering can be used effectively, such as in the presence of bright point
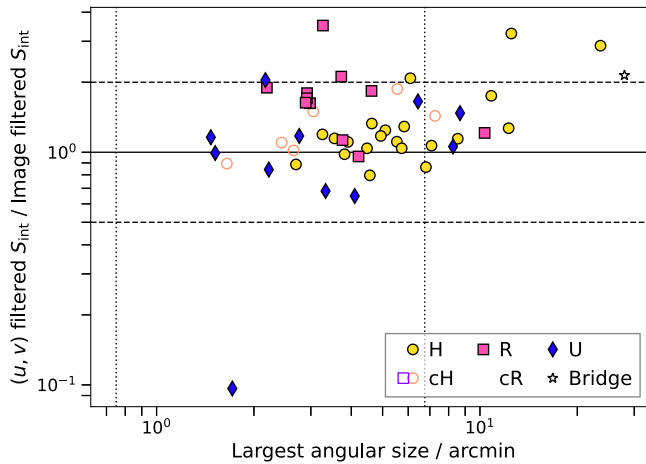
Figure 16. The ratio of integrated flux density measurements from the (u, v)-filtered and image-filtered maps as a function of largest angular scale of the source. The solid black line is drawn at 1, with the dashed lines indicating ratios of 0.5 and 2. The vertical dotted lines indicate 45 arcsec and 405 arcsec – approximately the image filtering scale, $3\,\theta_M$ and $27\,\theta_M$, respectively.

sources. Abell 3378, for example (Figure 6(ii)) hosts a bright point source at its centre. After application of image-based filtering, the artefacts accompanying bright sources result in regions of negative emission around the source. After (u, v) filtering and removal of the point source, some residual emission remains at the cluster centre but it is unclear whether this is also related to residual artefacts from the bright source. In this case, neither the image-based or (u, v)-based subtraction provide a clear image of the centre of the cluster.

We also investigate the utility of the image-filtered maps for measuring flux density. Rudnick (2002) showed that the flux remaining in the filtered maps is a function of the relative size of the feature and the filter scale. For the EMU survey, the filter is chosen to ensure that sources at $\approx \theta_M$ (i.e. compact sources) are removed completely from the diffuse emission maps. Figure 16 shows the ratio of measured flux densities in the (u, v)-filtered and image-filtered maps as a function of source size. We find that the image-filtered measurements are on average $\approx 70\%$ of the (u, v)-filtered flux density, though this is more extreme for relics (median $\approx 60\%$) than for halos (median $\approx 90\%$). This results from the removal of some small-scale fluctuations in the relic by the image-based filter. With the EMU survey filter, it is thus important to recognize that relics can be significantly underestimated, and sources with angular sizes $> 27\,\theta_M$ will be difficult to detect and measure reliably.

6. Future work

The full EMU survey commenced in November 2022 and is expected to take about five years, covering most of the southern sky (see Figure 12). So far ≈ 100 fields (out of ≈ 850) have been observed, validated, and made public in CASDA, and we expect observing efficiency and data flow to increase over the next year. Equatorial fields are observed in two 5-h sessions; after combination and subsequent mosaicking of all tiles this will result in a homogeneous radio continuum sky survey where no or very little re-processing should be required before applying the analysis methods developed here to search for diffuse, non-thermal radio emission in PSZ2 clusters. Of particular note is the utility of

the image-based filtering for searching for this emission in lieu of (u, v)-plane subtraction methods.

There are a number of avenues for future work involving diffuse emission in clusters with EMU. This includes the natural extension of the present work to the whole EMU survey. With the predicted numbers of sources, we should approach a statistically significant sample for which secondary correlations, e.g., with cluster morphology, can be examined. While the statistical results obtained at 150 MHz and at 1.4 GHz so far have not been substantially different (e.g. van Weeren et al., 2021), having two independent samples of cluster sources at 144 MHz (from the full LoTSS) and 943 MHz (from the full EMU survey) will allow a deep exploration of the scaling relations for halos and relics as a function of frequency. We will also be able to expand the cluster sample, including non-PZS2 cluster catalogues like the Abell catalogues (Abell et al., 1989, with 3 511 clusters in the planned EMU coverage), X-ray cluster samples like the Meta-Catalogue of X-ray detected Clusters of galaxies (MCXC; Piffaretti et al., 2011, 796 in EMU) or recent (and upcoming) cluster catalogues from the eROSITA[y], including the Final Equatorial Depths Survey (eFEDS; Liu et al., 2022, with all 542 clusters in EMU) and the All-Sky Survey (eRASS:1; Bulbul et al., in prep) and other SZ-selected cluster catalogues from the South Pole Telescope (e.g. Bleem et al., 2020, with 677 in EMU) and the Atacama Cosmology Telescope (e.g. Hilton et al., 2021, with 2 826 in EMU). While many of these catalogues have significant overlap, the number of non-PSZ2 clusters will also provide an additional sample to search, with similar LoTSS searches showing promising results (Hoang et al., 2022).

EMU is well-suited for exploration of radio galaxies in clusters. Recently, Böckmann et al. (2023) combined the EMU Pilot Survey (Norris et al., 2021) and eRASS:1 cluster catalogue, analysing the interaction between the X-ray–emitting ICM and the central radio galaxy/AGN. This work, too, is expected to be expanded to EMU images that overlap with the eRASS:1 coverage. Within the context of searching for low-surface brightness radio sources, work is being done to employ methods that do not rely on individual visual inspection alone. Gupta et al. (2022) used unsupervised machine learning to highlight sources with peculiar morphologies, finding a handful of diffuse cluster sources in archival ASKAP data. Other methods include the combination of complexity metrics followed by crowd-sourced inspection of classified sources (Segal et al., 2023). Such techniques may be employed to search for diffuse cluster emission, which will be particularly useful when considering expanded cluster samples. EMU will provide an important first step towards samples of diffuse radio sources in Southern Sky, providing the groundwork for future high-sensitivity, and high-resolution surveys with the SKA.

7. Summary

In this work we have performed a survey of diffuse radio emission in galaxy clusters using archival ASKAP data. The purpose of this work is to assess the prospects of the full EMU survey with respect to the numbers of radio halos and relics that we should expect to find once the survey is completed, and to inform on the type of statistical work that will be possible.

We follow BSC22 and investigate clusters from the PSZ2 catalogue, identifying 71 PSZ2 clusters within deep archival datasets around ≈ 1 GHz. We re-calibrate and re-image the archival data to both improve consistency in the imaging quality

---

[y]extended ROentgen Survey with an Imaging Telescope Array; Predehl et al. (2021).

and to generate images suitable for both finding diffuse cluster emission and characterising it. This includes producing low-resolution, tapered images and images with compact sources filtered out via (u, v)-plane subtraction and image-based angular scale filtering. We make a brief comparison of these filtering methods, highlighting the utility of the (less resource-intensive) image-based filtering which is being used to generate additional data products for the full EMU survey. The filtering methods all perform well at detecting diffuse sources and removing the compact source contributions, though there is some discrepancy between measured flux densities that arises due to differences in angular scales being filtered.

In this survey we see a number of previously detected diffuse cluster sources, including those detected in ASKAP data for the first time. In total, we report the detection of 21 radio halos (with an additional six candidates), of which 12 (and all candidates) are reported here for the first time. We note that five of the remaining halos have been previously reported using the same or similar ASKAP observations. We also detect 11 relics across seven clusters (with five additional candidates), six (and all candidates) reported here for the first time, and four previously detected in the same ASKAP data. In addition to the radio halo and relic detections, we identify 12 unclassified diffuse sources, including the previously detected phoenix in Abell 133. We also confirm the radio bridge connecting to Abell 3562 and a nearby group. Based on this survey of archival data, we estimate we may detect halos in 254^{+88}_{-16} PSZ2 clusters and relics in 85^{+57}_{-9} PSZ2 clusters in the full EMU survey. We find radio halos and relics down to peak surface brightnesses of $\approx 0.2\ \mu$Jy arcsec^{-2} and $\approx 0.5\ \mu$Jy arcsec^{-2}, respectively. We also find that we are detecting diffuse sources in low mass ($< 5 \times 10^{14}\ M_\odot$) clusters, highlighting overall exciting prospects for the full EMU survey in complementing Northern Hemisphere clusters surveys with LOFAR.

Data availability. Observatory-processed ASKAP data products are available through CASDA: https://data.csiro.au/domain/casdaObservation, listed under the SBIDs in Table 1. X-ray observations can be accessed through https://cda.harvard.edu/chaser and https://nxsa.esac.esa.int/nxsa-web for *Chandra* and *XMM*-Newton data products, respectively. Optical data products can be accessed through https://des.ncsa.illinois.edu/desaccess, https://ps1images.stsci.edu/cgi-bin/ps1cutouts, and http://archive.stsci.edu/cgi-bin/dss_form for DES, PS1, and DSS2, respectively. The specific images produced for this work are available through the PASA Datastore (https://data-portal.hpc.swin.edu.au/institute/pasa).

References

Abazajian, K. N., et al. 2009, ApJS, 182, 543

Abbott, T. M. C., et al. 2018, ApJS, 239, 18

Abbott, T. M. C., et al. 2021, ApJS, 255, 20

Abell, G. O., Corwin, Jr. H. G., & Olowin, R. P. 1989, ApJS, 70, 1

Aguado-Barahona, A., Barrena, R., Streblyanska, A., Ferragamo, A., Rubiño-Martn, J. A., Tramonte, D., & Lietzen, H. 2019, A&A, 631, A148

Akamatsu, H., et al. 2015, A&A, 582, A87

Allison, J. R., et al. 2022, PASA, 39, e010

Arras, P., Reinecke, M., Westermann, R., & Enßin, T. A. 2021, A&A, 646, A58

Bagchi, J., Durret, F., Neto, G. B. L., & Paul, S. 2006, Science, 314, 791

Bernardi, G., et al. 2016, MNRAS, 456, 1259

Biava, N., et al. 2021, MNRAS, 508, 3995

Bleem, L. E., et al. 2020, ApJS, 247, 25

Boch, T., & Fernique, P. 2014, in Manset N., Forshay P., eds, Astronomical Society of the Pacific Conference Series Vol. 485, Astronomical Data Analysis Software and Systems XXIII. p. 277

Böckmann, K., et al. 2023, A&A, 677, A188

Bocquet, S., et al. 2019, ApJ, 878, 55

Böhringer, H., et al. 2007, A&A, 469, 363

Bonafede, A., Giovannini, G., Feretti, L., Govoni, F., & Murgia, M. 2009, A&A, 494, 429

Bonafede, A., et al. 2012, MNRAS, 426, 40

Bonnarel, F., et al. 2000, A&AS, 143, 33

Botteon, A., et al. 2019, A&A, 630, A77

Botteon, A., et al. 2021, ApJ, 914, L29

Botteon, A., et al. 2022a, A&A, 660, A78

Botteon, A., et al. 2022b, Science Advances, 8, eabq7623

Botteon, A., Markevitch, M., van Weeren, R. J., Brunetti, G., & Shimwell, T. W. 2023, A&A, 674, A53

Boxelaar, J. M., van Weeren, R. J., & Botteon, A., 2021, Astronomy and Computing, 35, 100464

Briggs, D. S. 1995, PhD thesis, The New Mexico Institute of Mining and Technology, Socorro, New Mexico

Brown, S., Emerick, A., Rudnick, L., & Brunetti, G. 2011, ApJ, 740, L28

Brüggen, M., Bykov, A., Ryu, D., & Röttgering, H. 2012, Space Sci. Rev., 166, 187

Brüggen, M., et al. 2021, A&A, 647, A3

Brunetti, G., & Jones T. W. 2014, Int. J. Modern Phys. D, 23, 1430007

Brunetti, G., Setti, G., Feretti, L., & Giovannini, G. 2001, MNRAS, 320, 365

Brunetti, G., et al. 2008, Nature, 455, 944

Bruno, L., et al. 2023a, A&A, 672, A41

Bruno, L., et al. 2023b, A&A, 678, A133

CASA Team, et al. 2022, PASP, 134, 114501

Caglar, T. 2018, MNRAS, 475, 2870

Cassano, R., Brunetti, G., Setti, G., Govoni, F., & Dolag, K. 2007, MNRAS, 378, 1565

Cassano, R., Ettori, S., Giacintucci, S., Brunetti, G., Markevitch, M., Venturi, T., & Gitti, M. 2010, ApJ, 721, L82

Cassano, R., Brunetti, G., Norris, R. P., Röttgering, H. J. A., Johnston-Hollitt, M., & Trasatti, M. 2012, A&A, 548, A100

Cassano, R., et al. 2013, ApJ, 777, 141

Cassano, R., et al. 2023, A&A, 672, A43

Chambers, K. C., et al. 2016, preprint, (arXiv 1612.05560)

Chapman, J. M., Dempsey, J., Miller, D., Heywood, I., Pritchard, J., Sangster, E., Whiting, M., & Dart, M. 2017, in Lorente N. P. F., Shortridge K., Wayth R., eds, Astronomical Society of the Pacific Conference Series Vol. 512, Astronomical Data Analysis Software and Systems XXV. p. 73

Clarke, T. E., Kronberg, P. P., & Böhringer, H. 2001, ApJ, 547, L111

Cuciti, V., et al. 2021a, A&A, 647, A50

Cuciti, V., et al. 2021b, A&A, 647, A51

Cuciti, V., et al. 2022, Nature, 609, 911

Cuciti, V., et al. 2023, A&A, 680, A30

De Filippis, E., Bautz, M. W., Sereno, M., & Garmire, G. P. 2004, ApJ, 611, 164

Di Gennaro, G., et al. 2019, ApJ, 873, 64

Di Gennaro, G., et al. 2021, A&A, 654, A166

Dickey, J. M., et al. 2013, PASA, 30, e003

Duchesne, S. W., Johnston-Hollitt, M., Zhu, Z., Wayth, R. B., & Line, J. L. B. 2020, PASA, 37, e037

Duchesne, S. W., Johnston-Hollitt, M., Bartalucci, I., Hodgson, T., & Pratt, G. W. 2021a, PASA, 38, e005

Duchesne, S. W., Johnston-Hollitt, M., & Wilber, A. G. 2021b, PASA, 38, e031

Duchesne, S. W., Johnston-Hollitt, M., Offringa, A. R., Pratt, G. W., Zheng, Q., & Dehghan, S. 2021c, PASA, 38, e010

Duchesne, S. W., Johnston-Hollitt, M., & Bartalucci, I. 2021d, PASA, 38, e053

Duchesne, S. W., Johnston-Hollitt, M., Riseley, C. J., Bartalucci, I., & Keel, S. R. 2022, MNRAS, 511, 3525

Duchesne, S. W., et al. 2023a, PASA, 40, e034

Duchesne, S. W., et al. 2023b, arXiv e-prints, p. arXiv:2311.12369

Dwarakanath, K. S., Parekh, V., Kale, R., & George, L. T. 2018, MNRAS, 477, 957

Enßlin, T. A., & Gopal-Krishna 2001, A&A, 366, 26

Enßlin, T. A., Biermann, P. L., Klein, U., & Kohle, S. 1998, A&A, 332, 395

Finoguenov, A., Sarazin, C. L., Nakazawa, K., Wik, D. R., & Clarke, T. E. 2010, ApJ, 715, 1143

Flaugher, B., et al. 2015, AJ, 150, 150

Gaensler, B. M., Landecker, T. L., Taylor, A. R., & POSSUM Collaboration 2010, in American Astronomical Society Meeting Abstracts #215. p. 470.13

George, L. T., et al. 2017, MNRAS,

Giacintucci, S., Markevitch, M., Cassano, R., Venturi, T., Clarke, T. E., & Brunetti, G. 2017, ApJ, 841, 71

Giacintucci, S., Markevitch, M., Cassano, R., Venturi, T., Clarke, T. E., Kale, R., & Cuciti, V. 2019, ApJ, 880, 70

Giacintucci, S., Markevitch, M., Johnston-Hollitt, M., Wik, D. R., Wang, Q. H. S., & Clarke, T. E. 2020, ApJ, 891, 1

Giacintucci, S., et al. 2022, ApJ, 934, 49

Green, D. A. 2011, Bull. Astronom. Soc. India, 39, 289

Gupta, Y., et al. 2017, Curr. Sci., 113, 707

Gupta, N., Huynh, M., Norris, R. P., Wang, X. R., Hopkins, A. M., Andernach, H., Koribalski, B. S., & Galvin, T. J. 2022, PASA, 39, e051

Gürkan, G., et al. 2022, MNRAS, 512, 6104

Guzzo, L., et al. 2009, A&A, 499, 357

Hale, C. L., et al. 2021, PASA, 38, e058

Hales, C. A., Murphy, T., Curran, J. R., Middelberg, E., Gaensler, B. M., & Norris, R. P. 2012, MNRAS, 425, 979

Hilton, M., et al. 2021, ApJS, 253, 3

Hindson, L., et al. 2014, MNRAS, 445, 330

Hoang, D. N., et al. 2022, A&A, 665, A60

Hodgson, T., Bartalucci, I., Johnston-Hollitt, M., McKinley, B., Vazza, F., & Wittor, D. 2021, ApJ, 909, 198

Hoeft, M., & Brüggen, M. 2007, MNRAS, 375, 77

Hotan, A. W., et al. 2014, PASA, 31, e041

Hotan, A. W., et al. 2021, PASA, 38, e009

Hunter, J. D. 2007, Comput, Sci. Eng., 9, 90

Huynh, M., Dempsey, J., Whiting, M. T., & Ophel, M. 2020, in Ballester P., Ibsen J., Solar M., Shortridge K., eds, Astronomical Society of the Pacific Conference Series Vol. 522, Astronomical Data Analysis Software and Systems XXVII. p. 263

HyeongHan, K., et al. 2020, ApJ, 900, 127

Jaffe, W. J. 1977, ApJ, 212, 1

James, C. W., et al. 2019, PASA, 36, e009

Johnston-Hollitt, M. 2003, PhD thesis, University of Adelaide, http://hdl.handle.net/2440/21954

Jones, D. H., et al. 2009, MNRAS, 399, 683

Jones, A., et al. 2023, A&A, 680, A31

Jones, E., Oliphant, T., Peterson, P., et al. 2001–2017, SciPy: Open source scientific tools for Python, http://www.scipy.org/

Joye, W. A., & Mandel, E. 2003, in Payne H. E., Jedrzejewski R. I., Hook R. N., eds, Astronomical Society of the Pacific Conference Series Vol. 295, Astronomical Data Analysis Software and Systems XII. p. 489

Kale, R., Dwarakanath, K. S., Bagchi, J., & Paul, S. 2012, MNRAS, 426, 1204

Kale, R., et al. 2022, MNRAS, 514, 5969

Kang, H. 2018, J,. Korean Astronom. Soc., 51, 185

Kempner, J. C., Blanton, E. L., Clarke, T. E., Enßlin, T. A., Johnston-Hollitt, M., & Rudnick, L. 2004, in Reiprich T., Kempner J., Soker N., eds, The Riddle of Cooling Flows in Galaxies and Clusters of galaxies. (arXiv:astro-ph/0310263)

Knowles, K., et al. 2021, MNRAS, 504, 1749

Knowles, K., et al. 2022, A&A, 657, A56

Koester, B. P., et al. 2007, ApJ, 660, 239

Koribalski, B. S., et al. 2020, Ap&SS, 365, 118

Kurahara, K., et al. 2023, PASJ, 75, S138

Lee, W., et al. 2022, ApJ, 924, 18

Liang, H., Hunstead, R. W., Birkinshaw, M., & Andreani, P. 2000, ApJ, 544, 686

Liu, A. et al. 2022, A&A, 661, A2

Loi, F., et al. 2023, A&A, 672, A28

Lovisari, L., et al. 2017, ApJ, 846, 51

Macgregor, P., et al. submitted, PASA

Macquart, J.-P., et al. 2010, PASA, 27, 272

Martinez Aviles, G., et al. 2018, A&A, 611, A94

Maturi, M., Bellagamba, F., Radovich, M., Roncarelli, M., Sereno, M., Moscardini, L., Bardelli, S., & Puddu, E. 2019, MNRAS, 485, 498

McConnell, D., et al. 2016, PASA, 33, e042

McConnell, D., et al. 2020, PASA, 37, e048

McMullin, J. P., Waters, B., Schiebel, D., Young, W., & Golap, K. 2007, in Shaw R. A., Hill F., Bell D. J., eds, Astronomical Society of the Pacific Conference Series Vol. 376, Astronomical Data Analysis Software and Systems XVI. p. 127

Mohan, N., & Rafferty, D. 2015, PyBDSF: Python Blob Detection and Source Finder (ascl:1502.007)

Murgia, M., Parma, P., de Ruiter, H. R., Bondi, M., Ekers, R. D., Fanti, R., & Fomalont, E. B. 2001, A&A, 380, 102

Murgia, M., Govoni, F., Markevitch, M., Feretti, L., Giovannini, G., Taylor, G. B., & Carretti, E. 2009, A&A, 499, 679

Murphy, T. 1999, PhD thesis, University of Sydney, http://www.astrop.physics.usyd.edu.au/RELICS/thesis/thesis.html

Murphy, T., et al. 2021, PASA, 38, e054

Nishiwaki, K., & Asano, K., 2022, ApJ, 934, 182

Norris, R. P., et al. 2011, PASA, 28, 215

Norris, R. P., et al. 2021, PASA, 38, e046

Offringa, A. R., & Smirnov, O. 2017, MNRAS, 471, 301

Offringa, A. R., et al. 2014, MNRAS, 444, 606

Orrú, E., Murgia, M., Feretti, L., Govoni, F., Brunetti, G., Giovannini, G., Girardi, M., & Setti, G. 2007, A&A, 467, 943

Pandge, M. B., Kale, R., Dabhade, P., Mahato, M., & Raychaudhury, S. 2022, MNRAS, 509, 1837

Paul, S., et al. 2023, Journal of Astrophysics and Astronomy, 44, 38

Pearce, C. J. J., et al. 2017, ApJ, 845, 81

Petrosian, V. 2001, ApJ, 557, 560

Piffaretti, R., Arnaud, M., Pratt, G. W., Pointecouteau, E., & Melin, J. B. 2011, A&A, 534, A109

PLANCK Collaboration et al. 2016a, A&A, 594, A27

PLANCK Collaboration et al. 2016b, A&A, 594, A27

Predehl, P., et al. 2021, A&A, 647, A1

Price-Whelan, A. M., et al. 2018, AJ, 156, 123

Quici, B., et al. 2021, PASA, 38, e008

Raba, R., et al. 2020, in Pizzo R., Deul E. R., Mol J. D., de Plaa J., Verkouter H., eds, Astronomical Society of the Pacific Conference Series Vol. 527, Astronomical Data Analysis Software and Systems XXIX. p. 271 (arXiv 1912.09439)

Rajpurohit, K., et al. 2018, ApJ, 852, 65

Rajpurohit, K., et al. 2020, A&A, 642, L13

Rajpurohit, K., et al. 2021, A&A, 646, A56

Ramatsoku, M., et al. 2020, A&A, 636, L1

Randall, S. W., Clarke, T. E., Nulsen, P. E. J., Owers, M. S., Sarazin, C. L., Forman, W. R., & Murray, S. S. 2010, ApJ, 722, 825

Rhee, J., et al. 2023, MNRAS, 518, 4646

Rigney, J., et al. 2022, MNRAS, 516, 540

Riseley, C. J., Scaife, A. M. M., Oozeer, N., Magnus, L., & Wise, M. W. 2015, MNRAS, 447, 1895

Riseley, C. J., et al. 2022a, MNRAS, 512, 4210

Riseley, C. J., et al. 2022b, MNRAS, 515, 1871

Riseley, C. J., et al. 2023, MNRAS, 524, 6052

Robitaille, T., Bressert, E. 2012, APLpy: Astronomical Plotting Library in Python, Astrophysics Source Code Library (ascl 1208.017)

Röttgering, H. J. A., Wieringa, M. H., Hunstead, R. W., & Ekers, R. D. 1997, MNRAS, 290, 577

Rudnick, L. 2002, PASP, 114, 427

Schellenberger, G., et al. 2022, ApJ, 925, 91

Segal, G., et al. 2023, MNRAS, 521, 1429

Shakouri, S., Johnston-Hollitt, M., & Pratt, G. W. 2016, MNRAS, 459, 2525

Shimwell, T. W., et al. 2022, A&A, 659, A1

Shweta, A., Athreya, R., & Sekhar, S. 2020, ApJ, 897, 115

Sikhosana, S. P., Knowles, K., Hilton, M., Moodley, K., & Murgia, M. 2023, MNRAS, 518, 4595

Skillman, S. W., Xu, H., Hallman, E. J., O'Shea, B. W., Burns, J. O., Li, H., Collins, D. C., & Norman, M. L. 2013, ApJ, 765, 21

Slee, O. B., & Reynolds, J. E. 1984, PASA, 5, 516

Slee, O. B., Roy, A. L., Murgia, M., Andernach, H., & Ehle, M. 2001, AJ, 122, 1172

Smirnov, O. M., & Tasse, C. 2015, MNRAS, 449, 2668

Strüder, L. et al., 2001, A&A, 365, L18

Tasse, C. 2014, A&A, 566, A127

Tasse, C., et al. 2018, A&A, 611, A87

Taylor, M. B. 2005, in Shopbell P., Britton M., Ebert R., eds, Astronomical Society of the Pacific Conference Series Vol. 347, Astronomical Data Analysis Software and Systems XIV. p. 29

Thomson, A. J. M., et al. 2023, PASA, 40, e040

Tingay, S. J., et al. 2013, PASA, 30, 7

Tonry, J. L., et al. 2012, ApJ, 750, 99

Trehaeven, K. S., et al. 2023, MNRAS, 520, 4410

Turner, M. J. L., et al. 2001, A&A, 365, L27

Urdampilleta, I., Akamatsu, H., Mernier, F., Kaastra, J. S., de Plaa, J., Ohashi, T., Ishisaki, Y., & Kawahara, H. 2018, A&A, 618, A74

Vacca, V., et al. 2022a, MNRAS, 511, 3389

Vacca, V., et al. 2022b, MNRAS, 514, 4969

Vazza, F., Wittor, D., Brunetti, G., & Brüggen, M. 2021, A&A, 653, A23

Velović, V., Cotton, W. D., Filipović, M. D., Norris, R. P., Barnes, L. A., & Condon, J. J., 2023, MNRAS, 523, 1933

Venturi, T., Bardelli, S., Dallacasa, D., Brunetti, G., Giacintucci, S., Hunstead, R. W., & Morganti, R. 2003, A&A, 402, 913

Venturi, T., et al. 2022, A&A, 660, A81

Wayth, R. B., et al. 2018, PASA, 35

Wen, Z. L., Han, J. L., & Liu, F. S. 2009, ApJS, 183, 197

Wilber, A. G., Johnston-Hollitt, M., Duchesne, S. W., Tasse, C., Akamatsu, H., Intema, H., & Hodgson, T. 2020, PASA, 37, e040

Wittor, D., Brüggen, M., Grete, P., & Rajpurohit, K. 2023, MNRAS, 523, 701

Xie, C., et al. 2020, A&A, 636, A3

Ye, H., Gull, S. F., Tan, S. M., & Nikolic, B. 2021, High dynamic range wide field imaging method in radio interferometry (arXiv 2101.11172)

Yuan, Z. S., Han, J. L., & Wen, Z. L. 2022, MNRAS, 513, 3013

Zhang, X., et al. 2023, A&A, 672, A42

de Gasperin, F., van Weeren, R. J., Brüggen, M., Vazza, F., Bonafede, A., & Intema, H. T. 2014, MNRAS, 444, 3130

de Gasperin, F., et al. 2017, Sci. Adv., 3, e1701634

de Gasperin, F., et al. 2022, A&A, 659, A146

de Jong, J. M. G. H. J., et al. 2022, A&A, 668, A107

van Haarlem, M. P., et al. 2013, A&A, 556, A2

van Weeren, R. J., Röttgering, H. J. A., Intema, H. T., Rudnick, L., Brüggen, M., Hoeft, M., & Oonk, J. B. R. 2012, A&A, 546, A124

van Weeren, R. J., et al. 2017, Nat. Astron., 1, 0005

van Weeren, R. J., de Gasperin, F., Akamatsu, H., Brüggen, M., Feretti, L., Kang, H., Stroe, A., & Zandanel, F. 2019, Space Sci. Rev., 215, 16

van Weeren, R. J., et al. 2021, A&A, 651, A115

van der Walt, S., Colbert, S. C., & Varoquaux, G. 2011, Comput. Sci. Eng., 13, 22

A. Cluster images

We summarise the image properties in Table A1 (rms noise) and Table A2 (PSF) for the individual cluster images, including the archival image. For Table A1, the rms noise is calculated within a 2 Mpc circle around the cluster centre. Figures A1(i)–A1(lxxi) shows ASKAP images for each cluster in our sample. For each cluster, we show the robust $+0.25$ reference image and the tapered, compact source-subtracted image. In each panel we label the diffuse sources of interest, and show dashed, black polygon regions which are used for integrated flux density measurements. More comprehensive images of all clusters (e.g. Figure 7), along with the FITS files for the reprocessed radio data, will be provided in the PASA Datastore. In the PDF document, a link is included in the caption for clusters with a corresponding entry in Section 4.4.

Table A1. Image noise properties within 2 Mpc of the cluster in μJy PSF^{-1}.

Cluster	Archive	robust 0.0	robust +0.25	uniform	100 kpc taper	250 kpc taper
PSZ2 G006.16−69.49	48.0	39.4	38.9	68.5	126	561
PSZ2 G008.31−64.74	66.6	75.5	75.1	140.7	202	943
PSZ2 G011.06−63.84	43.8	38.9	38.8	66.7	108	359
PSZ2 G011.92−63.53	43.9	36.9	38.3	53.9	121	513
PSZ2 G014.72−62.49	40.5	36.6	37.8	52.0	68	255
PSZ2 G017.25−70.71	57.9	49.0	46.3	91.1	84	288
PSZ2 G018.18−60.00	52.3	41.8	40.2	79.8	98	347
PSZ2 G018.76−61.65	43.1	35.1	35.4	55.1	126	588
PSZ2 G110.28−87.48	33.0	27.8	30.4	44.1	63	166
PSZ2 G149.63−84.19	40.5	32.3	32.6	45.5	323	2149
PSZ2 G167.43−53.67	67.5	44.7	44.6	65.9	233	977
PSZ2 G167.66−65.59	75.6	42.0	41.7	63.1	112	516
PSZ2 G167.98−59.95	60.0	32.9	32.4	49.5	181	887
PSZ2 G172.98−53.55	96.0	52.6	53.2	74.1	120	462
PSZ2 G174.40−57.33	67.3	37.5	38.2	51.2	174	1017
PSZ2 G175.69−85.98	40.7	42.5	46.0	64.7	239	1003
PSZ2 G180.74−85.21	43.3	40.1	39.2	69.2	131	473
PSZ2 G219.88+22.83	83.6	75.9	76.2	105.7	218	825
PSZ2 G220.11+22.91	67.5	63.3	61.5	88.4	202	960
PSZ2 G223.47+26.85	56.7	42.1	42.6	71.6	99	307
PSZ2 G225.48+29.41	67.8	43.4	49.1	52.4	381	1916
PSZ2 G227.59+22.98	77.4	52.7	54.8	77.4	314	1482
PSZ2 G227.89+36.58	64.8	56.7	66.2	65.6	211	967
PSZ2 G228.38+38.58	46.3	40.6	41.9	66.0	82	286
PSZ2 G228.50+34.95	45.4	39.1	40.0	61.1	142	779
PSZ2 G230.73+27.70	53.9	42.6	44.8	64.9	159	800
PSZ2 G231.79+31.48	66.0	50.9	50.3	90.1	122	579
PSZ2 G232.84+38.13	61.1	54.2	55.9	85.8	415	1809
PSZ2 G233.68+36.14	67.2	56.8	62.2	79.7	209	982
PSZ2 G236.92−26.65	37.2	34.3	35.3	53.6	206	1044
PSZ2 G239.27−26.01	40.4	37.4	42.8	56.6	132	617
PSZ2 G241.79−24.01	79.9	58.4	63.6	76.5	779	5433
PSZ2 G241.98+19.56	33.7	29.4	29.2	47.8	78	379
PSZ2 G254.52+08.27	36.6	31.8	32.1	57.4	150	898
PSZ2 G260.80+06.71	39.6	37.7	42.4	49.8	278	1885
PSZ2 G262.36−25.15	47.8	44.1	50.2	55.1	958	3281
PSZ2 G263.14−23.41	33.1	32.1	35.2	51.6	185	1005
PSZ2 G263.19−25.19	37.6	43.8	51.1	45.3	422	2252
PSZ2 G263.68−22.55	40.7	45.0	43.7	84.3	222	1309
PSZ2 G265.21−24.83	31.2	31.3	30.4	56.6	640	4309
PSZ2 G270.63−35.67	38.6	36.5	38.5	79.7	83	253
PSZ2 G271.28−36.11	37.4	34.4	37.8	62.5	118	412
PSZ2 G272.08−40.16	69.2	61.3	70.2	59.1	629	4049
PSZ2 G275.24−40.42	47.8	46.5	48.0	75.4	137	506
PSZ2 G275.73−06.12	30.9	31.0	33.3	41.0	164	895
PSZ2 G276.09−41.53	59.8	58.3	57.3	104.1	297	1913
PSZ2 G276.14−07.68	32.7	34.5	39.1	52.7	255	1421

Table A1. Continued.

Cluster	Archive	robust 0.0	robust +0.25	uniform	100 kpc taper	250 kpc taper
PSZ2 G282.32—40.15	32.4	33.4	34.0	73.5	91	309
PSZ2 G286.28—38.36	44.2	40.7	46.2	69.5	123	618
PSZ2 G286.75—37.35	50.1	55.0	59.6	116.9	116	427
PSZ2 G311.98+30.71	34.6	32.9	34.9	51.6	1608	9935
PSZ2 G313.33+30.29	33.2	33.2	35.1	53.2	1274	7113
PSZ2 G328.58—25.25	49.5	44.0	42.5	89.5	138	517
PSZ2 G331.96—45.74	31.7	29.9	31.0	49.7	510	4021
PSZ2 G332.11—23.63	33.8	34.3	34.7	67.8	128	639
PSZ2 G332.23—46.37	32.5	28.6	29.9	48.5	326	1701
PSZ2 G332.29—23.57	55.2	110.6	100.6	212.5	8406	7869
PSZ2 G333.89—43.60	36.8	31.4	32.7	58.1	89	310
PSZ2 G335.58—46.44	35.5	30.9	33.6	48.7	565	3852
PSZ2 G336.95—45.75	33.7	31.7	33.1	53.5	621	2801
PSZ2 G337.99—33.61	36.7	35.8	34.1	72.7	87	290
PSZ2 G339.74—51.08	58.3	60.0	54.9	125.0	189	1209
PSZ2 G340.35—42.80	31.3	30.3	31.8	49.7	100	405
PSZ2 G341.19—36.12	41.8	40.2	43.1	66.5	138	688
PSZ2 G341.44—40.19	39.0	34.4	38.3	51.6	182	1043
PSZ2 G342.33—34.93	59.2	65.1	74.2	86.4	358	1966
PSZ2 G342.62—39.60	52.9	47.8	53.5	64.8	437	3321
PSZ2 G345.38—39.32	37.1	36.1	38.4	57.0	124	583
PSZ2 G345.82—34.29	38.4	24.1	24.8	37.8	858	6319
PSZ2 G346.86—45.38	31.1	33.7	36.7	47.2	462	2591
PSZ2 G347.58—35.35	31.9	30.1	30.2	56.3	126	525

Table A2. Image PSFs (arcsec × arcsec, deg).

Cluster	Archive	robust 0.0	robust +0.25	uniform	100 kpc taper	250 kpc taper
PSZ2 G006.16−69.49	10.1 × 8.5, 82.6	13.3 × 10.5, 87.8	15.2 × 12.0, 92.1	9.9 × 7.6, 79.2	33 × 32, 87.2	70 × 68, 88.6
PSZ2 G008.31−64.74	10.0 × 8.5, 83.7	13.0 × 10.6, 87.0	14.7 × 11.8, 95.5	9.5 × 7.3, 76.6	28 × 27, 104.1	58 × 56, 97.3
PSZ2 G011.06−63.84	10.0 × 8.5, 83.7	13.0 × 10.6, 88.2	14.8 × 11.8, 96.8	9.6 × 7.3, 77.4	34 × 33, 83.9	70 × 68, 95.6
PSZ2 G011.92−63.53	10.0 × 8.5, 83.7	13.2 × 10.7, 88.8	15.0 × 11.9, 97.3	9.9 × 7.7, 79.1	32 × 32, 89.8	67 × 66, 84.0
PSZ2 G014.72−62.49	10.0 × 8.5, 83.7	13.2 × 10.7, 89.9	15.0 × 11.9, 98.5	10.0 × 7.7, 79.7	23 × 21, 106.3	46 × 44, 80.4
PSZ2 G017.25−70.71	10.1 × 8.5, 82.6	13.3 × 10.5, 89.4	15.2 × 12.0, 93.3	10.1 × 7.7, 80.2	29 × 27, 100.1	58 × 56, 83.2
PSZ2 G018.18−60.00	10.0 × 8.5, 83.7	13.1 × 10.6, 91.5	15.0 × 11.8, 100.3	9.7 × 7.3, 79.2	31 × 30, 105.0	66 × 64, 94.7
PSZ2 G018.76−61.65	10.0 × 8.5, 83.7	13.2 × 10.7, 91.1	15.1 × 11.9, 99.8	10.1 × 7.7, 80.7	32 × 32, 98.4	68 × 66, 84.5
PSZ2 G110.28−87.48	12.4 × 9.9, 86.5	12.9 × 9.8, 96.1	15.0 × 10.8, 102.6	9.6 × 7.0, 89.6	25 × 21, 115.0	45 × 43, 90.6
PSZ2 G149.63−84.19	12.6 × 9.7, −87.5	13.7 × 9.7, 100.4	15.6 × 11.1, 102.6	11.1 × 7.8, 89.9	51 × 48, 79.4	112 × 110, 80.2
PSZ2 G167.43−53.67	18.0 × 18.0, 0.0	13.6 × 10.9, 85.0	14.8 × 12.3, 79.4	12.1 × 8.6, 86.2	40 × 36, 100.8	81 × 74, 110.8
PSZ2 G167.66−65.59	18.0 × 18.0, 0.0	12.7 × 10.7, 84.7	14.0 × 11.8, 92.2	10.7 × 8.1, 94.3	26 × 24, 122.9	51 × 48, 105.9
PSZ2 G167.98−59.95	18.0 × 18.0, 0.0	13.8 × 10.8, 84.4	15.4 × 12.3, 79.7	11.9 × 8.3, 87.3	49 × 44, 88.1	103 × 93, 112.2
PSZ2 G172.98−53.55	18.0 × 18.0, 0.0	13.5 × 10.7, 86.0	14.7 × 12.1, 79.7	12.0 × 8.5, 88.4	28 × 25, 108.3	56 × 52, 94.7
PSZ2 G174.40−57.33	18.0 × 18.0, 0.0	12.9 × 11.0, 86.0	14.1 × 12.2, 96.0	11.1 × 8.2, 91.6	39 × 37, 100.3	81 × 74, 109.1
PSZ2 G175.69−85.98	12.6 × 9.7, −87.5	13.1 × 10.0, 95.1	15.1 × 11.0, 101.3	9.7 × 7.0, 89.1	35 × 33, 98.7	70 × 68, 92.2
PSZ2 G180.74−85.21	12.6 × 9.7, −87.5	13.2 × 10.0, 94.9	15.2 × 11.1, 101.0	9.7 × 7.0, 89.0	37 × 35, 93.1	77 × 75, 93.0
PSZ2 G219.88+22.83	13.4 × 12.4, −89.5	14.9 × 11.8, 113.3	16.4 × 13.2, 117.5	12.8 × 9.4, 103.7	37 × 34, 124.8	72 × 68, 100.0
PSZ2 G220.11+22.91	13.4 × 12.4, −89.5	14.9 × 11.8, 112.8	16.4 × 13.2, 117.1	12.8 × 9.4, 103.3	39 × 36, 124.6	74 × 69, 99.8
PSZ2 G223.47+26.85	13.4 × 12.4, −89.5	14.1 × 12.2, 129.3	16.1 × 13.7, 136.6	11.3 × 9.7, 90.9	31 × 28, 143.0	58 × 56, 113.4
PSZ2 G225.48+29.41	13.5 × 12.5, −80.5	13.4 × 11.4, 103.2	15.2 × 12.4, 114.4	11.2 × 8.2, 90.7	38 × 36, 123.7	77 × 74, 104.8
PSZ2 G227.59+22.98	13.3 × 11.9, 83.9	14.4 × 10.8, 93.6	15.8 × 12.3, 97.0	12.5 × 7.6, 88.1	36 × 32, 69.0	64 × 61, 77.9
PSZ2 G227.89+36.58	13.4 × 12.5, 83.0	13.3 × 12.3, 109.3	15.1 × 13.1, 123.4	11.2 × 9.2, 86.3	25 × 23, 133.9	50 × 48, 165.6
PSZ2 G228.38+38.58	13.4 × 12.5, 83.0	13.8 × 11.7, 95.8	15.4 × 13.2, 101.6	12.0 × 8.8, 76.4	25 × 22, 100.2	46 × 45, 131.7
PSZ2 G228.50+34.95	13.4 × 12.5, 83.0	13.8 × 11.8, 111.1	15.4 × 13.2, 116.9	11.7 × 9.0, 88.8	32 × 30, 134.7	64 × 62, 104.1
PSZ2 G230.73+27.70	13.2 × 11.6, 89.5	14.0 × 11.5, 118.2	15.8 × 13.0, 126.0	11.9 × 9.3, 90.2	33 × 30, 129.8	62 × 58, 104.3
PSZ2 G231.79+31.48	13.3 × 12.1, 86.9	14.4 × 10.6, 107.2	15.8 × 12.0, 111.0	12.5 × 7.8, 95.6	30 × 27, 119.0	59 × 54, 106.3
PSZ2 G232.84+38.13	13.4 × 12.5, 83.0	14.0 × 11.8, 106.3	15.5 × 13.4, 112.3	12.0 × 8.8, 86.6	46 × 45, 163.8	95 × 91, 99.3
PSZ2 G233.68+36.14	13.3 × 12.1, 86.9	14.4 × 11.2, 107.2	15.8 × 12.7, 111.3	12.5 × 8.4, 90.6	29 × 27, 126.1	56 × 54, 117.3
PSZ2 G236.92−26.65	12.1 × 9.7, 85.4	12.5 × 10.0, 85.9	14.1 × 11.1, 91.8	9.3 × 7.0, 80.2	44 × 42, 73.1	97 × 95, 89.8
PSZ2 G239.27−26.01	12.1 × 9.7, 85.4	12.4 × 10.1, 84.0	13.9 × 11.0, 91.0	9.1 × 6.9, 78.3	24 × 22, 97.9	49 × 47, 100.8
PSZ2 G241.79−24.01	12.1 × 9.7, 85.4	12.5 × 10.2, 82.5	14.0 × 11.2, 89.8	9.1 × 7.0, 77.4	45 × 44, 79.7	100 × 99, 111.3
PSZ2 G241.98+19.56	12.4 × 10.5, 81.4	13.1 × 10.5, 92.0	14.8 × 11.6, 99.9	10.3 × 7.7, 83.2	31 × 30, 105.5	63 × 61, 94.2
PSZ2 G254.52+08.27	12.3 × 10.1, 80.8	12.6 × 10.1, 84.3	14.3 × 11.3, 90.1	9.1 × 6.9, 77.7	36 × 35, 86.0	77 × 75, 101.9
PSZ2 G260.80+06.71	12.5 × 10.3, 80.2	12.6 × 10.2, 80.9	14.3 × 11.4, 85.7	9.0 × 6.9, 74.4	36 × 35, 84.1	77 × 75, 102.5
PSZ2 G262.36−25.15	11.2 × 9.5, 86.7	11.5 × 9.7, 83.8	12.9 × 10.9, 88.1	8.4 × 6.8, 73.5	37 × 36, 86.0	81 × 80, 87.7
PSZ2 G263.14−23.41	11.2 × 9.5, 86.7	11.3 × 10.0, 79.4	12.6 × 11.5, 85.4	8.2 × 6.7, 69.9	32 × 32, 81.0	69 × 68, 108.9
PSZ2 G263.19−25.19	11.2 × 9.5, 86.7	11.7 × 9.9, 83.4	13.2 × 11.1, 87.9	9.2 × 7.4, 75.6	38 × 37, 87.7	82 × 81, 88.6
PSZ2 G263.68−22.55	11.2 × 9.5, 86.7	11.3 × 10.0, 79.1	12.7 × 11.6, 85.2	8.2 × 6.8, 69.8	39 × 38, 80.6	87 × 87, 99.1
PSZ2 G265.21−24.83	11.2 × 9.5, 86.7	11.8 × 10.1, 83.2	13.4 × 11.5, 88.1	8.5 × 6.9, 71.8	92 × 89, 44.5	221 × 202, 14.3
PSZ2 G270.63−35.67	13.9 × 11.4, −88.8	13.9 × 11.1, 87.3	16.0 × 12.9, 91.9	9.1 × 7.1, 77.8	30 × 26, 104.8	61 × 58, 102.3
PSZ2 G271.28−36.11	13.9 × 11.4, −88.8	14.1 × 11.3, 88.2	16.3 × 13.1, 92.8	9.1 × 7.2, 78.2	33 × 30, 102.5	68 × 65, 104.1
PSZ2 G272.08−40.16	15.5 × 13.7, −6.2	15.2 × 13.9, 35.9	16.8 × 15.8, 59.3	12.8 × 10.5, 9.6	51 × 46, 65.7	107 × 103, 61.2
PSZ2 G275.24−40.42	15.5 × 13.7, −6.2	15.2 × 13.6, 33.2	16.9 × 15.6, 53.5	12.0 × 9.5, 177.1	37 × 34, 75.8	77 × 75, 89.9
PSZ2 G275.73−06.12	12.3 × 10.7, 81.3	12.8 × 11.0, 78.4	14.5 × 12.5, 83.9	9.7 × 8.1, 72.2	36 × 35, 106.7	77 × 76, 98.6
PSZ2 G276.09−41.53	15.5 × 13.7, −6.2	15.5 × 13.8, 40.1	17.3 × 15.7, 59.3	12.2 × 9.6, 1.6	47 × 44, 74.6	100 × 97, 83.7
PSZ2 G276.14−07.68	12.3 × 10.7, 81.3	13.0 × 10.8, 74.2	14.9 × 12.4, 78.7	9.4 × 7.0, 61.9	36 × 35, 98.2	77 × 75, 102.2
PSZ2 G282.32−40.15	13.9 × 12.0, −84.8	14.0 × 11.8, 93.0	16.3 × 13.6, 98.8	9.0 × 7.4, 78.7	37 × 34, 108.8	79 × 76, 111.0

Table A2. Continued.

| Cluster	Archive	robust 0.0	robust +0.25	uniform	100 kpc taper	250 kpc taper
PSZ2 G286.28−38.36	13.9 × 12.0, −84.8	14.0 × 12.0, 92.8	16.2 × 13.8, 99.4	8.9 × 7.8, 71.7	29 × 26, 105.7	59 × 57, 109.2
PSZ2 G286.75−37.35	13.9 × 12.0, −84.8	14.0 × 12.0, 90.8	16.2 × 13.9, 97.7	8.9 × 7.9, 67.1	24 × 22, 102.6	48 × 45, 111.3
PSZ2 G311.98+30.71	12.3 × 9.9, 85.5	12.9 × 10.4, 86.7	14.7 × 11.6, 92.7	9.3 × 7.3, 80.7	102 × 98, 60.3	245 × 230, 177.6
PSZ2 G313.33+30.29	12.3 × 9.9, 85.5	12.9 × 10.4, 86.1	14.6 × 11.6, 91.9	9.3 × 7.3, 80.5	100 × 96, 61.0	240 × 225, 172.6
PSZ2 G328.58−25.25	12.3 × 11.2, 83.0	12.6 × 11.4, 77.1	14.3 × 13.1, 87.5	8.6 × 7.3, 64.2	38 × 37, 110.2	83 × 81, 114.4
PSZ2 G331.96−45.74	12.1 × 10.7, 85.3	12.4 × 10.8, 82.2	13.8 × 12.0, 82.8	9.0 × 7.3, 71.5	72 × 70, 72.9	162 × 156, 30.1
PSZ2 G332.11−23.63	12.3 × 11.2, 83.0	12.6 × 11.1, 77.7	14.2 × 12.8, 85.3	8.6 × 7.1, 66.7	36 × 34, 111.4	77 × 76, 112.0
PSZ2 G332.23−46.37	12.1 × 10.7, 85.3	12.6 × 10.9, 82.6	14.2 × 12.4, 87.4	8.8 × 7.4, 75.4	58 × 57, 74.0	133 × 129, 43.3
PSZ2 G332.29−23.57	12.3 × 11.2, 83.0	12.9 × 11.5, 78.2	14.6 × 13.2, 86.4	9.3 × 8.0, 70.6	106 × 103, 40.6	250 × 232, 166.7
PSZ2 G333.89−43.60	12.1 × 10.7, 85.3	12.1 × 11.0, 80.3	13.6 × 12.8, 87.9	8.7 × 7.1, 65.9	28 × 27, 128.9	57 × 55, 108.3
PSZ2 G335.58−46.44	12.1 × 9.9, 80.5	12.3 × 10.6, 81.1	13.7 × 12.0, 84.9	8.8 × 7.0, 67.9	69 × 68, 50.4	156 × 149, 47.3
PSZ2 G336.95−45.75	12.1 × 9.9, 80.5	12.2 × 10.5, 80.7	13.7 × 11.9, 83.9	8.8 × 6.9, 68.3	68 × 66, 52.3	155 × 145, 39.8
PSZ2 G337.99−33.61	12.5 × 10.9, 78.8	12.8 × 10.9, 78.8	14.7 × 12.9, 86.7	9.4 × 6.9, 70.8	37 × 35, 94.1	77 × 76, 105.3
PSZ2 G339.74−51.08	12.1 × 9.9, 80.5	12.2 × 10.3, 80.7	13.6 × 11.6, 84.2	8.7 × 7.0, 70.4	35 × 34, 158.2	76 × 75, 100.6
PSZ2 G340.35−42.80	14.0 × 10.9, −58.2	14.0 × 11.4, 113.5	15.8 × 13.1, 109.4	10.9 × 7.7, 120.4	35 × 34, 106.2	77 × 75, 103.0
PSZ2 G341.19−36.12	12.0 × 10.7, 84.8	12.3 × 10.9, 83.5	13.8 × 12.6, 91.8	8.7 × 7.0, 72.8	29 × 28, 83.6	60 × 59, 100.4
PSZ2 G341.44−40.19	14.0 × 10.9, −58.2	12.2 × 10.8, 81.8	13.7 × 12.6, 89.5	8.7 × 7.1, 70.6	31 × 31, 88.9	66 × 64, 101.9
PSZ2 G342.33−34.93	12.0 × 10.7, 84.8	15.8 × 10.6, 65.4	17.0 × 13.2, 72.0	12.7 × 6.3, 65.8	33 × 32, 90.2	70 × 68, 101.1
PSZ2 G342.62−39.60	12.0 × 10.7, 84.8	12.4 × 11.0, 83.4	14.0 × 12.8, 91.5	8.8 × 7.1, 71.6	45 × 44, 92.5	101 × 99, 93.0
PSZ2 G345.38−39.32	14.8 × 11.1, −59.0	14.9 × 11.6, 117.4	16.7 × 13.3, 111.4	12.1 × 8.3, 126.5	34 × 33, 96.8	73 × 71, 89.6
PSZ2 G345.82−34.29	12.0 × 10.1, 86.1	12.6 × 11.1, 74.9	14.1 × 12.9, 84.4	9.6 × 7.9, 58.6	97 × 92, 54.5	235 × 213, 161.6
PSZ2 G346.86−45.38	12.1 × 10.1, 89.1	14.8 × 11.5, 115.4	16.7 × 13.2, 109.6	11.5 × 7.8, 122.6	68 × 67, 74.1	156 × 153, 19.3
PSZ2 G347.58−35.35	12.0 × 10.1, 86.1	12.3 × 10.3, 82.4	13.9 × 11.5, 87.1	8.8 × 7.1, 73.9	33 × 32, 100.7	71 × 70, 101.6
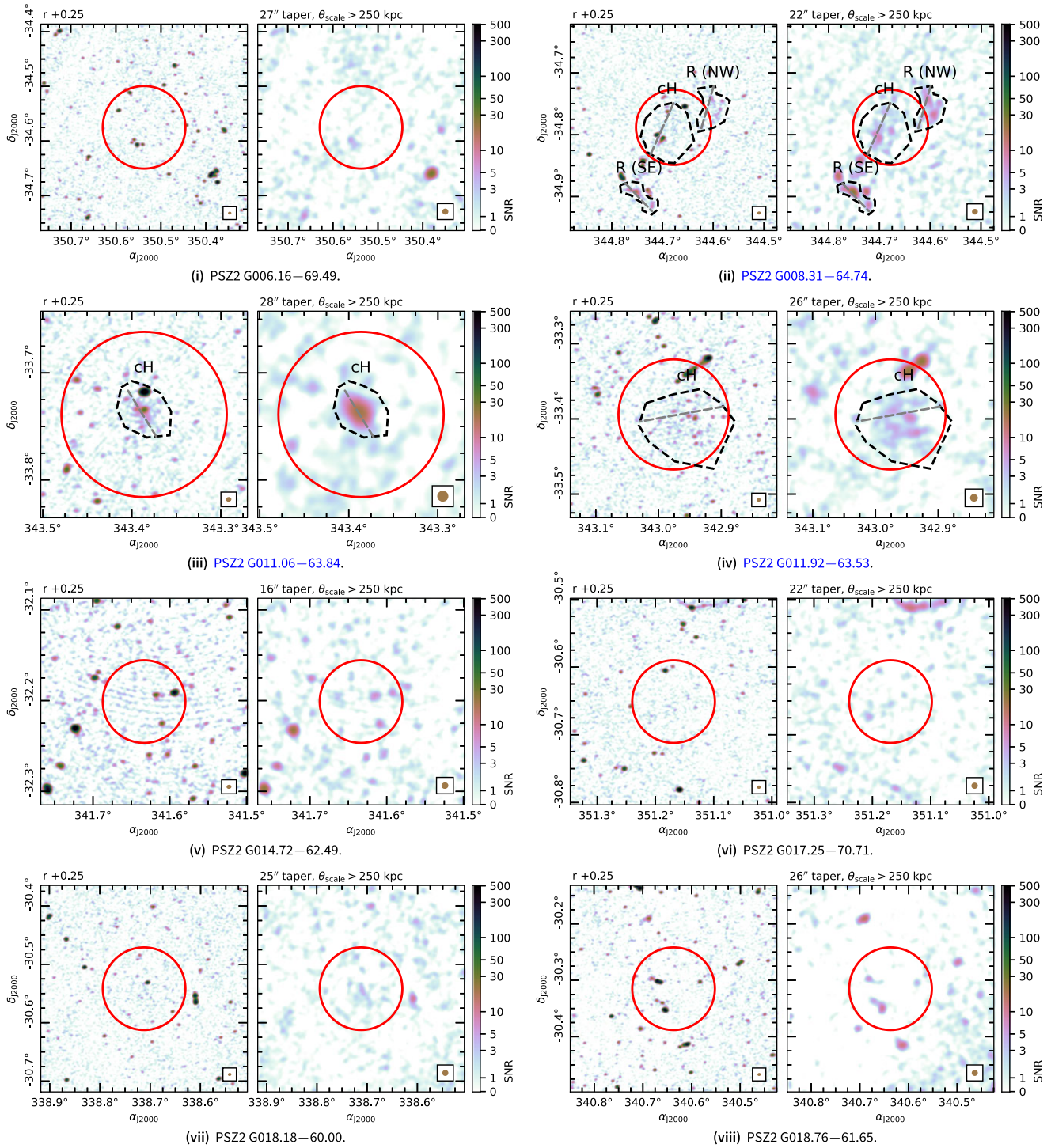
Figure A1. Radio images of the clusters. *Left.* The robust +0.25 reference image. *Right.* The robust +0.25 image, tapered, after subtraction of sources of scales < 250 kpc. In both panels, the red circle has a 1 Mpc radius at the redshift of the clusters (dashed indicates an assumed redshift of 0.2). Dashed polygon regions indicate the diffuse sources of interest and are the region used for integrated flux density measurements. The PSF of each image is shown in the bottom right corner.
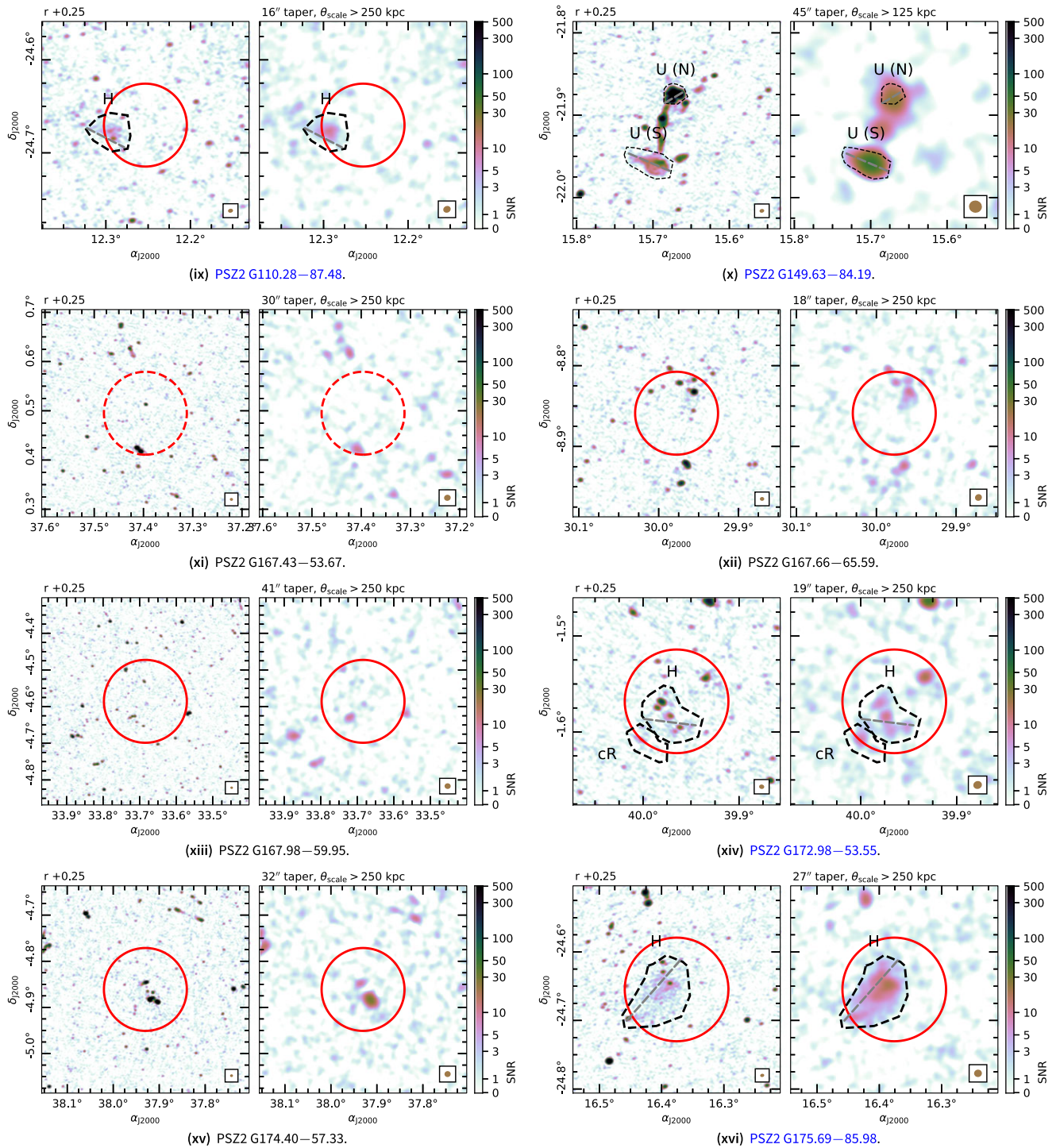
(ix) PSZ2 G110.28−87.48.

(x) PSZ2 G149.63−84.19.

(xi) PSZ2 G167.43−53.67.

(xii) PSZ2 G167.66−65.59.

(xiii) PSZ2 G167.98−59.95.

(xiv) PSZ2 G172.98−53.55.

(xv) PSZ2 G174.40−57.33.

(xvi) PSZ2 G175.69−85.98.

Figure A1. Continued.

(xvii) PSZ2 G180.74−85.21.

(xviii) PSZ2 G219.88+22.83.

(xix) PSZ2 G220.11+22.91.

(xx) PSZ2 G223.47+26.85.

(xxi) PSZ2 G225.48+29.41.

(xxii) PSZ2 G227.59+22.98.

(xxiii) PSZ2 G227.89+36.58.

(xxiv) PSZ2 G228.38+38.58.

Figure A1. Continued.

(xxv) PSZ2 G228.50+34.95.

(xxvi) PSZ2 G230.73+27.70.

(xxvii) PSZ2 G231.79+31.48.

(xxviii) PSZ2 G232.84+38.13.

(xxix) PSZ2 G233.68+36.14.

(xxx) PSZ2 G236.92−26.65.

(xxxi) PSZ2 G239.27−26.01.

(xxxii) PSZ2 G241.79−24.01.

Figure A1. Continued.

(xxxiii) PSZ2 G241.98+19.56.

(xxxiv) PSZ2 G254.52+08.27.

(xxxv) PSZ2 G260.80+06.71.

(xxxvi) PSZ2 G262.36−25.15.

(xxxvii) PSZ2 G263.14−23.41.

(xxxviii) PSZ2 G263.19−25.19.

(xxxix) PSZ2 G263.68−22.55.

(xl) PSZ2 G265.21−24.83.

Figure A1. Continued.

(xli) PSZ2 G270.63−35.67.

(xlii) PSZ2 G271.28−36.11.

(xliii) PSZ2 G272.08−40.16.

(xliv) PSZ2 G275.24−40.42.

(xlv) PSZ2 G275.73−06.12.

(xlvi) PSZ2 G276.09−41.53.

(xlvii) PSZ2 G276.14−07.68.

(xlviii) PSZ2 G282.32−40.15.

Figure A1. Continued.

(xlix) PSZ2 G286.28—38.36.

(l) PSZ2 G286.75—37.35.

(li) PSZ2 G311.98+30.71.

(lii) PSZ2 G313.33+30.29.

(liii) PSZ2 G328.58—25.25.

(liv) PSZ2 G331.96—45.74.

(lv) PSZ2 G332.11—23.63.

(lvi) PSZ2 G332.23—46.37.

Figure A1. Continued.

(lvii) PSZ2 G332.29−23.57.

(lviii) PSZ2 G333.89−43.60.

(lix) PSZ2 G335.58−46.44.

(lx) PSZ2 G336.95−45.75.

(lxi) PSZ2 G337.99−33.61.

(lxii) PSZ2 G339.74−51.08.

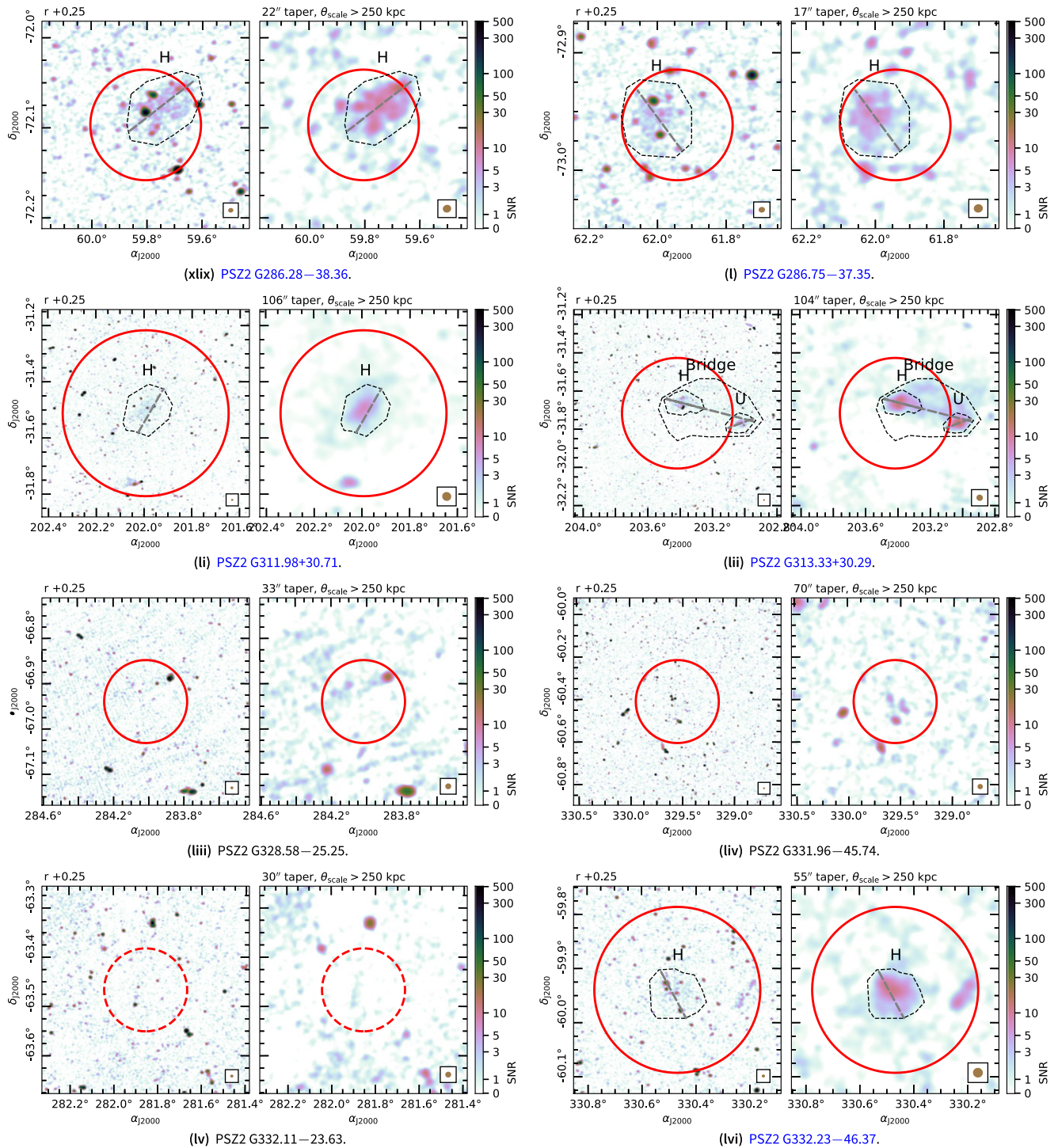**(lxiii)** PSZ2 G340.35−42.80.
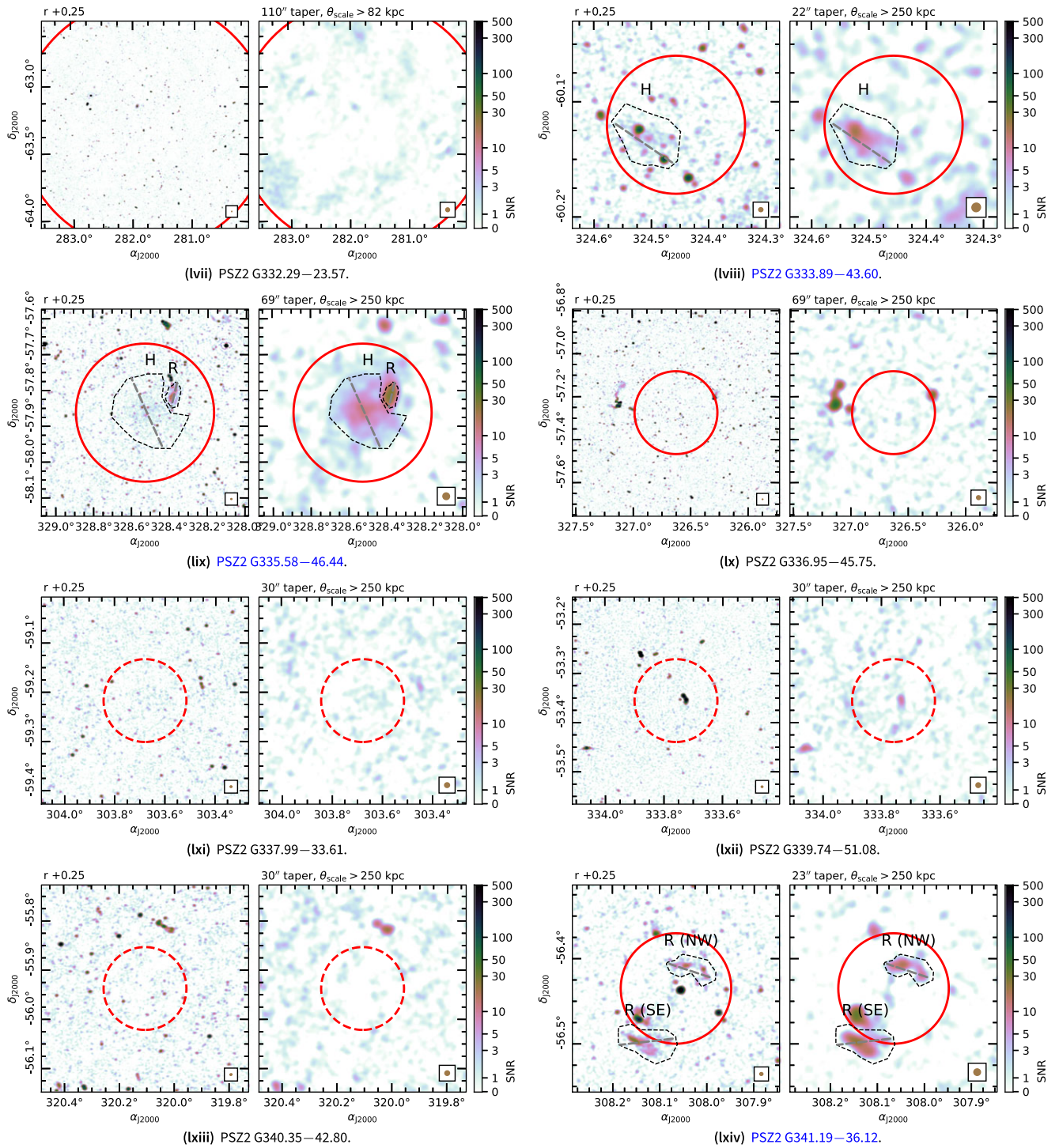
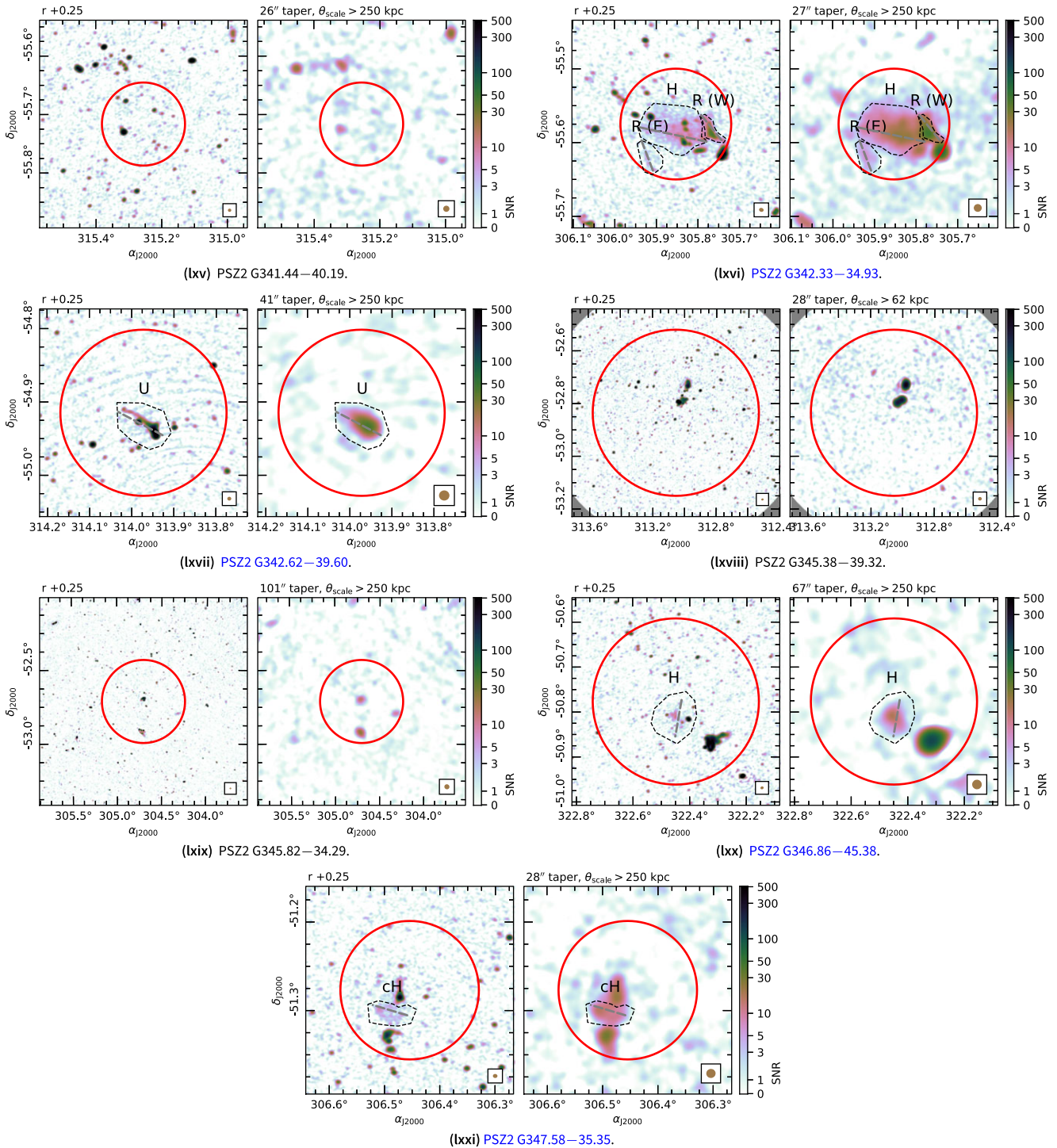**(lxiv)** PSZ2 G341.19−36.12.

Figure A1. Continued.

Figure A1. Continued.

B. Halo models

Figure B1 shows the halo models output from `Halo-FDCA` (middle panels) along with the images used for model fitting (left panels) and the residuals after subtraction of the model from the data (right panels). The black, dashed contours on the left panels show the halo model, and regions that are masked are shown in grey.

Only the best-fit model is shown (i.e. with the lowest reduced χ^2), though other model fits are provided in the PASA Datastore along with other data products. In addition to the model images and residual images, log files from `Halo-FDCA` are also provided so interested users can obtain the model parameters from any of the models.
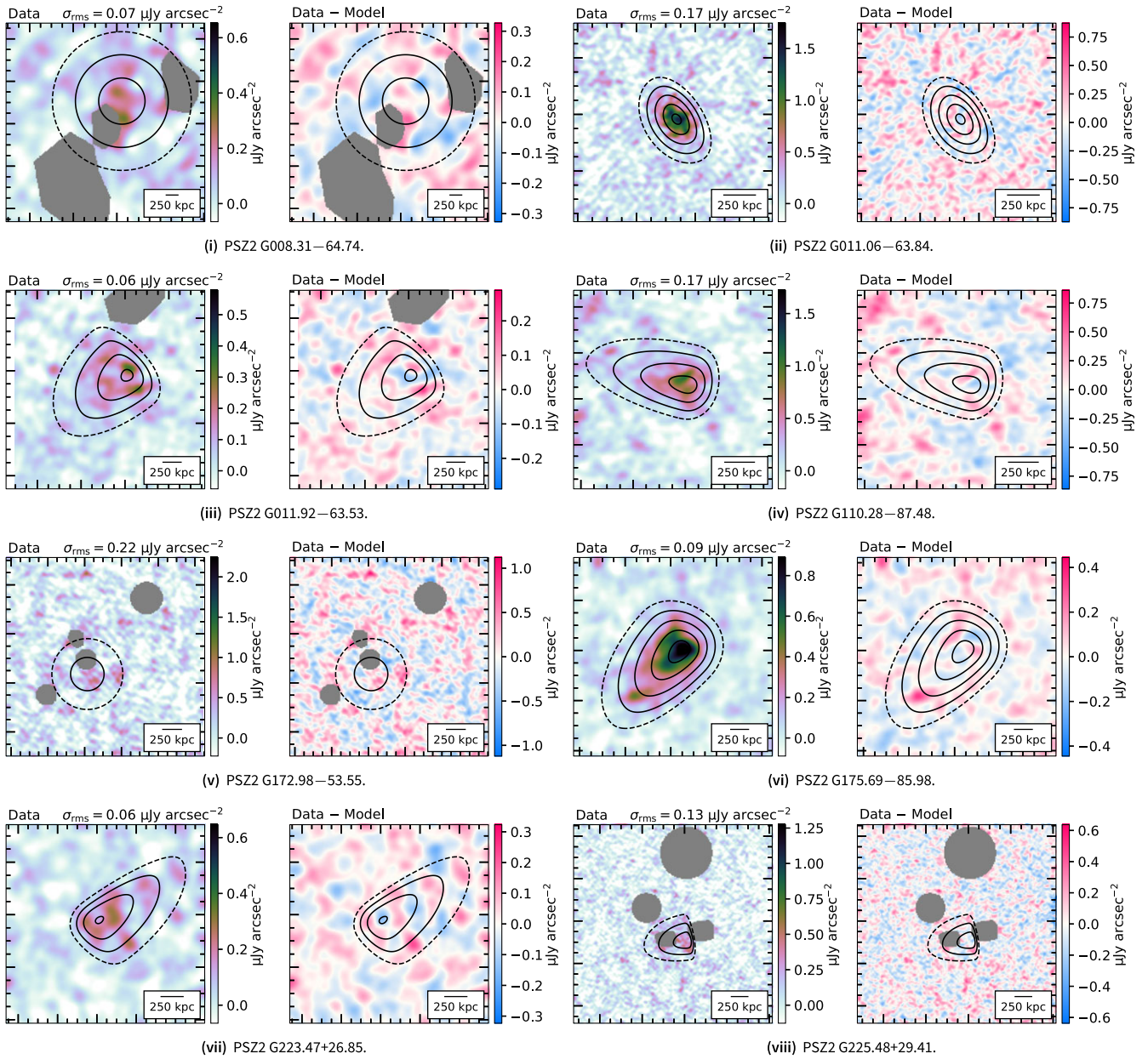
Figure B1. Radio halo models fit using `Halo-FDCA`. *Left.* Compact source-subtracted image used for modelling the halo (and flux density measurements). *Right.* Residual image after subtraction of the model. The model is shown as black contours in both panels (solid: $[1, 2, 4, 8, 16, 32] \times \sigma_{rms}$, dashed: $0.5\sigma_{rms}$). The left panel colourscale is linear between $[-1, 10] \times \sigma_{rms}$ and the right panel colourscale is linear between $[-5, 5] \times \sigma_{rms}$. Grey regions correspond to regions that are masked during fitting. Note the units are in μJy arcsec^{-2} for consistency with the literature.
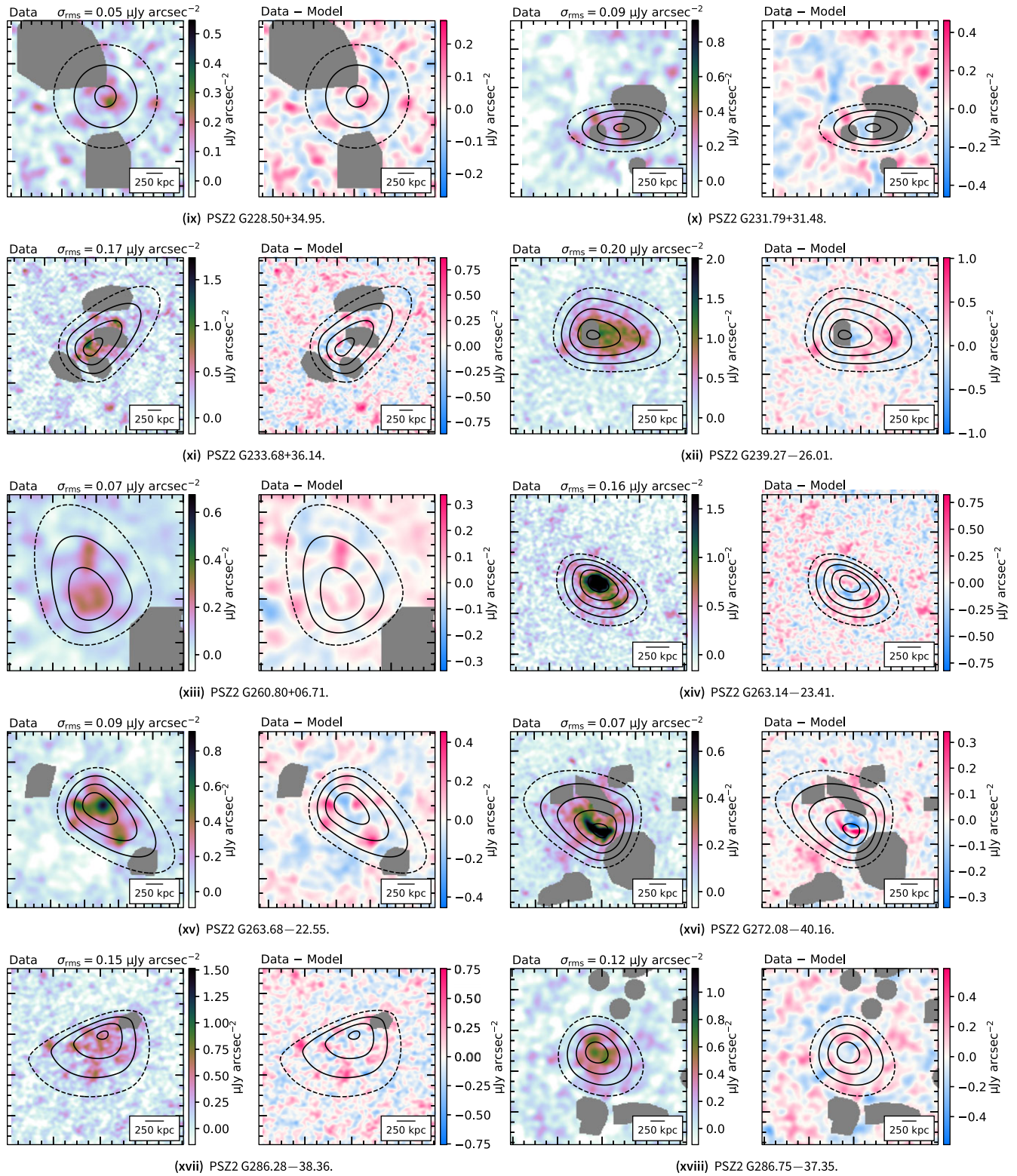
(ix) PSZ2 G228.50+34.95.

(x) PSZ2 G231.79+31.48.

(xi) PSZ2 G233.68+36.14.

(xii) PSZ2 G239.27−26.01.

(xiii) PSZ2 G260.80+06.71.

(xiv) PSZ2 G263.14−23.41.

(xv) PSZ2 G263.68−22.55.

(xvi) PSZ2 G272.08−40.16.

(xvii) PSZ2 G286.28−38.36.

(xviii) PSZ2 G286.75−37.35.

Figure B1. Continued.

(xix) PSZ2 G311.98+30.71.

(xx) PSZ2 G313.33+30.29.

(xxi) PSZ2 G332.23−46.37.

(xxii) PSZ2 G333.89−43.60.

(xxiii) PSZ2 G335.58−46.44.

(xxiv) PSZ2 G342.33−34.93.

(xxv) PSZ2 G346.86−45.38.

(xxvi) PSZ2 G347.58−35.35.

Figure B1. Continued.